Faculteit Wetenschappen

Departement Fysica

Advanced TEM investigation of the elementary plasticity mechanisms in palladium thin films at the nano scale

Gevorderd TEM onderzoek naar de elementaire plasticiteits mechanismen op nanoschaal in palladium dunne films

Proefschrift voorgelegd tot het behalen van de graad van

Doctor in de Wetenschappen

aan de Universiteit Antwerpen, te verdedigen door

Behnam Amin-Ahmadi

Promotoren:

Prof. Dr. D. Schryvers   **Antwerpen**

Dr. H. Idrissi   **2015**

Members of the Jury

Chairman

Prof. Dr. E. Goovaerts, University of Antwerp, Belgium

Promotors

Prof. Dr. D. Schryvers, University of Antwerp, Belgium

Dr. H. Idrissi, University of Antwerp, Belgium

Members

Prof. Dr. C. Kübel, Karlsruhe Institute of Technology, Germany

Prof. Dr. T. Pardoen, Université catholique de Louvain, Belgium

Prof. Dr. B. Partoens, University of Antwerp, Belgium

Contact information

Behnam Amin-Ahmadi

EMAT - Electron Microscopy for Materials Science

University of Antwerp - Department of Physics

Groenenborgerlaan 171, B-2020 Antwerpen

Belgium

behnam.amin-ahmadi@uantwerpen.be

To my family

Preface

Pd has been known for some time to be an enabling material for future hydrogen technologies. For example, thin membranes of Pd can play a role in hydrogen purification and sensing applications. However, the mechanical stability and response to hydrogen pressure of Pd thin films, often having a nanoscale interior structure, is still insufficiently understood. In the present thesis, advanced transmission electron microscopy techniques have been used to unravel the elementary processes activated at the micro- and nanoscale and controlling the nucleation, mobility and interaction of crystal defects and the resulting mechanical properties of as-deposited and hydrided nanocrystalline Pd thin films. Throughout the thesis, the deposition, hydriding cycle and mechanical testing (using on-chip method) of Pd films were performed by IMAP group of the Université catholique de Louvain-la-Neuve. The automated crystal orientation mapping using transmission electron microscopy was performed by 4MAT group of Université Libre de Bruxelles.

Organization of the thesis:

Chapter 1 gives a general introduction to the application and hydriding mechanisms of Pd films used in this thesis. The general description of crystal defects such as dislocations, twin boundary and stacking faults is also presented in this chapter as are the plasticity mechanisms of nanocrystalline face centered cubic metals.

Chapter 2 provides a review on the processing of nanocrystalline metals, the basic TEM techniques used to characterize the materials and the details concerning the preparation of TEM samples using the focused ion beam technique.

Chapter 3 presents micro- and nanostructure characterization of electron beam evaporated Pd thin films including grain size, texture, grain boundary and twin boundary analysis at different deposition rates.

Chapter 4 presents for the first time time-resolved high resolution TEM relaxation experiments of electron-beam evaporated Pd films using an on-chip tensile testing method. Specific attention is paid to the characterization of dislocations and twin boundaries at different time intervals.

Chapter 5 deals with the investigation of the microstructure changes of the $\sum 3\{111\}$ coherent and $\sum 3\{112\}$ incoherent twin boundaries in sputtered Pd films under hydrogen loading using HRTEM. These results are compared to recent experimental and simulation results in the literature.

Chapter 6 first presents the influence of the initial microstructure such as dislocation density, twin boundary density and grain size on the hydriding mechanisms of nanocrystalline Pd films. Then, the effect of hydriding on the microstructure changes of Pd films is documented using advanced transmission electron microscopy techniques. Specific attention is paid on the formation of stacking faults after hydriding/dehydriding of the Pd films.

Table of Contents

Chapter 1

1. Introduction

1.1. Hydrogen as an energy carrier

Since early human history, people have used various sources of energy such as wood and fossil fuels (including coal, oil and natural gas) as a fuel for different applications. However, nowadays with an increasing population, the supply of fossil fuels is getting difficult and has created a serious problem in the world. Moreover, the fossil fuels have serious environmental concerns due to emissions of pollutants, therefore, the use of clean and renewable energy has received more attention recently. One of the best candidates as a clean energy is hydrogen gas. Since hydrogen is the third most abundant element on earth, it is considered as the fuel of the future [1,2]. The Sun 's energy comes from nuclear fusion of hydrogen, but this process is impossible to be controlled on Earth. Therefore, hydrogen is not considered as an energy source. Elemental hydrogen from solar, biological, or electrical sources require more energy to make it, so in these cases hydrogen is considered as an energy carrier.

Hydrogen is more energetic (on a per gram basis) than natural gas, the most energetic fossil fuel. Also, the product of burning of hydrogen is water, therefore, it burns cleanly in air and is non-toxic. It can also be used as possible source for nuclear fusion. Hydrogen has a higher self-ignition temperature ($510°C$) than other fuels such as gasoline ($228 – 501°C$ depending on the grade). Moreover, hydrogen is the lightest element, therefore, it disperses rather rapidly in the atmosphere. These advantages make hydrogen a good candidate to be used in different applications such as the automotive industry. Recently, in these companies, hydrogen-fueled vehicles have been developed.

On the contrary to the mentioned advantages of hydrogen gas, it has some disadvantages such as low mass and high diffusivity which make hydrogen gas difficult to store. It is also highly flammable in concentrations ranging from 4% to 90% by volume [3]. These concerns have led to serious issues in its safety, difficulty in storage and handling of hydrogen gas, which subsequently have prevented complete using of hydrogen gas in different applications. Therefore, it is very important to pay more attention in the investigation and development of the materials used for efficient detection, storage, purification and sensing of hydrogen gas. There is still no standard storage method for hydrogen-powered vehicles and most common designs for hydrogen storage are using high-pressure hydrogen gas in a sturdy stainless steel and composite storage tanks [4].

Various research works have been done on the safe storage of hydrogen in media other than strong tanks such as nanotubes [4-9], complex metal hydrides such as catalyzed alanate

hydrides [10-14], and transition metal hydrides [15-18]. One of the most serious problems of using transition metals and transition-metal alloys for hydrogen storage is the change of the mechanical properties due to hydrogen absorption and desorption. It is indeed reported that these metals become quite brittle due to hydrogen absorption [4]. The embrittlement problem of metals during hydriding was studied in various metal–hydrogen systems. Most of these studies involved the characterization of the mechanical properties of the metal–hydrogen system while the absorbed hydrogen is present in the metal matrix. However, most applications of metal–hydrogen systems involve not only hydrogen absorption but also hydrogen desorption. Therefore, recent studies have focused on systems in which all of the absorbed hydrogen has been removed from the metal matrix prior to characterization [4,19,20]. Palladium (Pd) is a good candidate for these studies since the hydriding behavior of Pd is reversible and desorption of hydrogen gas occurs in ambient conditions. Therefore, many researchers have paid more attention on the effects of hydrogen absorption/desorption cycling on the mechanical and microstructure properties of transition metals and especially on Pd and Pd- based alloys.

1.2. Palladium-Hydrogen

1.2.1. Palladium applications in hydrogen technology

Pd was first discovered in 1803 by Wollaston while working on purification of platinum [1]. It belongs to the group VIII transition elements in the periodic table. The ambient crystalline structure of Pd is face centered cubic (fcc). The primary sources of Pd are copper-nickel sulfide ores and crude platinum. The selectivity of hydrogen by Pd was first discovered in 1866 by Thomas Graham, a British chemist while working with Pd metal. He observed the absorption of large quantities of hydrogen by Pd [1]. He also reported that hydrogen could diffuse very fast through Pd membranes and, hence, can be used to purify the hydrogen [1]. The measured diffusivity of hydrogen in Pd indicates that it is orders of magnitude faster than diffusivities of other gases.

Pd is thus a promising candidate material for hydrogen technology applications. Due to its large hydrogen absorption capacity, Pd proofs to be a good candidate for hydrogen purification and sensing applications, which are essential for hydrogen energy technology. Pd has also high sensitivity and selectivity of hydrogen gas and can release hydrogen at room temperature. Moreover, as mentioned above, hydride formation in Pd is reversible [21].

Hydrogen purification is another process that can be improved via absorption in Pd. Initially the production of hydrogen was done using the electrolysis of water or the gasification of hydrocarbons which causes waste of energy or produces pollutants, respectively. Selective absorption of hydrogen by Pd can lead to a hydrogen purity of 99.99999% without wasting energy and environmental concerns. Pd can also be used as a surface catalyst for absorption of hydrogen. Pd requires a very low activation energy to break apart H_2 molecules into hydrogen single atoms, thus it requires less energy in comparison with other metals to absorb hydrogen [22].

1.2.2. Palladium-Hydrogen system

During hydriding of Pd, hydrogen atoms occupy octahedral interstitial lattice sites of the Pd lattice. Figure 1.1(a) represents a schematic showing the position of Pd atoms (purple circles) and hydrogen atoms (orange circles) in the fcc lattice of Pd. In a fully occupied PdH unit cell, all the octahedral sites are occupied with a total of 4 H atoms in the fcc Pd unit cell. At low hydrogen concentrations, only some of the octahedral sites are occupied which forms the α-phase. At higher concentrations of hydrogen most of the octahedral sites are occupied, giving rise to the β-phase. This β-phase also has an fcc structure and forms due to ordering of hydrogen atoms in the Pd structure. Moreover, it is well known that the interstitial hydrogen atoms induce a volume expansion of the host material [19]. During hydriding of Pd, as long as the H/Pd (atomic ratio) stays below $\alpha_{SSmax} \approx 0.008$ at room temperature, the fcc Pd α-phase will form and cause an expansion of the lattice constant from 3.889 Å to 3.895 Å. When the hydrogen content exceeds this limit, a two-phase region of α- and β-phase Pd appears where the latter structure has a lattice constant close to 4.025 Å. The two phases coexist until H/Pd=0.6 (β_{SSmin}) at which the α-phase disappears entirely. The initial volume of the Pd structure thus expands by about 10% when the H/Pd ratio reaches 0.6 [19-25]. This dilatation can generate extremely large overall compressive stresses if the deformation is impeded by a mechanical constraint imposed to the material such as in the case of a film lying on a thick substrate. Therefore, the β-phase is expected to contain a highly distorted microstructure. Figure 1.1(b) shows that the transition between the two phases as a function of the hydrogen partial pressure and the temperature [25, 26].

The solubility of hydrogen gas in Pd as mentioned in the previous paragraph is established for bulk Pd. However, it is confirmed that this solubility is different for thin films and nanocrystalline (nc) Pd. It has indeed been reported that in thin films and nc Pd, the maximum

hydrogen solubility in the α-phase was increased up to 0.02 (from 0.008) while the minimum hydrogen solubility in the β-phase was decreased down to 0.43 (from 0.6) [26]. These changes lead to a narrowing of the miscibility gap for hydrogen in Pd [27, 28].

At this point it is relevant to mention that throughout this thesis, we define nc metals with an average grain size and range of grain sizes smaller than 100 nm, ultrafine grain (ufg) in the range of 100–1000 nm and microcrystalline (mc) metals containing grains larger than 1 μm. Therefore, nc metals contain a high density of grain boundaries (GBs) due to the small grain size. The change of the solubility of hydrogen gas in nc Pd can be attributed to this high density of GBs which act as hydrogen trapping sites in the Pd microstructure [29]. Hydrogen atoms can also be trapped by lattice defects such as dislocations and vacancies rather than by GBs [22]. Thus, the initial microstructure of Pd affects the hydriding behavior which will be explained in more details in following sections.

Also the thickness of thin films will affect the hydriding behavior of metals [29]. It is reported that with decreasing the film thickness, the maximum solubility of hydrogen in the α-phase (α_{SSmax}) increases and the minimum solubility of hydrogen in β-phase (β_{SSmin}) decreases again resulting in a narrowing of the miscibility gap [30].

Besides, it is confirmed that structural swelling of Pd upon hydrogen loading by interstitial introduction of hydrogen atoms in Pd can result in the closing of nanoscopic gaps followed by a decrease in net resistance of the system which results in an increase of electrical conductivity [31, 32]. In a Pd film without nanoscale gaps, the hydrogen atoms diffuse into the Pd film and occupy the interstitial lattice sites which act as scattering points for electrons leading to an increase in the electrical resistivity of the films. The change in conductivity of the films depends on the amount of absorbed hydrogen or the amount of hydrogen in the ambient. Sensors utilizing this principle can detect the presence of hydrogen ranging from 5% to 100% volume fraction. However, to be able to detect 100% of hydrogen gas by volume, the single phase region in the metal-hydrogen phase diagram needs to be extended by adding alloying elements such as Silver (Ag) and Nickel (Ni) into the Pd [1].

On the other hand, the volume changes of the Pd lattice by hydrogen loading may lead to the generation of dislocations within the Pd matrix and which may affect the mechanical properties of nc Pd. Dislocation generation in nc Pd which is used in sensing application can also have other effect such as shortening of a sensing cell's lifetime, interruption of the electrical circuitry and lowering of the device's sensing sensitivity and proficiency [33]. Therefore, the characterization of nc Pd before and after hydriding is essential to predict the behavior of this metal during any of the above applications.
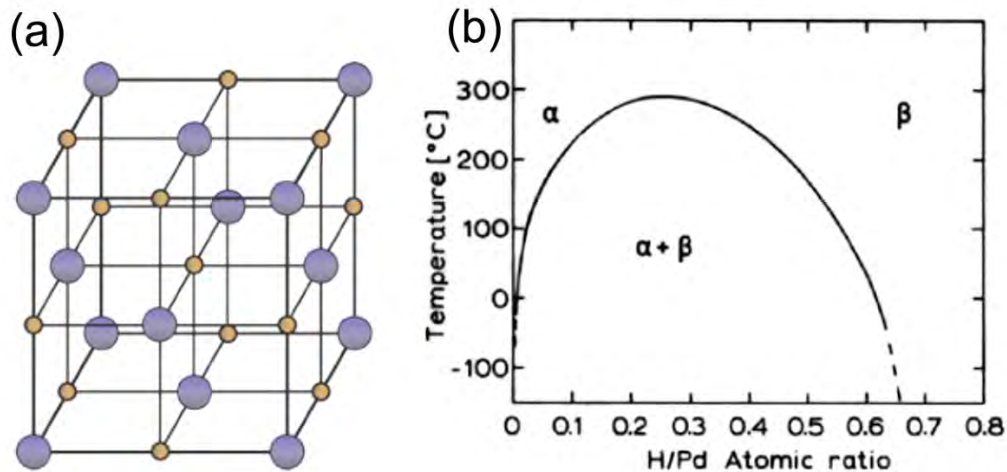
Figure 1.1 (a) Schematic illustration of the Pd fcc lattice (purple atoms) and the octahedral sites containing hydrogen atoms (orange atoms). On the image, each site is occupied and the H:Pd ratio is equal to 1 which has not been reported experimentally [34]. (b) Phase diagram of the Pd-H system [35].

1.2.3. Hydriding kinetics

In order to better understand the microstructural changes after hydriding or the effect of the initial microstructure on the hydriding behavior of Pd, it is best to first look into the hydriding kinetics of metals in general. It is confirmed that the hydriding mechanism of metals involves solid-gas reactions [36] which consist of the interaction of the gaseous hydrogen molecules with the metal surface. Afterwards, hydrogen molecules are adsorbed on the surface of the metal and then dissociated into hydrogen atoms, also referred to as dissociative chemisorption. The adsorbed hydrogen atoms start diffusing into the bulk metal and form the hydride phase. There are different parameters which affect the hydriding mechanism in materials such as the synthesis technique, activation procedure and the earlier treatment of the material. As these parameters change the initial microstructure of the material such as grain size, defect concentration, size and nature of precipitates [36], also the hydriding kinetics will be changed. It can be concluded that the use of nc materials in the form of thin films and powders leads to specific kinetic behaviors during hydriding of metals. The general hydriding mechanism of Pd is schematically illustrated in Fig. 1.2. As indicated in this figure, the hydriding mechanism of Pd can be divided into four steps [30]: (1) hydrogen gas in the form of H_2 molecules is adsorbed onto the Pd surface, (2) the adsorbed hydrogen molecules

dissociate into hydrogen atoms, (3) hydrogen atoms diffuse along a minimum energy path towards available positions in the Pd structure and (4) the hydrogen atoms occupy mainly the octahedral interstitial sites of the fcc Pd lattice and a Pd hydride is finally formed [29]. For further information about hydriding kinetics, please see ref. [29].
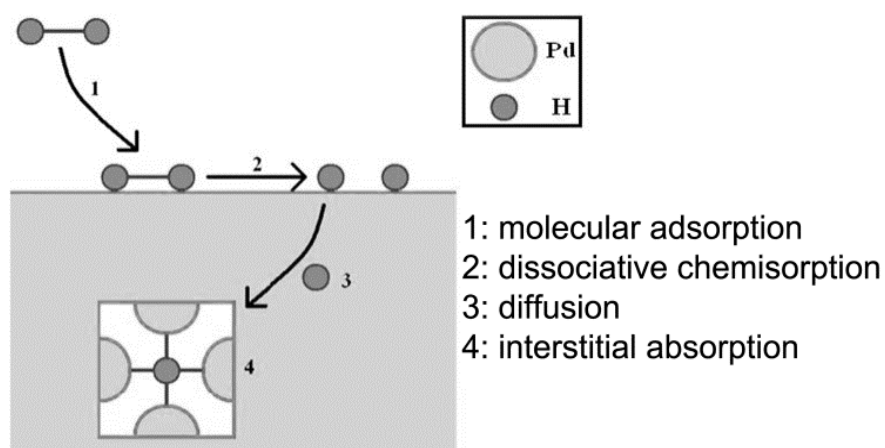
Figure 1.2 Schematic illustration of the kinetic steps during hydriding of Pd.

1.2.4. The effect of microstructure on the hydriding mechanism

As discussed in previous sections, the microstructure plays an important role in the hydriding mechanisms of metals. The microstructure of a metal can offer several types of hydrogen diffusion paths or trapping sites [37] such as GBs, dislocations, twins etc.

Grain boundaries

A GB in a crystalline material is defined as a region separating two crystals (grains) of the same phase but with different orientations. Therefore, a GB represents a transition region, where the atoms are moved from their regular positions in comparison with the grain interior. When the angle between two adjoining grains is low enough, this misorientation can be accommodated by an array of equidistant dislocations referred to as a low angle GB (LAGB). With increasing the misorientation angle, the dislocation model of the GB structure fails because individual dislocations are no more distinguishable and overlap with one another forming high angle GBs (HAGBs). The GB free volume is another parameter which affects

the GB diffusivity, the mobility, and grain growth by vacancy generation. GB free volume is defined as the difference on packing the atoms in the bulk and in the GB. This effect is pronounced in fine grained and nc materials, or in thin films on a substrate. The free volumes provides low energy site for solute atoms in the material. Amount of free volume is increasing with increase of the misorientation angle between two grains except for $\sum$ type boundaries.

With decreasing the grain size, the GB density increases within the metal. As GBs are known as low-energy sites for the absorbed hydrogen atoms, many hydrogen atoms will be trapped at GBs [29]. Mutschele and Kirchheim investigated the hydriding mechanism for nc Pd specimens with a mean grain size of 10 nm [38]. They observed the narrowing of the miscibility gap which is consistent with the hydriding behavior of other thin film specimens. The narrowing of the miscibility gap was explained based on the high density of GBs. During hydriding the nc Pd, at low hydrogen concentrations, the low energy sites existing at GBs are filled with hydrogen which increases the maximum solubility of the α-phase (increase of lower limit of miscibility gap). But at higher hydrogen concentrations, only the grain interiors can be occupied by additional hydrogen atoms. Thus, this lowers the minimum solubility of the β-phase [25].

Dislocations

A dislocation is defined as a one-dimensional crystallographic defect or irregularity, within a crystal structure. Dislocations can be viewed as a group of atoms in an irregular position arranged along a line and running throughout an entire crystal or a grain. The presence of dislocations in a crystal structure affects different properties of the materials such as mechanical and electrical properties. There are two primary types of dislocations called edge and screw dislocations, which can be distinguished based on the concept of the Burgers vector and Burgers circuit. A Burgers circuit is drawn in a crystal around a dislocation using an atom-to-atom path which forms a closed loop. If the same circuit (in terms of number of atom-to-atom steps in each direction) is drawn in a perfect crystal without the dislocation, the loop does not close. The Burgers vector is the vector that is needed to close the gap. An edge dislocation has a Burgers vector perpendicular to the dislocation line. Alternatively, a screw dislocation is formed when the Burgers vector is parallel to the line of the dislocation. Figure 1.3 shows a schematic illustration of Burgers circuits and vectors for examples of edge and screw dislocations [39].
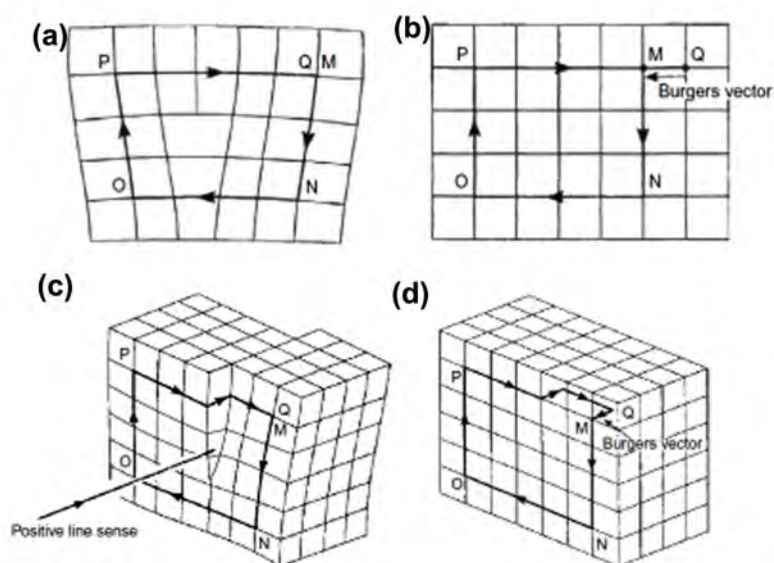
Figure 1.3 (a) Burgers circuit around an edge dislocation, (b) the same circuit in a perfect crystal. The closing vector (QM) is the Burgers vector. (c) Burgers circuit around a screw dislocation, and (d) the same circuit is drawn around a perfect crystal which shows the closing vector of QM as Burgers vector [39].

The shortest lattice vectors (Burgers vectors) for dislocations in the fcc structure are of the type 1/2<110> and <001>. Since the energy of a dislocation is proportional to the square of the magnitude of its Burgers vector (b^2), 1/2<110> dislocations have half the energy of <001> dislocations. Thus, <001> dislocations are much less favored energetically and rarely seen in fcc materials. The 1/2<110> dislocations are called lattice dislocations since the 1/2<110> vector is a translation vector of the fcc lattice and the glide of this dislocation leaves behind the perfect crystal. Moreover, lattice dislocations can split into so-called partial dislocations with the Burgers vectors shorter than 1/2<110> but which are not lattice vectors, therefore, the movement the partial dislocations in the initial {111} glide plane leaves behind an imperfect crystal containing a stacking fault (SF). In the fcc structure, partial dislocation can be of the type of Shockley Partial Dislocations (SPD) or Frank dislocations (FD). The SPD is associated with slip and has a Burgers vector of 1/6<112>. However, the Frank partials have a Burgers vector perpendicular to {111} planes (1/3<111>). Since the Burgers vector of a Frank

partial is not contained in one of the {111} planes, it cannot glide under applied stress. Therefore, they are called sessile dislocations, unlike the glissile SPDs [39].

Dislocations can be formed by plastic deformation of metals. However, dislocations in thin films are also generated during the deposition process due to the formation of internal stress within the film. They can also be created by hydriding or dehydriding of Pd films, where the dislocations accommodate the lattice mismatch present when the hydride phase nucleates and grows in the Pd matrix [29].

It is reported that hydrogen atoms can interact strongly with dislocation cores. This is due to a strong interaction between the tensile strain field of an edge dislocation and the hydrostatic stress component of the hydrogen atoms. Therefore, edge dislocations act as traps for hydrogen in Pd. Chemical potential-concentration isotherms measured on thin Pd films with different dislocation densities revealed a strongly enhanced hydrogen solubility in the low hydrogen concentration range [39,40]. However, screw dislocations interact weakly with the hydrogen atoms [29] due to weak interaction of the shear stress components generated by the screw dislocations with the hydrostatic stress component of the interstitial hydrogen atoms. Moreover, it is also well-known that dislocations act as preferential pathways for hydrogen transport [41], which affects the hydriding kinetics of Pd films, as well.

Twins

Twins are a type of planar defects which can be formed in a crystal either during deposition of a thin film or by deformation. The effect of twins on the hydriding mechanism of metals remains unclear. Several studies report that twins can act as hydrogen traps [42], but other studies do not confirm these observations such as the research done on steels. Some studies on Magnesium (Mg) indicate that twins do not have any effect on the hydriding thermodynamics [43], although Danaie et al. [43] did observe the improvement in the hydriding kinetics of their Mg powders. Therefore, twins can possibly be considered as preferential pathways for hydriding behavior. Besides, twins have other important effects on mechanical properties of different metals. Due to the importance of twins in hydriding and also in mechanical properties of metals, these defects are explained in more detail in the next section.

1.3. Introduction to Twin boundary

The most common twin boundary (TB) in an fcc crystal is defined as a {111} type plane at which the normal ABCABC stacking sequence in fcc structures reverses in the mirror relation. This mirror relation of atomic structure across the TB can be visualized along the [011] zone axis which is presented schematically in Fig. 1.4. In this case, the coherent TB (CTB) plane is the $(1\bar{1}1)$ close-packed plane. The angle of the TB plane with the other close packed planes in the [011] direction (i.e. $(11\bar{1})$) is 70.53˚. Here it should be mentioned that each lattice point in this two-dimensional illustration (Fig. 1.4) represents an atomic column containing an array of atoms along the viewing direction.
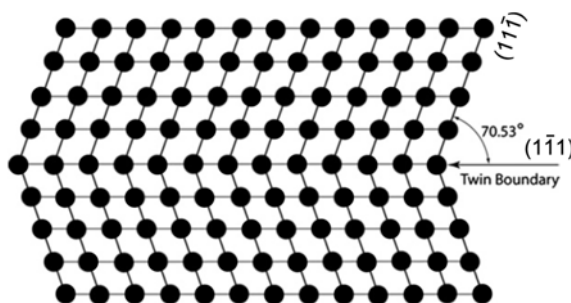
Figure 1.4 Schematic illustration of a TB in fcc crystals viewed along the [011] direction showing the mirror symmetry of the atomic structure.

TBs can be formed via different processes such as deformation, annealing and thin films or layers deposition processes. In order to better understand the formation of these planar defects and the effect of the stacking fault energy (SFE) on the twinning behavior of metals, in the following section the SF and SFE are described.

1.3.1. Stacking fault energy

The SF in a close packed system refers to a disruption in the long range stacking sequence of the lattice. This kind of disruption can induce two common types of crystal defects: a SF and a twin region [44, 45].

A SF can be either intrinsic or extrinsic. In the intrinsic case (ISF) a close packed plane is removed from the lattice yielding an ABC**AC**ABC stacking, i.e. with a missing B plane. In the extrinsic case (ESF) an extra plane is inserted in the lattice yielding an ABCA**C**BCABC stacking, i.e. with an extra C plane. In the former the disruption happens through one atomic layer in the crystal structure, in the latter the defect appears over two atomic layers (Fig. 1.5). Moreover, the systematic introduction of SFs over many atomic layers produces a twin region.

As explained in section 1.2.4, a lattice dislocation (1/2<110>) can dissociate in two SPDs (1/6<112>) bounding a SF since it is energetically favored. This configuration is called an extended dislocation. During applying a stress, first a leading partial glides and leaves behind the SF ribbon and the trailing partial removes the SF. Therefore, the total slip vector will be equal to 1/2<110>. The existence of a SF ribbon with a certain width is due to the balance between different forces on the SF such as the repulsive force between the leading and trailing partial dislocations and the attractive force due to the surface tension of the SF. As a result, these SFs carry an amount of energy (SFE) defined as the energy per unit area of the SF. It can be concluded that the SF width is reversely proportional to the SFE. The SFE is a materials property which also affects the twinning behavior of materials and plasticity mechanisms during deformation [46]. It is well known that with decreasing SFE, the formation of SFs and deformation twinning in coarse-grained fcc metals increases. The same behavior has also been observed in nc fcc metals.
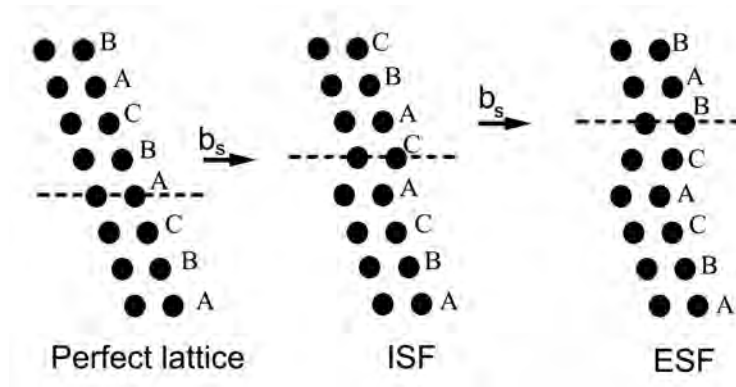

Figure 1.5 Schematic illustration of the formation of intrinsic and extrinsic SFs via glide of SPD (b_s=a/6<112>).

However, it is recently reported using experimental and simulation results that the SFE is not a sufficient parameter to describe and study the twinning behavior in different materials. It is reported that the so-called generalized planar fault energies (GPFEs) have significant implications on plastic deformation of nc materials [46,47]. A GPFE (Fig. 1.6) consists of three important energies: intrinsic SFE (γ_{isf}), unstable SFE (γ_{usf}), and unstable twin fault energy (γ_{utf}). The unstable SFE is defined as the energy barrier for homogenous nucleation of a SF within a perfect lattice by movement of a leading partial dislocation.. The energy barrier for formation of the trailing partial to form a dissociated dislocation with a SF in between is proportional to the ratio of $\gamma_{usf}/\gamma_{isf}$, essentially defining the intrinsic SFE. The unstable twin fault energy is defined as the energy barrier for the formation of a twin nucleus by nucleation of leading partials at successive {111} planes in the fcc crystal (see Chapter 6 for more detail on these different terms) [44]. The GPFE curves can be extracted for fcc metals, using *ab-initio* calculation when sliding two semi-infinite crystals on a {111} plane along a [112] direction.

Figure 1.6 shows the schematic illustration of GPFE curves for Ni. As shown in Fig. 1.6, Ni has a very high SFE (≈110 mJ.m^{-2}), therefore as discussed above, it is difficult to form SFs by slip of partial dislocations due to deformation. However, experimental studies revealed both the formation of SFs and deformation twins in nc Ni. Moreover, molecular dynamics (MD) simulations confirmed the formation of SFs in Ni [45].

The formation of SFs in Ni can be explained using the GPFE curve [46]. During deformation of Ni, if the amount of resolved shear stress is large enough to overcome the Peierls-Nabarro stress (the force needed to overcome the lattice resistance for moving a dislocation) a SF generates by formation of a leading partial dislocation. However, the barrier for nucleation and movement of the trailing partial dislocation is a function of γ_{usf}–γ_{isf}. If the γ_{usf}–γ_{isf} value increases, the formation of the trailing dislocation will become more difficult. It has been reported that this barrier (γ_{usf}–γ_{isf}) is large for Ni and Copper (Cu) in comparison with Aluminum (Al). Therefore, during deformation of Ni, leading partial dislocations nucleate and slip without formation of the trailing dislocation leaving a SF behind. Besides, since the value of the unstable twin fault energy is very close to the unstable SFE, twins can be easily formed once a leading partial is nucleated and slipped. Therefore, deformation twinning can be activated in Ni despite its high SFE.
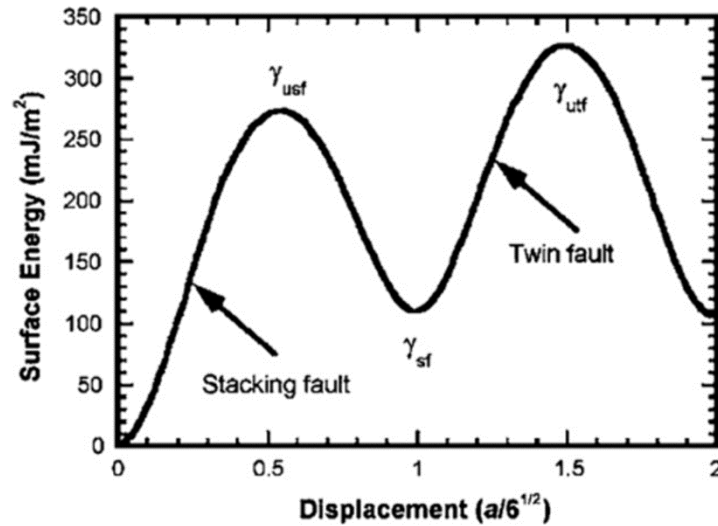
Figure 1.6 Schematic illustration of the GPFE curves for Ni [45]. γ_{sf} is the stable SFE; γ_{usf} is the unstable SFE; γ_{utf} is the unstable twin fault energy; and "a" is the lattice constant.

In a summary, it can be concluded that during deformation of materials, first a SF forms and then a deformation twin nucleates. The nucleation and slip of the leading partial dislocation leads to the formation of the SF after which the formation of twinning partials on the successive planes where the leading partial slips converts the SF to a twin nucleus. However, the grain size may also affect the formation of SFs and twins during deformation. Since a higher stress is required to emit a partial dislocation in smaller grains, in a material with higher unstable twin fault energy than the unstable SFE, below a certain grain size, the required stress for nucleation and movement of the twinning partial dislocation will be higher and no twinning occurs in such small grains. However, the extended SFs will be formed because the applied stress is still high enough to emit the leading partial dislocations.

In the following section three different twins including deformation, annealing and growth twins will be described in more detail.

1.3.2. Deformation twinning

As explained in the previous section, deformation twins in fcc metals are formed by the nucleation and glide of partial dislocations on successive planes. All these partial dislocations have the same Burgers vector which induces a macroscopic strain in the crystal to accommodate the imposed strain. Figure 1.7 shows schematically the formation of a

deformation twin in the upper part of a sphere-shaped grain via glide of the partials with a Burgers vector $\mathbf{b_1}$. As shown, the upper part of the grain is sheared into a new shape due to the glide of the partial dislocations with the same Burgers vector on successive atomic planes. Therefore, a GB kink will be produced at the TB with an angle of 141˚, which is twice the angle between two close-packed {111} planes as indicated in Fig. 1.4.
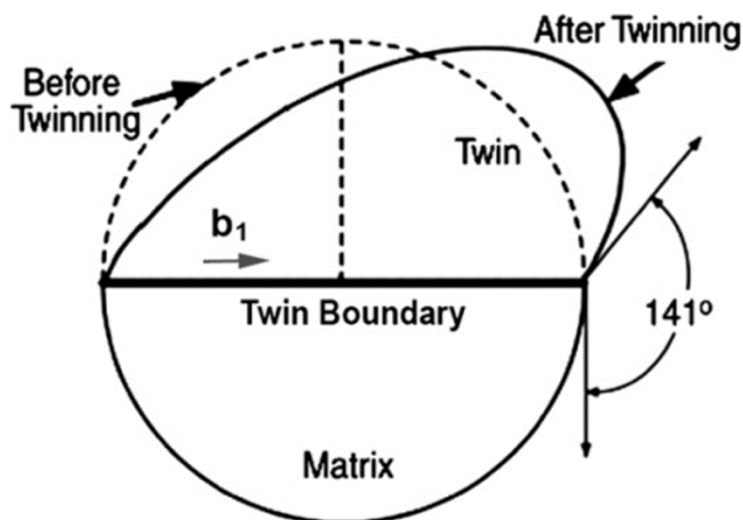
Figure 1.7 Conventional deformation twinning by the gliding of one type of partials on successive slip planes above the twin boundary [46].

In fcc crystals, the twinning partial dislocations have a Burgers vector of a/6<112> which can glide on the respective <111> slip plane (Shockley partials). Therefore, in an fcc cubic structure, on every slip plane there are three equivalent SPDs. For example, if you consider the (111) plane as slip plane, the three SPDs are $\mathbf{b_1}$ = Bδ = $\frac{a}{6}$[2$\bar{1}\bar{1}$], $\mathbf{b_2}$ = Aδ = $\frac{a}{6}$[$\bar{1}$2$\bar{1}$], and $\mathbf{b_3}$ = Cδ = $\frac{a}{6}$[$\bar{1}\bar{1}$2] which are schematically presented in Fig. 1.8(a). The used lettering refers to the ABC stacking sequence of close packed planes in fcc crystals. One should notice that there are also three partials with opposite Burgers vectors, -$\mathbf{b_1}$, -$\mathbf{b_2}$, and -$\mathbf{b_3}$. The magnitude and direction of these Burgers vectors are indicated by red arrows in Fig. 1.8(b) on the (111) slip plane. The disruption within the stacking sequence can occur by gliding a partial dislocation across the slip plane which leads to the formation of a SF. Based on this explanation, the position of atoms will change due to the formation of the SF. The shift in the

position of the atoms occurs based on the magnitude and orientation of the Burgers vectors shown in Fig. 1.8(b), therefore, the shift can be described as A→B B→C C→A [45].

As explained in section 1.3.1, the deformation twinning forms by nucleation and slip of partial dislocations with the same Burgers vectors on successive slip planes. Figure 1.8(c) shows the change in stacking sequence by formation of a four-layer deformation twin. Column 1 shows the normal stacking sequence of an fcc crystal while the following columns represent the change in stacking sequence due to the glide of a partial dislocation with b_1 Burgers vector. The slip of a partial dislocation with Burgers vector b_1 leads to the formation of an intrinsic SF by shifting of atoms from B to C positions and thus yielding a missing layer of atoms in B positions (column 2). The nucleation and slip of the partial dislocation on the successive slip plane with the same Burgers vector causes the formation of two layered extrinsic SFs (CB in column 3) which can also be considered as a nanotwin. The twin region is enlarged by further slip of the same partials on the successive slip planes. Column 5 in Fig. 1.8(c) shows the formation of a four-layer twin CBAC due to the slip of partial dislocations with the same Burgers vector on successive planes. However, there are other mechanisms which include the movement of a mixture of partial dislocations. The latter mechanisms induce smaller macroscopic strain since partials with different Burgers vectors shear the lattice in different directions [45,48].
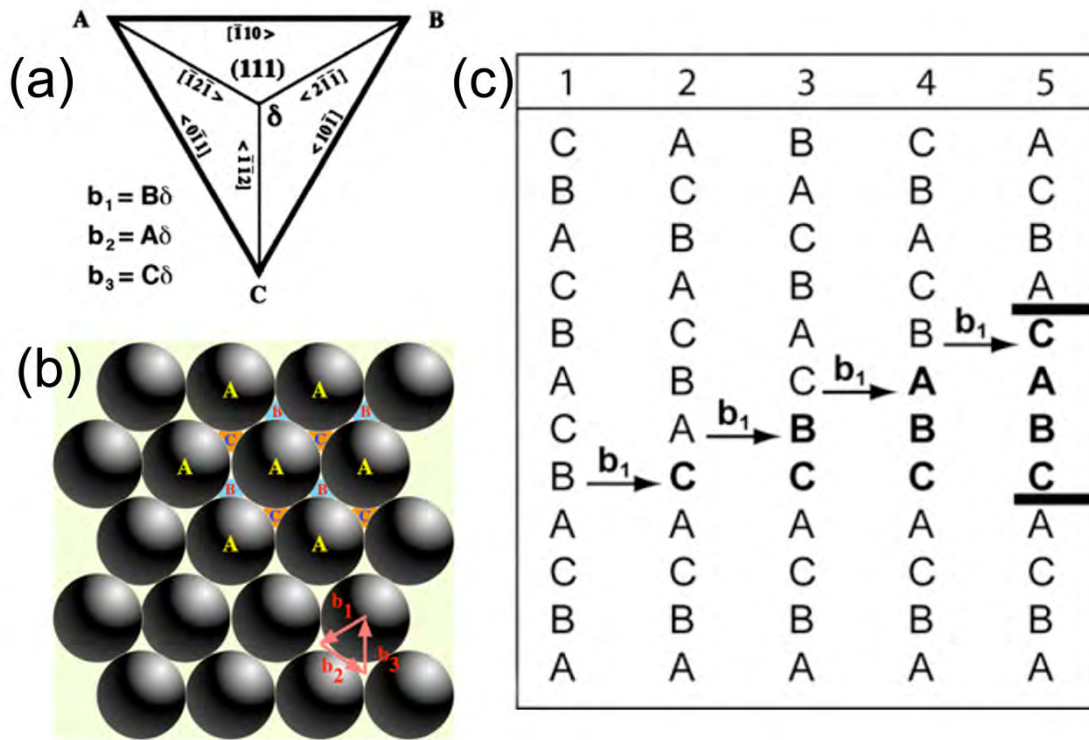
Figure 1.8 (a) Three equivalent Burgers vectors b_1, b_2, and b_3 of SPDs on the (111) slip plane. (b) The magnitude and direction of the three partial Burgers vectors, b_1, b_2, and b_3, on the (111) plane, and the positions of atomic stacking A, B, C. (c) The formation of a four-layer CBAC deformation twin by the slip of four partial dislocations with the same Burgers vector b_1 [45].

1.3.3. Annealing twinning

Annealing twins are another type of twins in metals which has been observed in a variety of deformed and subsequently annealed fcc metals and alloys as early as 1897 [49]. The formation of annealing twins is usually attributed to a grain growth process which occurs during annealing at relatively high temperatures [49].

Annealing and deformation twins consist of SFs which have been formed by slipping partial dislocations on successive slip planes. As discussed in section 1.3.2, a mechanical force is needed for the nucleation and slip of partials to form the deformation twins. Thus, in the absence of an applied stress, the formation and growth of annealing twins is difficult to understand.

In the literature, there are different studies which explain several models for the formation and growth of annealing twins. These models are based on growth accidents and/or nucleation of

twins by SFs or fault packets [48,49]. The growth accident model assumes that during grain growth, atoms move from the shrinking grains to the growing ones. The annealing twins form due to the introduction of {111} steps in the GB during grain growth. Another model attributes the formation of annealing twins to the existence of SF packets in the structure. The formation of SF packets is attributed to the fault formation (pop out) from ledges present on GBs. Further studies on the formation of annealing twins in Ni showed that the formation of twins is caused by GB migration and their density depends on the driving force for migration of GBs. This driving force is associated with the curvature of the GB, the smaller the radius of this curvature, the higher the driving force for formation of annealing twins. The net curvature of a boundary can be described by {111} steps (also referred to as ledges and facets) present in the boundary (see Fig. 1.9) [49]. With decreasing the radius of curvature, the area containing these steps increases. The formation of annealing twins can be explained by the movement of the step schematically illustrated by MNRQ in Fig. 1.9. Due to the growth of grain I, the step moves upwards and the upper portion PQRS of the boundary moves towards the right and lines up with the lower boundary segment LMNO. The stacking sequence of {111} planes in both grains is ABCABCA assuming that atoms in the MNRQ step are in C position. During growth of grain I, the upper segment of the GB moves to the right and steps move upward forming an unfaulted region within the volume swept by the migrating step. However, it is possible that due to growth accidents atoms above the newly formed step plane may find themselves in the B position instead of the A position. Therefore, an intrinsic SF or one-layer thick annealing twin forms. The higher the velocity of the boundary, the higher the probability of growth accidents. Such a faulted region consists of one SPD loop. If faulting occurs on consecutive {111} step planes, thicker annealing twins can form [49].
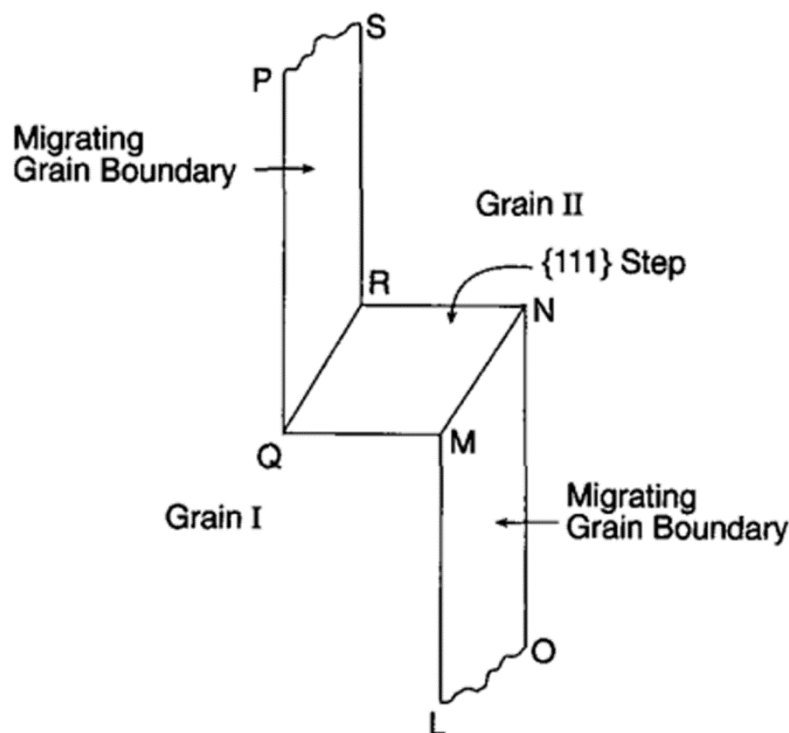
Figure 1.9 Schematic illustration of a {111} step (MNRQ) along a GB. Grain I grows at the expense of grain II due to GB migration [49].

1.3.4. Growth twins

Twin structures may also form during crystal nucleation and growth from vapour and liquid phases. In this case, quite large and nearly perfect twins are produced often transecting entire grains.

Recently, nc metallic bulk samples and layers of Cu, stainless steels, Ag, Ni and Pd containing growth twins have been successfully produced using pulsed electrodeposition [50-52] and sputter deposition [53–57]. All these studies show that the existence of growth twins in nc materials leads to the resistance of material to plastic localization or improvement of the strength/ductility balance. In order to facilitate the formation of growth twins, the efforts were intentionally focused on metals with low and moderate SFE, such as Cu [50–53] and stainless steels [54–57]. However, there are very few research works which have focused on the formation of growth twins in high SFE nc materials such as Pd thin films despite the technological needs for such a twinned metallic films in hydrogen technology applications. Very recently, Pd films with ≈30 nm grain size, deposited using electron-beam (e-beam) evaporation, have been characterized in detail by transmission electron microscopy (TEM)

[58]. These studies confirmed that more than 20% of the grains contain growth twins. The formation mechanism of growth twins in Pd films was also investigated. Nc Pd films which were deposited using two methods based on physical vapour deposition (PVD): e-beam evaporation and sputter deposition [59] were used. Technical details about the deposition of Pd films can be found in [59]. Typical bright field (BF) micrographs of these Pd films are shown in Fig. 1.10. TEM analysis showed that sputter-deposited films have very few growth twins, while a significant number of nanograins containing growth twins were observed in the films deposited by e-beam evaporation. The orientation of these films was also investigated using selected-area electron diffraction (SAED) on different regions throughout the sample. The results showed that the sputtered Pd film exhibits strong <111> fcc crystallographic texture (inset of Fig. 1.10(a)) similar to the microstructure of sputter deposited, textured and highly twinned Cu and stainless steel layers [57-64]. However, no twins were observed within the grains of Fig. 1.10(a). This lack of twins was first attributed to the high SFE of Pd (130–180 mJ.m^{-2}), hence to the too small driving force for the formation of twins. In the literature, the observation of nanoscale growth twins in sputter deposited Cu and stainless steel films is related to the low SFE of these metals. Therefore, with decreasing SFE, the probability of twin nucleation increases [61]. Thus, high SFE metals such as Al (160–200 mJ.m^{-2}) or Pd, are unlikely to show any SFs or twins. However, the growth twins were observed in non-textured Pd film (Fig. 1.10(b)), so it was concluded that the mechanism responsible for the formation of growth twins in sputter deposited Cu and stainless steel films containing strong <111> texture is unlikely to be responsible for the observed twins in the Pd films. By comparing the images in Fig. 1.10, it could be anticipated that there is a relationship between the absence of the crystallographic texture in the e-beam-evaporated films and the formation of the growth twins. Such feature points towards a role of GBs in the formation of twins.
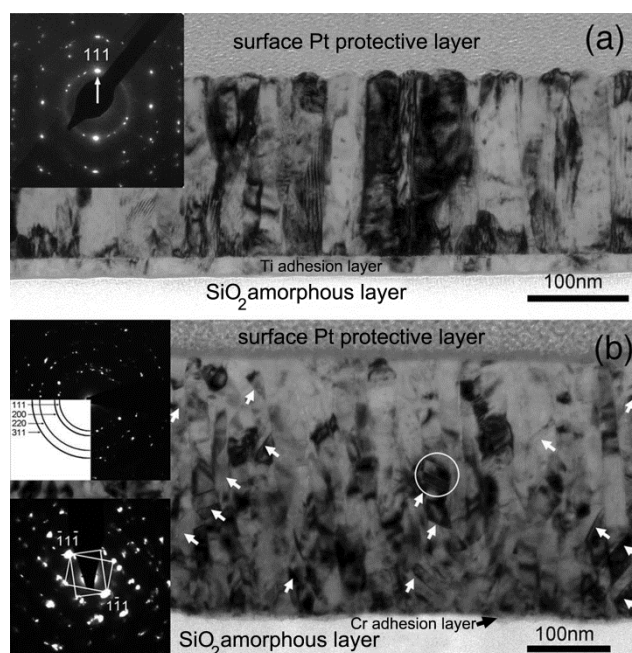
Figure 1.10 (a) BF micrograph of cross-sectional focused ion beam (FIB) specimen prepared from a sputter deposition Pd film. Inset shows the <111> texture parallel to the normal of the film. (b) BF micrograph of cross-sectional FIB specimen prepared from Pd film deposited by e-beam evaporation. Growth twins are shown by white arrows. Left insets show no texture (top) for the entire film and a {111} nanotwin pattern in the grain indicated by a white circle (bottom) [59].

The mechanism based on GB migration was initially proposed by Ashby and Harper [60] and also described by Gleiter [61]. This model involves the splitting and the subsequent migration of a GB segment, leaving behind two CTBs. Fullman and Fisher [62] proposed that twins form by GB migration during grain growth as a result of a decrease in the interfacial free energy of the GBs that would not be achieved in the absence of twinning. In other words, twins prefer to nucleate at GBs or triple junctions to reduce GB energies through orientation changes and a high twin density leads to a lower average GB excess energy for a similar grain size including twins. Therefore, the formation of growth twins in Pd films can be based on the formation and glide of twinning dislocations from high energy GBs [63-68] in the non-textured films.

1.3.5. Effect of growth twins on mechanical properties of nc Pd films

As for nanostructured bulk metallic materials, the strain hardening capacity (the capacity of the metals to harden with plastic deformation) of thin metallic films is often very low which

21

can be the reason of weak ductility in these materials. Ductility is defined as the ability of a material to deform plastically without plastic localization or without damage. Low ductility in the nc thin metallic films is due to the lack of forest hardening in nanosized grains. However, the presence of imperfections such as TBs inside these small grains acts as barrier against movements of lattice dislocations that eventually increase the strength and ductility of the nc films.

The mechanical properties of the nc Pd films were measured [58,69] using a novel concept of on-chip nanomechanical tensile testing, devoted to the characterization of the mechanical behavior of freestanding thin films or wires [70-72]. This on-chip nanomechanical tensile testing will be explained in details in section 4.2.1. The stress-strain curve of a Pd film with the thickness of 160 nm showed fracture strain of 6%, more than 1 GPa strength and an unexpectedly large strain hardening capacity compared to what is currently reported for nc materials without growth nanotwins (fracture strains of $\approx$ 1%) [58].

This large strength/ductility balance was attributed to the presence of the nanotwins. These nanotwins act as barriers to dislocation motion as well as sources for dislocation storage and multiplication via specific TB/dislocation reactions (see Ref. [58] for more details), providing an isotropic hardening contribution to the strain-hardening capacity. In addition, the presence of the nanotwins leads to significant back-stresses at the levels of the grain interior as well as heterogeneities at the level of the grains (grains with no twins being softer than grains with twins), both effects contributing to a significant kinematic hardening [69]. A semi-analytical grain aggregate model has been developed [69] in order to investigate the impact of these different contributions on the flow behavior of the Pd films, involving the effect of the twins, of the grain size and of the presence of a thin surface layer. This model provides guidelines for optimizing the strength/ductility ratio of the films, showing potential for significant improvement by working on the nanotwin configuration. It is indeed important to note that the experimentally observed high strain hardening capacity is obtained with only one-fifth of the grains containing nanotwins, revealing a huge potential to improve the strength/ductility balance even further.

Despite the TB effect on the plasticity mechanism of nc materials, there are other parameters which can control the plasticity mechanisms in these materials. In the following section, the possible plasticity mechanisms which can be activated with decreasing the grain size will be explained.

1.4. Plasticity mechanisms in nc metals

Nc materials are commonly defined as systems with grain size less than 100 nm. The decrease of grain size in materials has received much attention in recent years due to its enhancement of strength. Moreover, the tendency to miniaturization of various systems and devices of electromechanics, robotics, electronics, medicine, and so on requests systems with smaller dimensions [73].

The origins of grain-size strengthening can be explained by the Hall-Petch (H-P) equation which is suggested for polycrystalline materials:

$$\sigma_Y = \sigma_o + kd^{-1/2}, \tag{1.1}$$

where σ_Y is the yield strength, σ_o is the friction or internal stress opposing dislocation motion, k is the so-called "locking-parameter", and d is the mean grain size. σ_o and k are material-dependent constants that can be determined experimentally. It is reported that coarse-grained materials perfectly follow the H-P relation. Cottrell made a first attempt for a physical explanation on the grain-size strengthening [74]. He proposed a mechanism for grain size strengthening which includes the piling up of dislocations at GBs. However, in polycrystalline materials containing smaller grains, the dislocation motion is highly limited due to the presence of a high density of GBs. Dislocations which are generated in the interior of the grains will be blocked at GBs since the slip planes will be discontinuous due to the different orientation between the two grains. Applying more stress leads to the propagation of more dislocations on the same slip plane until they are repelled by the existing dislocations near the GB. This process continues until the amount of applied stress is high enough that the leading dislocation close to the GB transmits through the GB or another source is activated in an adjacent grain. These events lead to the macroscopic yielding of the material with the yield stress being defined as the stress which is required to initiate the plastic deformation when the material is pulled in tension.

Figure 1.11 shows the variation of yield stress as a function of grain size in mc, ufg and nc metals. It is seen that for ufg and mc, the yield stress increases with decreasing grain size which can be described by the H-P relation. In this regime, as explained above, the dominant plasticity mechanism is the pile-up of dislocations at GBs. With further decrease of the grain

size into the nanosized region, the trend of increasing the yield stress changes which is attributed to the change of deformation mechanisms. .

It has already been confirmed that the mechanism of dislocation nucleation in nc materials differs from that in mc and ufg materials. This is due to the lack of Frank-Read sources inside the small grains of nc materials, so the source of dislocation nucleation is just limited by GBs which will assist the nucleation and accommodation of dislocations [75]. GBs in nc materials are mostly high energy non-equilibrium boundaries which contain a much higher density of dislocations compared to GBs in mc materials. Therefore, they can act as source for the emission of dislocations inside the nanograins [75].

Recently, it has been noted that perfect dislocations are highly active in nc materials in contradiction to earlier reports in which only partial dislocations were observed in nc materials [76, 77]. However, the presence of partial dislocation activity was also confirmed by Liao et al. for nc Al containing wide SFs bounded by partial dislocations [78]. Furthermore, they also predicted the formation of wide SFs for other fcc materials with high SFE such as Ni. Moreover, Yamakov et al. have predicted by MD that in columnar nc Al, the plasticity is fully determined by dislocation activity [79].
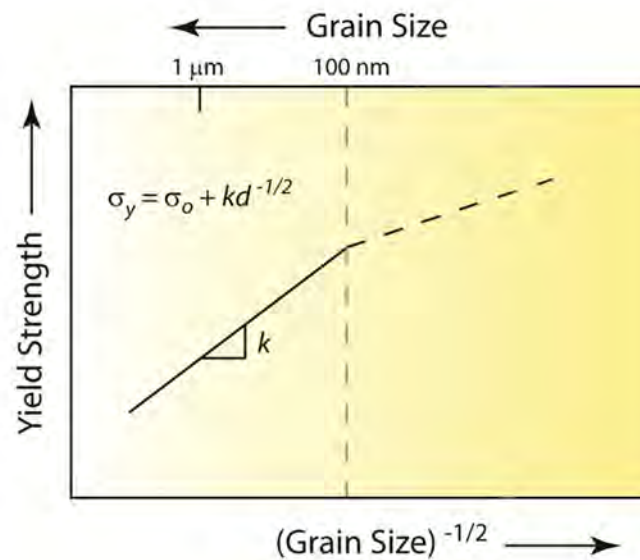

Figure 1.11 Schematic illustration of Hall-Petch plot showing the yield strength versus the grain size and the breakdown below 10 nm [73].

The results of MD simulations on nc materials show that the deformation mechanism is based on the nucleation of partial dislocations at GBs. For metals with low SFE such as Cu, only one partial is emitted from the GB, which leads to the formation of a SF. On the other hand, for metals with high SFE such as Al a trailing partial follows, leading to the formation of a full dislocation [75-86]. The transition in deformation mode is associated with the competition between the grain size and the separation distance between those partial dislocations.

The presence of TBs also affects the mechanical properties and deformation mechanisms in nc materials by changing the dislocation storage capacity of nc materials [87]. This behavior is mainly attributed to the TB-dislocations interactions as deformation mechanisms in nanotwinned materials. Recently, Idrissi et al. has reported that the strength/ductility balance of Pd thin films with an average grain size of 30 nm can be significantly improved due to the presence of coherent growth nanotwins [58]. TEM analyses have also shown that the dislocation pile-up against TBs is the principal mechanism of plastic deformation. Therefore, TBs are able to sustain much more shear strain than the grain interior. It is also observed both experimentally [88] and numerically [89,90], that dislocations can propagate across the TB by applying high stress, leaving defects on the TBs.

The twins are often initially coherent. Recently, Wang et al. have demonstrated the inherently defective state of coherent TBs in nanotwinned Cu [91]. Zhu et al. have observed that the initially coherent TBs lose their coherency during deformation [92]. The same authors have studied by atomistic simulation the reaction between dislocations and TBs. They attributed the high ductility of nanotwinned Cu to the hardening produced by the progressive loss of coherency of the TBs. They found that TBs act as sources and sinks for dislocations but can also play the role of strong obstacles against dislocation transmission across TBs.

Kobler et al. [93] investigated the microstructure and mechanical properties of nc Pd films. They reported that depending on the initial twin density, the samples behaved differently. For low initial twin densities, an increasing twin density was found during straining. On the other hand, starting from a higher twin density, the twins were depleted with increasing strain. Therefore, the initial twin density affects the plasticity mechanism in Pd films.

As already mentioned, with further decrease in grain size, non-dislocation mechanisms such as GB sliding, grain rotation and grain growth are suggested to play an important role in the deformation of nc materials. Grain rotation in nc metals has been predicted by computer

simulations [81-87] which is in agreement with the GB sliding and rotation of grains accompanying plastic deformation of mc and nc materials as observed by [87-109].

Schiotz and Jacobsen reported an increase in the strength of nc materials with 10 nm grain size [110]. They attribute this behavior to a change in deformation mechanisms from dislocation-based mechanisms to GB sliding when the grain size falls below 10 nm, which was confirmed by another study which the same change of mechanisms by decreasing the grains size in nc materials was found [111]. It is also reported that GB sliding needs to be accompanied by dislocation movement or atom shuffling to ensure the geometric compatibility [92].

Grain growth is also one of the possible mechanisms in deformation of nc materials. Nc materials are not thermodynamically stable and have a high density of GBs and it has been reported that grain coarsening may happen through GB migration in nc materials at room temperature [112] or under stress [113]. This mechanism affects the mechanical properties of the nc material, for example, Gianola et al. [114] reported an enhanced ductility coupled with a reduced strength of nc Al thin films due to stress-assisted grain growth.

Zhu et al. have modeled the decrease of hardness during nanoindentation creep of Ni and Cu by considering grain growth [115]. Grain growth can arise from grain rotation where adjacent grains rotate to align their own orientation. This process produces larger grains where the previously existing GBs are replaced by high density dislocation areas yielding softer material [116].

Qualitative in-situ TEM experiments were also performed to study the deformation mechanisms in nc metals [87-96]. Despite extensive MD simulations and experiments including in-situ TEM, still many aspects regarding the deformation mechanisms in nanoscale materials are unclear.

One of the most important aspects that has received major attention in the last years is related to GB mediated processes including grain rotation. Hattar et al. [97,98] used in-situ TEM tensile deformation for ufg Al. They observed the motion of bend contours during deformation. They related the motion of the bend contours without dislocation activity to the elastic region of deformation and the combined motion of dislocations and bend contours to the plastic region of deformation. They also associated the motion of bend contours to GB mediated processes such as grain growth and grain rotation [97,98]. Moreover, Wang et al.

[99] reported the grain rotation and grain rotation/growth in nc Ni using nanobeam electron diffraction and a series of dark field (DF) images during in-situ TEM tensile deformation. Therefore, stress assisted grain growth due to grain rotation is known as an efficient mechanism to accommodate plastic deformation in small grains [97-108]. However, they did not consider the overall bending of the sample for the grain rotation analysis. Very recently, Mompiou et al. [109] applied in-situ TEM tensile experiments on dislocation free ufg Al thin films with a mean grain size around 250 nm. Their results show that at small plastic strains, intergranular plasticity occurs. It consists of the nucleation and motion of dislocations inside all types of GBs. However, they could not provide a solid proof showing the grain rotation and the amount of rotation in the microstructure.

Moreover, most published microstructural observations obtained during in-situ deformation in TEM are based on BF or DF techniques which are both of diffraction contrast type. Therefore, it is difficult to obtain clearly the grain rotation during in-situ deformation by using such BF and DF images. To overcome this issue in this thesis, the investigation of the grain size distribution as well as the crystallographic texture have been performed using automated crystal orientation mapping in TEM (ACOM-TEM) to obtain full orientation maps with nanometer resolution.

In summary of deformation mechanisms in nc materials, Fig. 1.13 shows a schematic overview of possible plasticity mechanisms in nanograins including grain rotation, GB sliding (shear), SF formation, nucleation of dislocations and twinning. In the present thesis, a detailed micro/nanostructural analysis using advanced TEM techniques on nc Pd films which have been deformed by different processes has been performed to unravel the responsible plasticity mechanisms. These results provide insightful information to guide the generation of microstructures with an enhanced strength/ductility balance in high SFE nc metallic thin films as needed for instance in Pd-based membranes. The nc Pd thin films used in the present project are a very good candidate for hydrogen purification and sensing applications. However, although several experimental studies have been dedicated to the study of the effect of hydrogen on the microstructure and mechanical properties of bulk coarse-grained Pd [104-107], quantitative experimental data on the elementary plasticity mechanisms activated in nc Pd thin films under hydrogen loading is still missing in the literature. This is a critical point since these mechanisms may strongly differ from those reported in bulk coarse-grained Pd due to the small grain size and the predominance of GBs and TBs in nc Pd films.
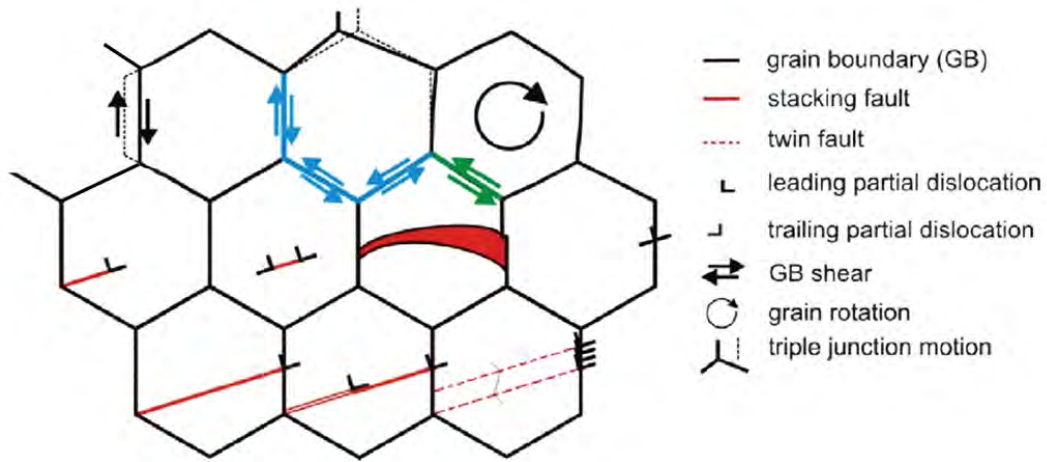
Figure 1.13 Schematic illustration of possible plasticity mechanisms in nc metals [after 47].

Chapter 2

2. Materials and Methods

2.1. Preparation of nc Pd thin films

2.1.1. Processing of nanocrystalline materials

The interest in ufg and nc materials has grown over the past decades. This is due to the special functional properties they exhibit with decreasing grain size. There are different effective techniques to produce ufg and nc materials for both research and industrial applications such as mechanical alloying (i.e., cryomilling and compaction) [110-120], severe plastic deformation (SPD) [121], gas-phase condensation of particles and consolidation such as physical vapour deposition (PVD) [122-124], and electrodeposition [125,126]. The first two techniques are mostly used to produce ufg material, however, the latter two, are used to produce nc material. Cryomilling using liquid nitrogen as mechanical alloying method has been mostly used to produce ufg Al alloys [120]. Using the mechanical alloying technique, it is possible to produce billets of material with reasonable size, however, it is difficult to control the impurity of the material during processing [120].

The SPD technique is also used to produce ufg materials with an average grain size in the range of 150-300 nm or more via torsion, multiple extrusion or multiple forging. Since, the starting material can be controlled, it does not suffer from impurity of the material after being processed. SPD has been used to process different metals and alloys such as Al alloys, Cu, Ni and Ti and its alloys (such as Ti-6Al-4V), steels and intermetallic compounds. Since the SPD technique applies an extensive and repeated deformation stress on the material, the processed materials contain highly distorted microstructures and high-angle GBs, which will affect the mechanical properties of these materials [121].

Gas-phase condensation or inert gas condensation [122-124] is another method which is used to produce nc metals including Cu, Ni and Pd. Powder particles with an average grain size in the range of 5–50 nm are produced by condensing the vapor phase using this technique [121]. Then, they are consolidated using high mechanical and/or thermal forces from compressing or heating the condensed powder particles. This technique suffers from some disadvantages such as the limitation in specimen volume, existence of impurities in the particle boundaries, incomplete densification, which causes the formation of porosities and difficulties in controlling the initial grain size after consolidation [121].

PVD and electrodeposition have also been used to produce nc thin films such as Ni, Co, Cu, Pd and binary alloys such as Ni-Fe and Ni-W [126,127]. The PVD method mostly leads to a narrow grain size distribution. It is also possible to produce different types of morphology

such as a columnar structure and/or clusters of grains with minimal misorientation between each other by changing the process parameters. In recent years, improvement and development of PVD and electrodeposition techniques for the production of nc metals has received more attention in comparison with the inert gas condensation method, since they avoid the formation of pores [121].

In the following section, the two most important PVD deposition methods which are used to produce the nc Pd thin films investigated in this thesis will be explained. These two techniques include evaporation and sputtering.

2.1.2. Evaporation

Evaporation is a technique which thermally removes the atoms from the source material after which they are deposited by condensation on a substrate located in front of the source [120]. This procedure is carried out inside a chamber under high vacuum conditions (around 10^{-7} mbar) which prevents the incorporation of gaseous impurities inside the deposited film. Therefore, high evaporation rate and high vacuum conditions during evaporation decrease the amount of impurity in the deposited film [128].

The evaporation of the material is one of the main concerns of this technique. There are two different methods to evaporate the source material. The first one is using resistively heated elements. However, using such heating sources leads to contamination from evaporated material originating from the crucibles, the heaters and the surrounding materials. Moreover, resistive heating is limited by the melting temperatures of the materials. Materials with higher melting points will be evaporated with lower rates which decreases the purity of deposited films [121,128].

The second technique for the evaporation of the source material is using an electron beam to locally heat the source material. Electron beams are emitted by the heating of a tungsten filament and then electromagnetic fields is used to accelerate and focus the electrons. Theoretically, it is possible to evaporate all materials at any rate using an electron beam. The e-beam evaporation induces local evaporation of source materials, therefore, it leads to the deposition of pure thin films. In this thesis, the e-beam evaporation technique was used to deposit the Pd films. The evaporation process does not allow varying deposition parameters over a wide range and only the deposition rate can be altered [128].

2.1.3. Sputter deposition

The other technique for production of nc thin films using PVD is sputtering. This method includes the removing of the atoms by the bombardment of a solid or liquid source by energetic particles, mostly ions. When an ion arrives at the surface of the target, a plume of material is released. This phenomena is called sputtering [128].

The target material is connected to the negative terminal of a direct current (DC) or radio frequency (RF) power supply. The target material thus acts as the cathode in the system. Typically, several kilovolts are applied to accelerate the ions. The substrate where the sputtered atoms will deposit faces the cathode.

After adjusting the vacuum in the chamber, a gas, typically argon, is introduced into the chamber. Gas pressure usually ranges from a few to 0.13 mbar. This environmental condition is used to produce and sustain a plasma [128]. This plasma consists of argon atoms, positively charged argon ions and free electrons. The plasma ions are accelerated towards the negative target material where they remove the atoms of the source material by sputtering. Sputtered atoms carry more energy in comparison with evaporated atoms, therefore, the sputtered films have generally a higher density than evaporated films. However, the higher energy of sputtered atoms leads to an increase of the temperature of the substrate during film deposition, which can affect its structure and morphology.

The other advantage of the sputtering technique in comparison with the evaporation method is the flexibility of the deposition parameters such as the Ar pressure and the temperature of the substrate which can be controlled. The latter leads to better adhesion of material on the substrate. Therefore, the microstructure of the film deposited by sputtering can be easily controlled compared to the evaporation method [128].

The sputtering technique can further be categorized in three different methods:

1) DC sputtering which includes applying a continuous current between the anode and the cathode.

2) RF sputtering is used for deposition of thin films of non-conducting materials (such as oxides). In order to avoid the charge build-up on insulating targets, the sign of the anode-cathode bias is varied at a high rate using this technique.

3) Magnetron sputtering utilizes strong electric and magnetic fields to confine charged plasma particles close to the cathode. In a magnetic field, electrons move along helical paths, undergoing more ionizing collisions with Ar atoms. The extra Ar ions created as a result of these collisions lead to higher deposition rates.

2.2. Transmission electron microscopy (TEM)

2.2.1. Introduction

TEM is a very powerful and common technique for the observation of the internal structure of materials and crystal defects such as dislocations, SFs, twins, voids and GBs. TEM was first developed by Ernst Ruska and Max Knoll in the 1930's. TEM operates on the same basic rules as a light microscope, however, an electron beam is used instead of light and electro-magnetic lenses are used instead of glass lenses in order to magnify and focus the beam and projected image. A typical TEM consists of an electron gun, the condenser lens system, the specimen stage and the imaging system, which are shown schematically in Fig. 2.1. As a result of the particle-wave duality principle, an electron beam of energy E can indeed be considered as a wave with wavelength λ (m) using the de Broglie equation as follows:

$$\lambda = \frac{h}{\sqrt{2m_\circ eE}}$$
(2.1)

where $m_\circ$ is the rest mass of the electron (kg), e is the elementary charge and h is Planck's constant (J.s). In view of the high voltage used, the latter equation needs to be written in relativistic terms, the unit of λ in the equation below is "nm":

$$\lambda = \frac{1.22}{\sqrt{E}}$$
(2.2)

The electrons are generated by the electron gun with a specific range of energy (order of several hundred V). Then, the electron beam is condensed using the condenser lens system to form a small spot on the sample. After the electron beam hits the specimen, it interacts with the specimen structure and yields an enlarged projected image of the material's internal structure in the image plane. The possibility for observing small objects depends on the resolution of the microscope, defined as the closest distance between two points which can be distinguished through the microscope and which for a TEM is much better than for a light microscope. The theoretical resolution "r" (m) is proportional with the wavelength of the probe based on the Rayleigh criterion [129]:

$$r = \frac{0.61\lambda}{\mu sin\alpha} \tag{2.3}$$

where λ (m) is the wavelength, μ is the refractive index of the medium between the object and the objective lens and the semi-angle α is referred to the microscope apertures. Therefore, it is clear that to obtain a better resolution, one needs to decrease λ and/or increase μ and/or α. A high energy electron beam has a much smaller wavelength than light (factor of many thousands). On the other hand, the medium in the TEM is vacuum, so the refractive index is constant and equal to 1. Furthermore, the angle at which the rays are reflected is very small, therefore sinα≈tanα≈α. These simplifications in the case of TEM yield:

$$r = \frac{0.61\lambda}{\alpha} \tag{2.4}.$$

By using the wavelength of an electron accelerated by 100 kV (λ=0.0037 nm) and α=0.02 radians (around 5 degree), it is theoretically possible to have a resolution of 0.1 nm using TEM which is smaller than the typical distances between two adjacent atoms in a crystal [129].
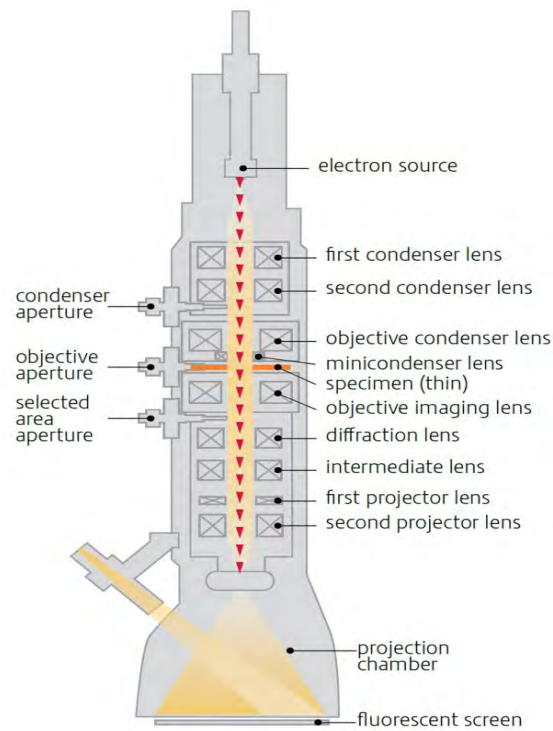
Figure 2.1 A cross-sectional view through a conventional transmission electron microscope [129].

The electron source (electron gun) produces the electrons which travel toward the specimen in the form of either a broad parallel beam or a focused beam using two or three condenser lenses (C1, C2, etc.). In the conventional TEM mode, the first two condenser lenses are used to illuminate the specimen with a parallel electron beam as shown in Fig. 2.2(a). As shown in this figure, the electron beam is not exactly parallel to the optic axis but the value of α is less than 10^{-4} radians (0.00578 degrees), which can be considered as a parallel beam.

In practice, there is another so-called condenser-objective lens in the upper objective pole-piece which can be considered as the C3 lens. The C1 and C2 lenses are used to image the source at the front focal plane of the condenser-objective lens, thus a true parallel beam can be created at the specimen plane using the condenser-objective lens C3 (Fig. 2.2(b)).
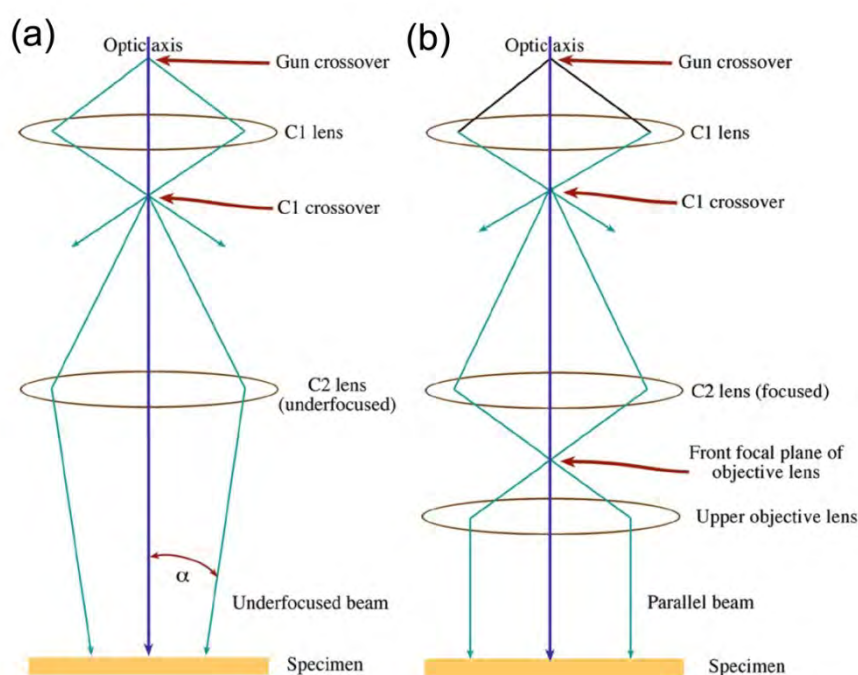
Figure 2.2 (a) Schematic illustration of a parallel beam in TEM (a) The basic principle of formation of a parallel beam in TEM using C1 and C2 lenses (b) Practical situation in TEM for creating the parallel beam on the specimen using three condenser lenses [129].

In order to form an image of the specimen, there is an objective lens below the specimen which collect the transmitted electrons from the exit surface of the sample. The objective lenses are used to create a diffraction pattern (reciprocal space) in the back focal plane and an

image (real space) in the image plane as shown in Fig. 2.3. In order to project the DP on the screen, the intermediate lens should be adjusted in a way that the back focal plane of the objective lens is considered as an object for the intermediate lens (Fig. 2.3(a)). Alternatively, by adjusting the intermediate lens in the way that the image plane of the objective lens is considered as the object plane for the intermediate lens, the image of the specimen is created on the screen [129].

It should be noted that the imaging systems shown in Fig. 2.3 are highly simplified. In most TEMs, many more projection lenses are used which give better flexibility and larger ranges for magnifying.
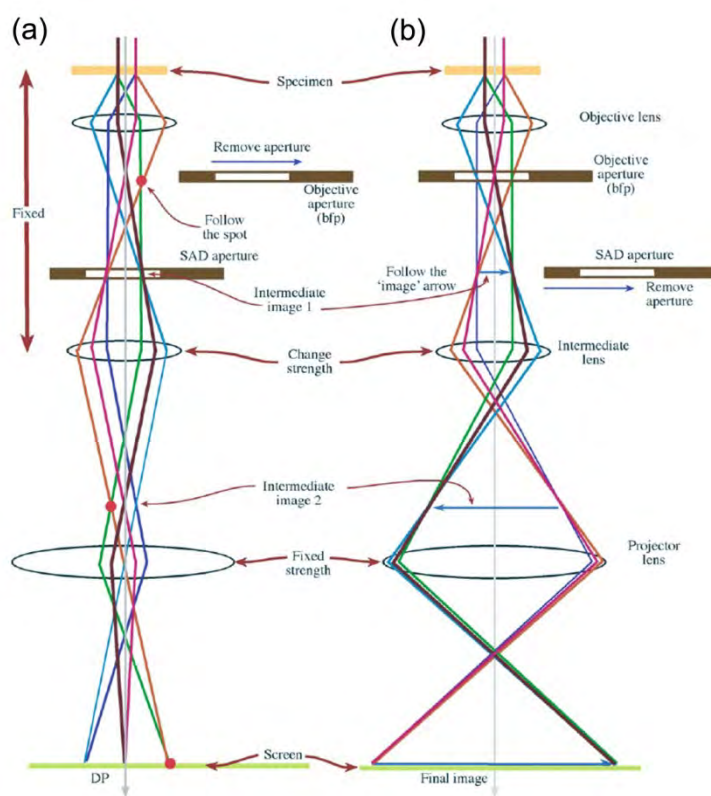
Figure 2.3 The two basic operation modes used in TEM for (a) projection of the diffraction pattern and (b) projection of the image onto the viewing screen [129].

2.2.2 Aberrations in TEM

There are many kinds of lens defects which will affect the image and/or the DP. However, the ones that affect the performance of the microscope in substantial ways are spherical aberration, chromatic aberration, and astigmatism:

2.2.2.1. Spherical aberration

Since even a perfect electromagnetic lens has cylindrical symmetry it behaves differently for the various off-axis electron beams, as is the case for any round lens as first mentioned by Ernst Abbe in 1881 [130]. The electron beams with higher deviation from the optic axis are more strongly bend toward the axis than beams closer to the optic axis. Therefore, a point object will be imaged as a disc in the image plane (Fig. 2.4). This imperfection is called spherical aberration. The radius of the spherically aberrated disk (r_{sph}) in the image plane can be written as:

$$r_{sph} = C_s\beta^3 \tag{2.5}$$

where C_s is the spherical aberration constant and β is the maximum deviation angle of the electron beam from the optic axis. In order to decrease the effect of spherical aberration, an objective aperture is inserted to block the high angle electron beams (β decreases).

Moreover, in order to completely correct the spherical aberration in an electron microscope, a corrector can be introduced which produces negative spherical aberration. This then combines with the positive aberration of the lens to give a total of zero spherical aberration. Therefore, all electron beams are brought to a common focus and a sharp image can thus be formed.
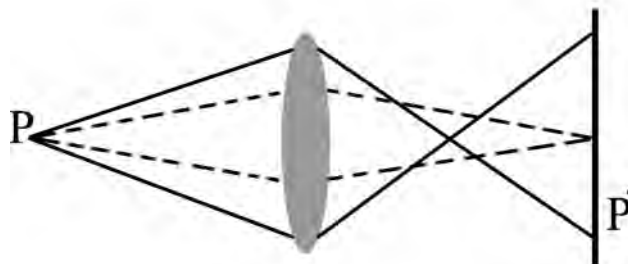
Figure 2.4 Schematic illustration of spherical aberration. The rays far from the optic axis of the lens (solid lines) bend stronger than the ones close to the optic axis (dashed lines). A point object (P) will thus be imaged as a disc (P') in the image plane.

2.2.2.2. Chromatic aberration

The chromatic term is related to the "color" of the electrons originating from the (small) difference in frequency, wavelength, or energy of both the incoming electrons and electrons that experience energy loss in specimen. The objective lens will bend the low energy electrons stronger than high energy electrons. Therefore, similar to spherical aberration, a point object will become blurred (disk-shaped) in the image plane. The radius r_{chr} of this disk can be given by:

$$r_{chr} = C_c \frac{\Delta E}{E_\circ} \beta \qquad\qquad (2.6)$$

where C_c is the chromatic aberration coefficient of the lens, ΔE is the energy variation of the electrons, E_0 is the initial energy of the primary electron beam, and β is the collection angle of the lens. The variation of the electron energy (ΔE) can be due to intrinsic features in the source of the primary electrons but also to the sample where energy loss processes can take place. Monochromating the source is a solution to correct chromatic aberration originating from the electron source. For the energy loss part, chromatic aberration gets worse for thicker specimens because the range of ΔE is increasing. Therefore, the use of thin specimens minimizes the effects of this aberration.

2.2.2.3. Astigmatism

Astigmatism occurs due to a non-homogenous magnetic field of the lenses originating from an asymmetry shape (coming from manufacturing steps), microstructural inhomogeneities of the lenses or external fields. Besides, the apertures may also disturb the magnetic field if they

are not precisely centered around the optic axis and/or they are not perfectly clean. Consequently, the image will become distorted by the amount of r_{ast} :

$$r_{ast}=\Delta f.\beta \qquad\qquad\qquad (2.7)$$

where Δf is the maximum difference in focus induced by the astigmatism and β is the angle of collection of the lens. Astigmatism can be easily corrected by stigmators which produce a compensating field to balance the inhomogeneities in the magnetic field.

2.2.3. Imaging in TEM

In the following sections the electron imaging and diffraction processes relevant for the present work will be discussed.

2.2.3.1. Electron Specimen Interaction

When the electrons hit the sample, they strongly interact with the atoms of the material. The deflection or scattering does not necessarily involve an energy transfer (no energy loss) in which case the scattering is elastic. If energy is lost during scattering of the electron beam, the scattering is called 'inelastic'. Due to the strong nature of the electron-matter interactions, the scattered electrons themselves might be elastically or inelastically scattered further within the specimen. The probability of a second scattering (or even more) will increase with the sample thickness. Elastic scattering at the electron cloud of the atoms in the sample is the main scattering mechanism used to produce reciprocal space DP and real space images.

Elastically scattered electrons are used for conventional TEM imaging, reciprocal space imaging and HRTEM imaging. During the transmission of the electron wave through the sample, its amplitude and phase will change which will contribute to the image contrast. Thus, the formation of the image in TEM can be due to amplitude contrast or phase contrast. Diffraction contrast is only contributing to amplitude contrast, however, mass-thickness contrast can be based on both amplitude and phase contrast. Mass-thickness contrast is mostly applied for imaging in non-crystalline materials such as polymers and biological materials where local differences in density and atomic number lead to different absorption. On the other hand, diffraction contrast is widely used for imaging of crystalline material (such as Pd investigated in this thesis).

2.2.3.2. Diffraction contrast
Bragg's law

W. L. Bragg investigated the diffraction in crystals by considering the reflection of an X-ray beam from atomic planes. Due to the wave-nature of electrons, the same principle holds for electron diffraction (ED). Figure 2.5 shows horizontal crystal atomic planes with spacing d. The incident electron plane wave with wavelength λ interacts with the atoms and can be considered to reflect at an angle θ equal to the incoming angle. Since, the scattering within the crystal lattice generates a phase difference constructive interference and maximum intensity will occur when the difference in travel distance between reflections on two successive planes (2dsinθ) equals an entire number of wavelengths:

$$2d\sin\theta = n\lambda \qquad\qquad (2.8)$$

The equation (2.3) is referred to as Bragg's law and θ is known as the Bragg angle.
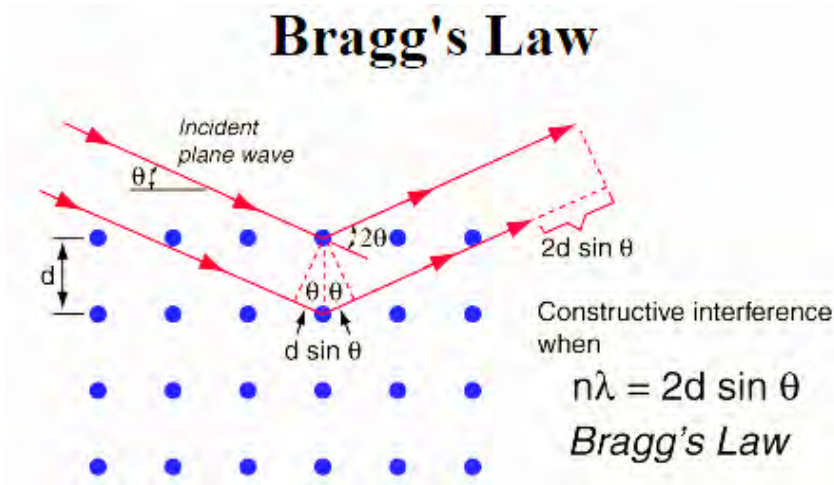
Figure 2.5 Schematic illustration of the reflection of an electron beam at an atomic plane based on Bragg's law.

The configuration of TEM for obtaining the DP was explained in section 2.2.1. ED is a very common and useful method to investigate different characteristics of the material such as being crystalline or amorphous, measuring lattice parameters, determining symmetry and orientation of each grain, distinguishing between different phases, etc.

The DP forms at the back focal plane of the objective lens. When the incident beam satisfies the Bragg law of a particular family of planes, the electron beam diffracts at the atomic plane and appears as a reflection in the DP (Fig. 2.6). The distance between the central spot of the non-diffracted beam and the different diffraction spots is proportional to the inverse of the inter-planar distances in the crystal lattice. In order to index the DP, the distance and the angle of each spot from the central spot are measured and transferred to real space after calibration of the camera length of the microscope. The full crystal structure of the specimen can be determined by indexing different DPs obtained along several orientations.
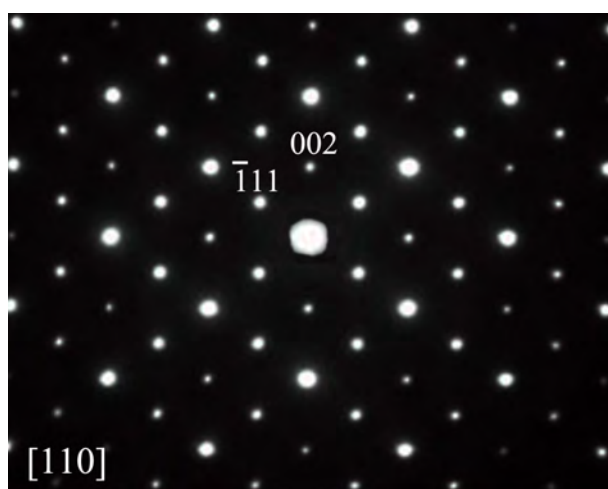
Figure 2.6 An example of a diffraction pattern (obtained from a Cu fcc crystal viewed along the [110] direction), showing the direct beam as central intense spot and many diffracted spots reflecting from different atomic planes, of which two are indexed.

The DP is in principle obtained from the area where the sample is illuminated by the electron beam. In order to limit the volume of material from which the DP originates, a specific region of the specimen can be selected by a selected-area aperture. This mode of operation is called selected-area diffraction (SAD) or selected-area electron diffraction (SAED). The SAD aperture is shown in Fig. 2.3(a) where it is inserted in the image plane of the objective lens.

2.2.3.3. Bright field and dark field imaging

There are two basic imaging operation modes in TEM called bright field (BF) and dark field (DF) imaging. An objective aperture is inserted into the back focal plane of the objective lens by which one can either select the central spot (BF image) or a diffracted spot (DF image).

In the case of the BF imaging mode, shown in Fig. 2.7 (a), some of diffracted spots are blocked by the objective aperture except the central beam. Therefore, the image contains a bright background with dark regions, the latter corresponding to the areas in which the lattice planes are satisfying Bragg's law and the corresponding spots are blocked by the aperture. Contrary, if a diffracted spot is selected by the objective aperture (Fig. 2.7(b)), an image forms containing a dark background with bright regions, the latter corresponding to the selected spot.
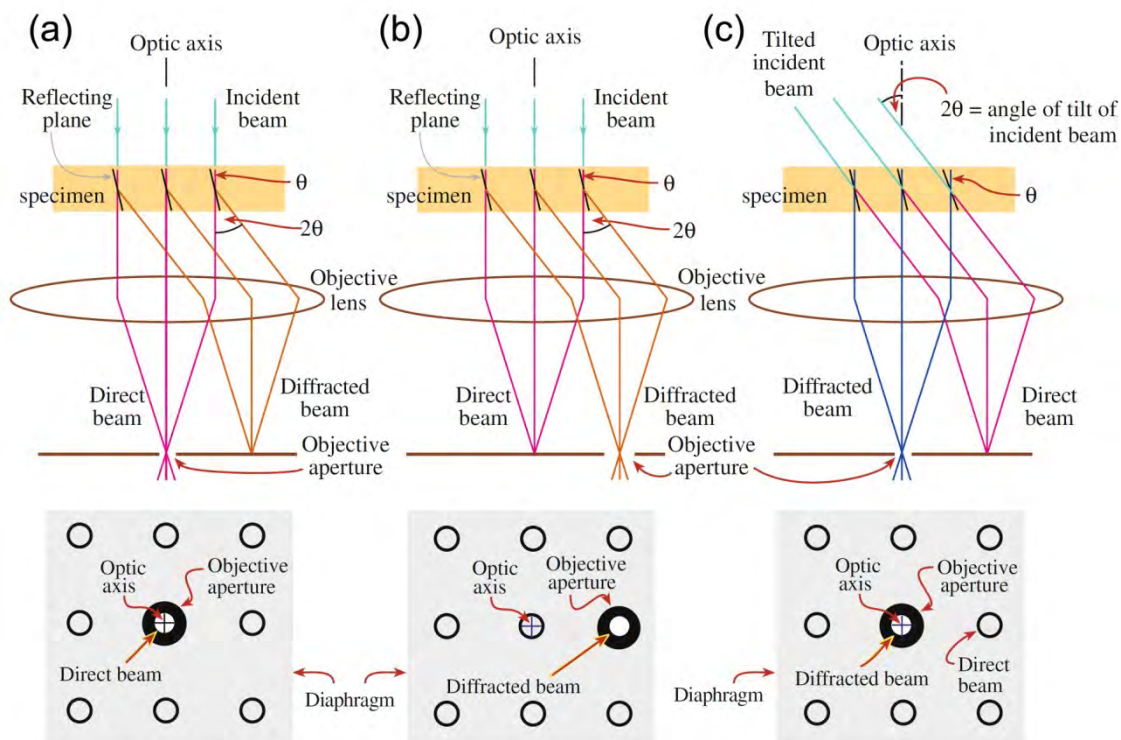
Figure 2.7 Schematic illustration showing the formation of (a) a BF image by selecting the central beam using an objective aperture (b) a DF image by moving the objective aperture to the diffracted spot to be selected and (c) a CDF image by tilting the electron beam in a way that the selected scattered beam remains on the optic axis [129].

In the case of a DF image, the aperture is displaced for selecting the diffracted spot. Since, off-axis electrons will cause high aberration and astigmatism, it will become difficult to obtain high quality images. In order to avoid this, a method called centered DF (CDF) is used. In this mode, the incoming beam tilt is adjusted by potentiometers above the objective lens in such a way that the incident beam hits the sample at an angle equal and opposite to the scattering angle. Thus, the scattered electron will become parallel to the optic axis as shown in Fig. 2.7(c) which yields a higher quality image.

2.2.3.4. High resolution TEM (HRTEM)

HRTEM is a powerful tool which allows direct imaging of the atomic structure of different materials such as semiconductors, metals, nanoparticles, etc. A HRTEM image is formed by the interference of all electrons passing the objective aperture and thus relies on the difference between the phases of electrons leaving the sample, hence the term phase contrast. However, any additional phase shift between the sample and the viewing screen will make the HRTEM image hard to interpret. Therefore, lenses with a low degree of aberrations are needed for HRTEM.

In an interference pattern the phases of the electron waves are not directly recorded, only the amplitudes of the interfering beams. By selecting a particular focal value of the objective lens the phase of the interacted electron waves with sample is converted to an image of the amplitude in the image plane. This conversion occurs through the phase contrast transfer function (CTF). Figure 2.8 shows the CTF function versus **u** as reciprocal lattice vector. CTF(u) is zero at **u**=0. If CTF(u) is large, it means that information with a periodicity or spatial frequency corresponding to that value of **u** will be strongly transmitted and thus will appear in the image. This CTF can be described by using the Williams and Carter [129] equation shown below:

$$CTF(u) = A(u).E(u).\sin(\chi(u)) \tag{2.9}$$

where **u** is a reciprocal lattice vector, A(u) is the aperture function, E(u) describes the attenuation of the wave for higher u (also referred to as the envelope function) and χ(u) is a function of the aberrations of the microscope. If we consider that only spherical aberration and defocus are contributing in χ(u), this function can be written as:

$$\chi(u) = \frac{\pi}{2} C_s \lambda^3 u^4 + \pi \Delta f \lambda u^2 \tag{2.10}$$

where C_s is the spherical aberration coefficient, λ is the electron wavelength and Δf the defocus of the objective lens.

The maximum of transmitted spatial frequency as dictated by the envelope function determines the information limit of the microscope. In practice, the aperture function (A(u)) cuts off the scattered electrons above a certain angle and will correspond with the size of the actual objective aperture used in the experiment [129].
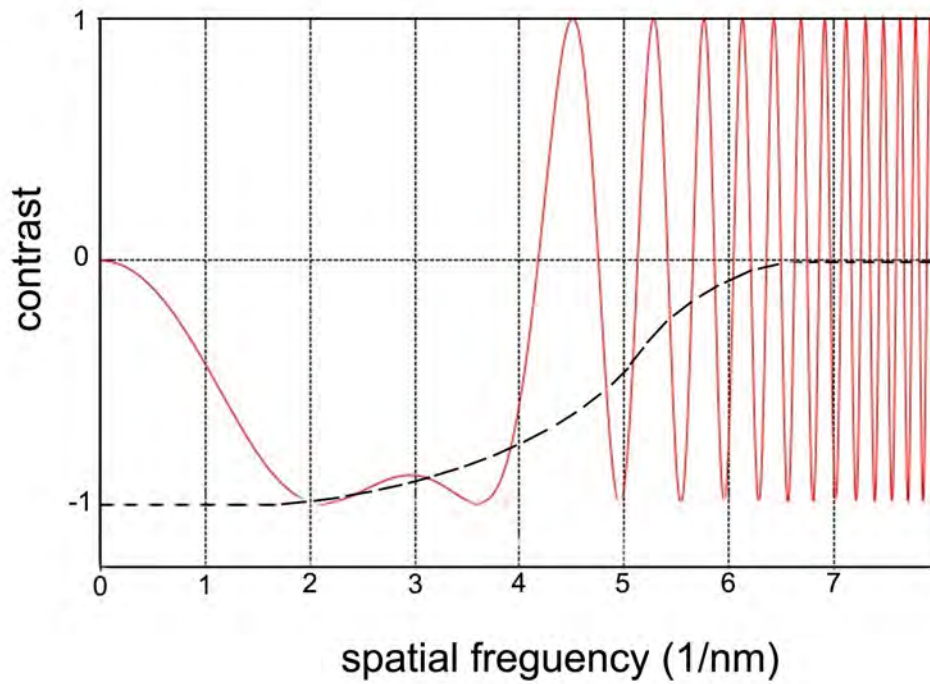
Figure 2.8 Schematic illustration of the contrast transfer function versus **u**.

Scherzer optimized the transfer function by balancing the effect of spherical aberration with a negative value of Δf which is known as Scherzer defocus:

$$\Delta f_{Sch} = -1.2(C_s\lambda)^{\frac{1}{2}} \tag{2.11}$$

At this defocus value, all electron beams within a maximum spatial frequency range at the exit plane of the sample will have a similar phase as seen from the plateau in the CTF in Fig. 2.8. It can be concluded from eq. (2.11) that the optimum defocus of the microscope depends on microscope properties such as spherical aberration C_s and the accelerating voltage (through λ). Therefore, by adjusting the defocus value and the objective aperture to cut off the high

index spots that fall within the strong oscillating part of the CTF, i.e. beyond the Scherzer plateau, it is possible to obtain HRTEM images with atomic resolution.

From an experimental HRTEM image it is further possible to obtain a Fast Fourier Transform pattern (FFT pattern) by selecting a desired region in the image. The FFT pattern is similar to the diffraction pattern representing the 2D slice through reciprocal space. By indexing the obtained FFT pattern, it is possible to determine the crystal symmetry and crystallographic orientation of a nanograin, while this can be impossible to obtain using a conventional SAD pattern due to the limited size of the SAD aperture [129].

2.2.3.5. Analytical TEM

As explained in section 2.2.3.1, when the electron beam interacts with the specimen, different types of signals are produced. Some of these signals can be used for chemical analysis of the specimen using different methods such as Energy Dispersive X-Ray Spectroscopy (EDS or EDX) and Electron Energy Loss Spectroscopy (EELS).

2.2.3.5.1. Energy Dispersive X-Ray Spectroscopy (EDS)

When an atom is bombarded with an electron beam, the atom can release some of the absorbed energy as X-rays. Due to inelastic scattering an inner shell electron can be removed from the atom, yielding a vacancy in the respective shell. In order to return the atom to its low energy state, an electron from an outer shell can move into the inner shell to fill the vacancy. This results in the release of a specific amount of energy, usually in the form of X-rays which can be measured by dedicated detectors, which convert the X-ray energy into an electronic count. The accumulation of these energy counts creates a spectrum representing the chemical analysis of the sample. Since each element has a set of specific energy levels, it is possible to determine the chemical composition of the material. The intensity of the X-ray spectrum of an element is proportional to the concentration of the element in the material. Therefore, a quantitative analysis of the elements can also be obtained, although care has to be taken for distorting features such as Z-dependent absorption, ghost peaks, … . In view of the limited energy resolution and extended energy range EDS is mostly used for detecting heavy elements and will not be used in the present work, where the focus is on known Pd metal material and hydrogen.

2.2.3.5.2. Electron Energy Loss Spectroscopy (EELS)

This technique is based on the analysis of the energy distribution of inelastically scattered electrons. These electrons, as the X-rays above, carry useful information about the chemistry of the studied atoms and also about their electronic structure (due to the higher energy resolution when compared to an EDS detector). This information can be used for detection of the nature of atoms and their bonding. An example of an EELS spectrum is shown in Fig. 2.9. There are three principle energy regions which should be considered in the EELS spectrum. The first one is the zero-loss peak which corresponds to the elastically scattered electrons. Since this peak is very intense and can damage the coupled charge device (CCD) of an EELS detector, care has to be taken when gathering the spectra. As seen from Fig. 2.9, there is a small plasmon peak immediately next to the zero-loss peak referred to as the low-loss region. It is clear that this and other useful peaks in EELS spectrum have much less intensity than the zero-loss peak, which is a disadvantage of this technique.
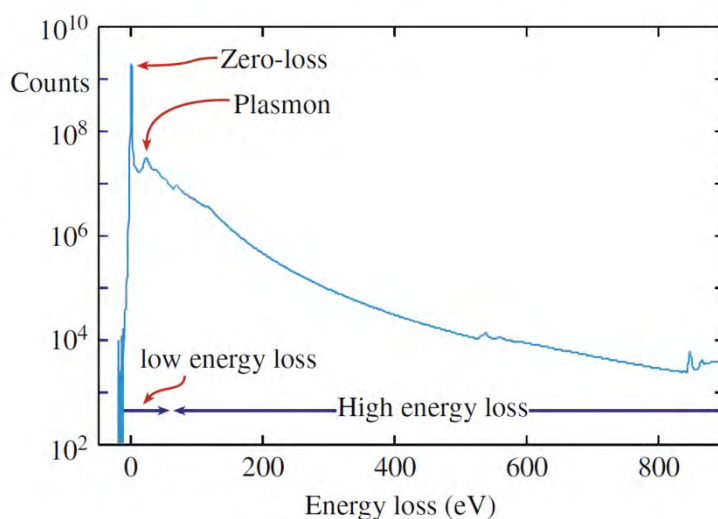
Figure 2.9 An example of an EELS spectrum displayed in logarithmic intensity mode [129].

This low-loss region has an energy loss up to ≈50 eV. The loss of energy is due to the interaction of the electrons with the weakly bonded outer shell electrons or plasmon oscillations. Using the zero-loss peak and the plasmon peak, the local thickness of the sample can be calculated.

The third region in an EELS spectrum contains the peaks in the high-loss region (more than 50 eV) which are due to the inelastic interactions of electrons with the inner or core shells of the atoms. As for the X-rays in EDS, the lost energy of the primary electrons varies with the atomic number (Z), so the positions of the peaks (usually referred to as edges) are different for various elements. Again the height (or better surface) of the peak after background correction corresponds to the concentration of a given element. It is thus possible to identify each element as well as the chemical composition of the material using the EELS spectrum. Moreover, due to the high energy resolution of an EELS detector, the shape of the edge contains information on the bonding in the sample [129]. In view of the high energy resolution and limited range EELS is mostly used for detecting light elements and will be used in the present work for the detection of possible hydrogen atoms in the lattice.

In the present thesis, conventional BF, DF and HRTEM characterizations of the samples were carried out using a TECNAI G2 (FEG microscope) operating at 200 kV. Further detailed experiments including atomic structure of crystal defects and analytical TEM investigations using EELS were performed using a FEI Titan 80-300 "cubed" microscope with aberration correctors for imaging and probe. This machine offers a spatial resolution of 0.5 Å in TEM mode.

2.3. Automated Crystallographic Orientation Mapping in a TEM (ACOM-TEM)

The ACOM-TEM technique uses small probe TEM diffraction spot patterns as an effective method for mapping phase and crystal orientation. This technique is an alternative to Orientation Imaging Microscopy (OIM) methods using Electron Backscattered Diffraction (EBSD) or Kikuchi lines in scanning electron microscope (SEM) [131,132]. It exhibits a characteristic resolution length scale of the order of nm, which is far too small to be readily available by EBSD on a SEM platform. Moreover, in the case of the investigation of deformed samples (also studied in this thesis) which contain a high concentration of lattice defects, it is very difficult to observe the region of interest (ROI) by conventional SEM-EBSD as this technique is based on the identification of backscatter Kikuchi diffraction patterns of which the contrast is very sensitive to the density of crystal defects. However, nc deformed samples can be more easily investigated using TEM.

Using ACOM-TEM, the electron beam in combination with the beam precession is scanned over the sample and the DPs are collected from different regions of the sample. The obtained DPs are compared with pre-calculated DP templates by using cross-correlation techniques and the best match is selected. Thus, the local crystal orientation of a single grain can be determined [133]. In order to eliminate the ambiguity that can exist for highly symmetric orientations, a build-in clean-up procedure in the OIM TSL® software from EDAX has been used. By using this clean-up procedure a single orientation for each ambiguous situation is selected.

The grain size distribution as well as the crystallographic texture of the Pd films were investigated by ACOM-TEM using a Philips CM20 equipped with a LaB_6 gun at 200 kV installed at the Free University of Brussels (ULB).

2.4. TEM sample preparation

Sample preparation is one of the most important steps for TEM analysis. The sample or the ROI should be electron transparent. The common thickness for metallic TEM samples for HRTEM is in the range of 30-50 nm. Furthermore, the prepared TEM sample should be mechanically robust for handling. The prepared TEM sample originating from a bulk sample is self supported, however, TEM samples made from nanopartical or thin films need to be mounted on a grid or support. Copper supports are mostly used, however, for heating experiments Mo supports are often used. In the case of nanoparticles and nanotubes which are already thin enough for TEM investigation, carbon grids are used due to their low contrast in TEM.

The most common way to prepare the TEM sample from a bulk material starts by thinning the sample to an initial thickness of 100-200 μm (by mechanical grinding). Then, a 3 mm disk is cut and further thinned by different techniques to yield electron transparency. These techniques include electrolytic polishing for conducting materials and/or ion milling for non-conducting materials.

In the case of thin films with the film thickness in the range of 150-300 nm (the samples investigated in this thesis), SEM/FIB dual-beam was used to prepare the TEM samples for the present work. This technique has the advantage over other techniques since one can tilt the specimen to any angle to minimize beam damage while the imaging capability allows the so-

called site-selected concept where a micron-sized sample can be prepared from any well-defined location in a sample.

2.4.1. Focused ion beam

Recently, small scale materials such as nc materials, nanoparticles, thin films, etc. are receiving more attention. Therefore, the FIB technique as a powerful sample preparation method for TEM has also obtained a broad interest. Most recent FIB machines combine the FIB column with a SEM column. Such an instrument is called a "dual-beam" FIB–SEM. Therefore, this instrument offers both high-resolution imaging and flexible micromachining in a single platform. The ion beam and the electron beam are aligned in such a way that both are converged at the same point of the sample with an angle of 52°. The schematic illustration of a dual beam FIB-SEM system is shown in Fig. 2.9. The ion mode consists of a finely focused ion beam which can also be used for imaging similar to a SEM. The ion beam is produced by a large negative potential between the liquid metal ion source (Ga-based) and an extraction electrode. Ga is commonly used in FIB due to its low melting temperature ($30^\circ C$) and low vapor pressure. An ion beam with low current is used for imaging in the ion mode. The ions interact with the surface of the sample and secondary electrons are emitted from the surface of the specimen (Fig. 2.10). These signals are collected by a detector to generate an image in ion mode [134].
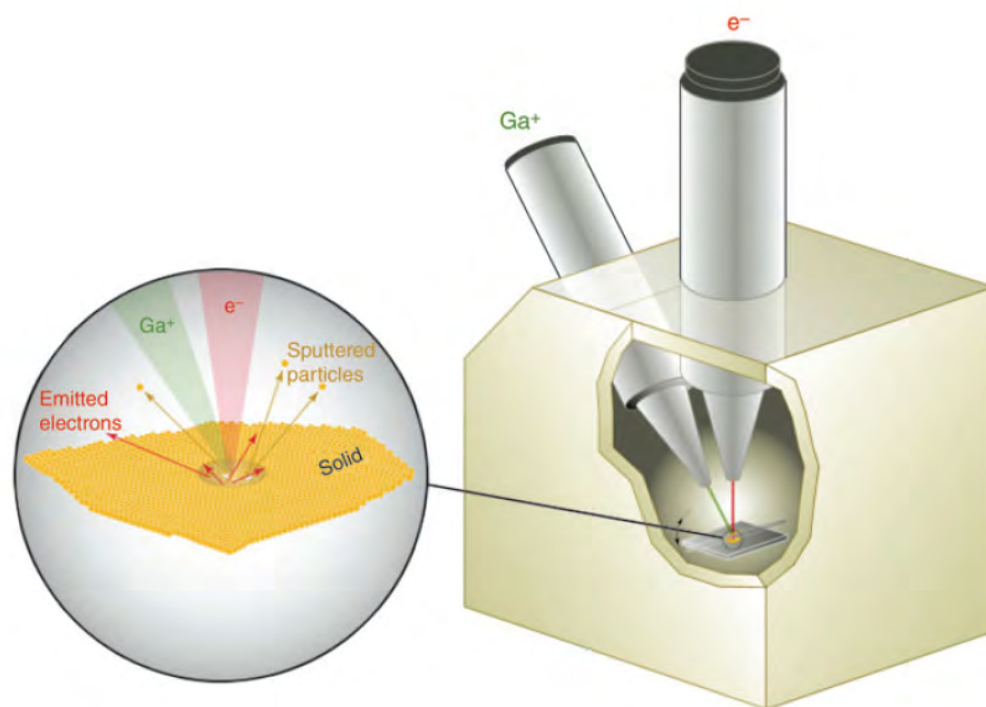
Figure 2.10 Schematic illustration of a dual-beam FIB–SEM instrument showing the interaction of the electron and ion beams with the surface of specimen [134].

Moreover, the ions generated at higher currents can be used for sputtering the surface and thinning the specimen. If the momentum of the ion becomes large enough to overcome the surface binding of the specimen atoms, the atoms will be removed from the surface of the specimen. Modern FIB-SEM machines also use gas-injection systems (GIS) for Pt deposition and an Omniprobe for removing the sample after cutting and moving to a TEM support.

Figure 2.11 shows the preparation steps of a TEM sample using FIB. First, a Pt protective layer is deposited using GIS by the ion or electron beam on the surface of the sample above the ROI (Fig. 2.11(a)) which is typically 10 to 15 micron long and 1.5 micron wide. The deposition of Pt using the electron beam is much slower than when using the ion beam, however, the kinetic energy of the ion beam is higher than that of the electron beam, so using the ion beam for Pt deposition may cause more damage to the surface of the specimen. Therefore, a very thin layer of Pt is first deposited using the electron beam and then the remaining Pt is deposited using the ion beam.

In the next step, the area around the ROI is removed using Ga^+ ions to create a thin lamella about 5 micron broad (Fig. 2.11(b)). By tilting the material the thin ROI can be cut free from

the remaining material (Fig. 2.11(c)). In the following step, the lamella is removed using the "lift out" technique of the Omniprobe (Fig. 2.11(d,e)). The needle of the Omniprobe is welded to the lamella by Pt deposition. In order to easily handle the prepared FIB sample, a copper support is used (Fig. 2.11(f)) onto which the FIB sample is glued again by Pt deposition (Fig. 2.11(g)). The exact position of the sample is shown by the arrow in Fig. 2.11(f). At the final step, final thinning and cleaning of the lamella are performed using low energy Ga^+ ions (Fig. 2.11(h)).
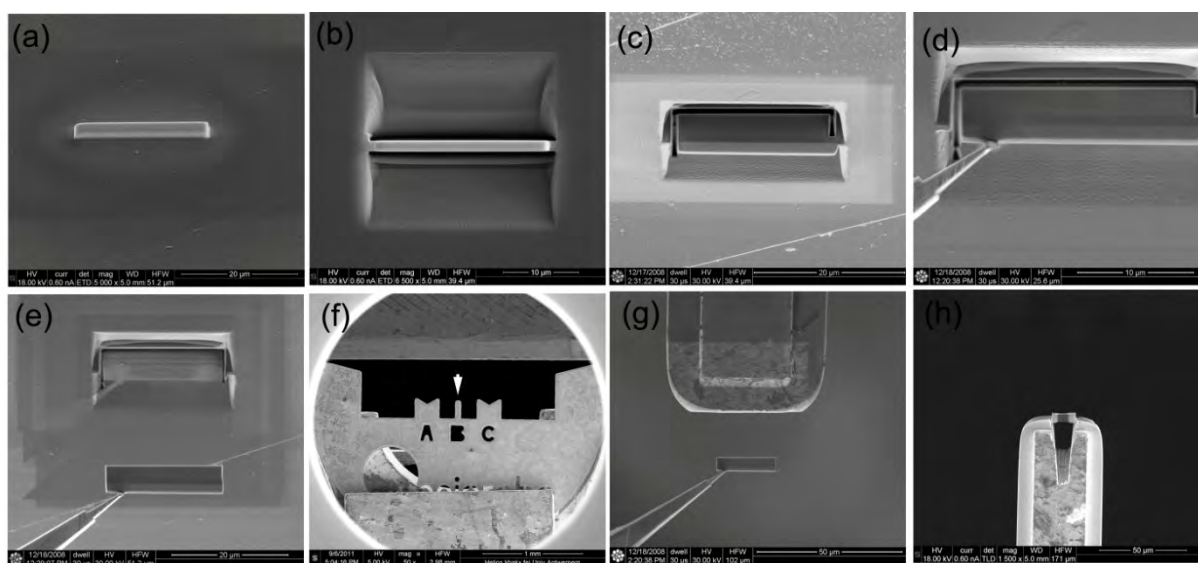
Figure 2.11 Steps of preparation of a cross-sectional TEM sample using FIB.

In this thesis, a dual beam FIB/SEM Helios NanoLab 650 (FEI) is used. This machine uses Ga^+ ions together with a FEG extreme high resolution SEM. In addition, the system is equipped with GIS containing a Pt source and an Omniprobe for micro-manipulation of the specimen. The beam energy for the ion beam is in the range of 500 eV - 30 keV and the smallest probe size is 7nm obtained at 30 kV/1.1 pA. Typically, for TEM sample preparation, ion beams of 30 kV/9 nA and 30 kV/0.23 nA with corresponding probe size of 249 nm and 38nm are used for sample cutting and early stage thinning. In order to minimize any damage on the sample, final cleaning on both sides of the thin lamellar is performed using an ion beam of 1 kV/95 pA.

Chapter 3

3. Effect of deposition rate on the microstructure of electron beam evaporated nanocrystalline Palladium thin films

3.1. Introduction

As explained in section 1.2, Pd is a promising candidate material for H_2 purification and sensing [23]. For such applications the metal surface area plays an important role regarding the optimization of the interaction between Pd and H_2. In order to obtain a higher surface to volume ratio, special attention has been paid to nanostructured forms of Pd such as nanoparticles, nanowires, nanotubes, nanocrystals and thin films. Nanowires have a high surface to volume ratio but suffer from poor mechanical stability [135]. Conversely, thin nc Pd thin films deposited on a flat substrate offer improved mechanical stability, but relatively low surface to volume ratio [23,136]. Moreover, it has been reported in the literature that nc thin metallic films often suffer from a lack of ductility which limits their use in those applications in which the ability of the materials to deform, stretch, or permanently change shape without cracking must be controlled [137-139]. Such behavior is attributed to the lack of strain hardening due to the absence of forest dislocation hardening mechanisms especially when the grain size is in the submicron range [58].

However, it was mentioned in section 1.3.5 that the introduction of growth nanotwins in nc metallic bulk samples and layers improves the strength/ductility balance [50-57]. Typically, in nc metals with HAGBs but without nanotwins the increased strength is accompanied by a loss in ductility, thermal stability, and electrical conductivity. However, nanotwinned metals such as copper exhibit very high tensile strengths, with good ductility, thermal stability, and electrical conductivity at room temperature [50, 140].

In order to amplify the formation of growth twins, most efforts for the synthesis were intentionally focused on metals with low and moderate SFE, such as Cu [51,52] and stainless steels [55-57]. However, although the technological needs for other nc twinned metallic films with higher SFEs are clear, such as Pd membranes to be used for hydrogen technologies, such materials have not as yet benefited much from similar efforts.

Recently, it has been reported that the strength/ductility balance of Pd thin films deposited by e-beam evaporation with an average grain size of 30 nm can be improved due to the presence of coherent growth nanotwins [58]. The origin of this behavior is attributed to the TB/dislocation reactions, providing an isotropic hardening contribution to the strain-hardening capacity [141]. The results were also used by Colla et al. [69] for the development of a semi-analytical model based on homogenization theory in order to predict the strength and the evolution of the strain hardening capacity of the twinned Pd films. The high strain

hardening capacity of the twinned Pd films was obtained with only 20% to 30% of the grains containing nanotwins, revealing a huge potential to raise even more the strength/ductility balance of the Pd films [69]. Therefore, a series of experiments to determine the driving forces as well as the fundamental mechanisms controlling the formation of growth twins in nc Pd films has been conducted. The final goal is the optimization of the deposition parameters to produce Pd films with a well-controlled population of nanoscale twins by analogy with recent experimental results obtained on Cu [52,140]. Very recently, Wang et al. [59] have demonstrated the absence of nanoscale growth twins in sputter deposited {111} textured nc Pd films. On the contrary, an absence of clear crystallographic texture was observed in e-beam-evaporated films accompanied by the presence of nanoscale growth twins in these films, even though Pd has a high SFE [141]. Kobler et al. found similar percentages of nanotwins in sputter-deposited Pd films [142]. Based on careful HRTEM analysis of the TBs, the formation mechanism of the twins in the e-beam deposited samples was attributed to the splitting and the subsequent migration of a GB segment instead of a twinning mechanism involving the nucleation and glide of SPDs [143-146]. It was also concluded that the large misorientation between the grains in the non-textured films constitutes the driving force for the activation of the twin growth mechanism. However, several key questions remain regarding the influence of other parameters such as the effect of the deposition rate and of the internal stress. Also, the experimental methods used by Wang et al. [141] to analyse the texture-dependent twin formation did not include the investigation of the character and the type of the GBs susceptible to act as preferential sites for the nucleation of the twins.

Recently, Castrup et al. [147] studied the structural properties and residual stresses of 500 nm thick magnetron sputtered nc Pd and PdAu films on flexible polymeric substrates with changing the pressure of the sputtering gas (Ar) in the range of 0.3 to 2 Pa which results in different deposition rates changing from 0.21 to 0.12 nm/s, respectively, which constitutes a relative narrow range. X-ray diffraction (XRD) measurements show that the (111) texture decreases with increasing Ar pressure and the (220) texture becomes more dominant. The grain size also decreases from 42 to 24 nm with increasing Ar pressure. TEM results show that the columnar grain length and the grain size in Pd film are almost unchanged with 67 and 24±15 nm, respectively. Moreover, significant changes of microstructure were not observed when compared to deposition on hard substrates.

In the present work, microstructure changes of e-beam evaporated Pd thin films including grain size, texture changes, GB analysis at nanoscale etc. with changing deposition rate in a

wide range of 0.3 to 5 Å.s^{-1} are determined and discussed. The density of TBs was measured using conventional BF and DF TEM while HRTEM was used to measure the dislocation densities as well as the interaction of these dislocations with growth TBs. Furthermore, ACOM-TEM has been used to characterize the evolution of the grain size distribution, the crystallographic texture and the character of the GBs. These results provide insightful information to guide the production of microstructures with enhanced strength/ductility balance in high SFE nc metallic thin films.

3.2. Experiments and Methods

Pd films with a thickness of 310 nm were deposited [1] by e-beam evaporation with three deposition rates (0.3 Å.s^{-1}, 1 Å.s^{-1} and 5 Å.s^{-1}). The films were deposited on top of a SiO$_2$ intermediate layer lying on a Si wafer. A thin Ti adhesion layer (25 nm) separating the Pd film from the SiO$_2$ layer was used to improve the adhesion of the films. The Pd target used for the evaporation of the films is of high purity (>99.995%), and as a high vacuum (1.3× 10^{-6} Pa) is created using a cryogenic pump inside the deposition chamber, no pollution effect is expected inside the Pd films. A previous study of similar Pd films using EELS, EDS and Energy Filtering TEM did not reveal the presence of any impurities within the matrix or along the GBs [141].

Conventional TEM characterization and HRTEM analysis of the films were carried out using a TECNAI G2 (FEG, 200 kV). FIB thinning with the "lift-out" procedure was used for the preparation of cross-sectional and plan-view TEM thin foils (section 2.3.1). The grain size distribution as well as the crystallographic texture of the Pd films were investigated by ACOM-TEM using a Philips CM20 equipped with a LaB$_6$ gun at 200 kV. The ACOM-TEM experiments were performed at the ULB.

3.2.1. Geometric Phase Analysis

In order to allow an easy visualization of single dislocations, Geometric Phase Analysis (GPA) was performed. GPA is an image processing technique which is sensitive to small displacements of the lattice fringes in HRTEM images. A mask is applied in the Fourier transform of the HRTEM image centered on the periodicity of interest and highlights local

---

[1] The deposition was performed at Université catholique de Louvain (UCL) by M.-S. Colla.

variations of the interplanar distances (i.e., local **g** maps) as so-called hot-spots [148]. These maps are used to facilitate the visualization of dislocations but not for the quantification of strain fields in the microstructure.

3.3. Results and Discussion

3.3.1. Conventional TEM analysis

Figure 1 shows BF micrographs of FIB cross-sectional TEM samples. These samples have been prepared from 310 nm thick Pd films deposited by e-beam evaporation at different deposition rates of 0.3, 1 and 5 Å/s. The Pd films exhibit a morphological texture with columnar grains elongated parallel to the growth direction (bottom to top of figures). The ring shaped SAED patterns shown as insets in this figure were obtained using an aperture corresponding with 200 nm on the sample. The obtained ring patterns reveal the expected fcc Pd crystalline structure. Moreover, the appearance of a ring pattern instead of a spot pattern confirm the existence of nanosized grains in Pd films.
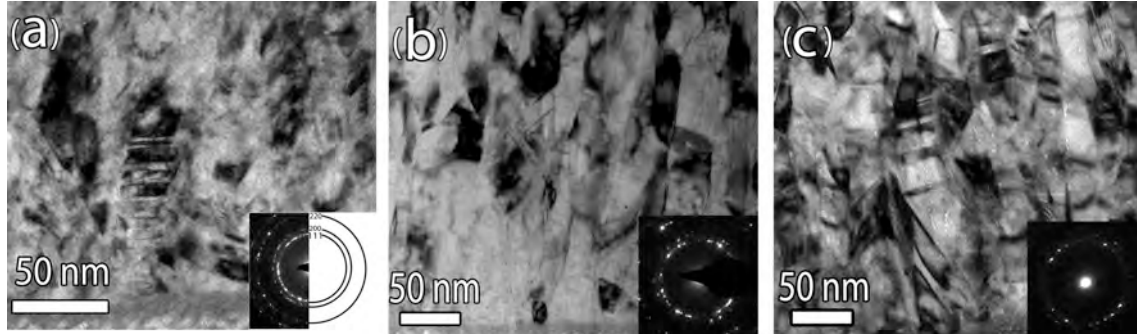
Figure 3.1 BF image and corresponding diffraction pattern of 310 nm thick Pd film deposited by e-beam evaporation technique at a) 0.3 Å/s b) 1 Å/s and c) 5 Å/s.

3.3.2. Statistical analysis of Pd films deposited at different rates

A statistical analysis of the in-plane and out-of-plane (along the film growth direction) average grain sizes, TB density and TB spacing was carried out using BF and DF micrographs for all three films. Around 100 grains for each film were included in the analysis. In order to ensure no twins were missed the sample was tilted up to ±30° along two perpendicular directions. Subsequently, BF images were taken after each 1° tilting. HRTEM images were also used to measure the dislocation density. The latter was measured by counting extra half

planes on Inverse FFTs (IFFTs) generated from HRTEM images using masks applied on each **g-**vector. An example of the IFFT using one **g** vector is shown in Fig. 3.2 where all the extra half planes are detected by following the 1D lattice fringes. The accuracy of the dislocation density measurements was calculated by determining the allowed spread of the selected region in the HRTEM image which did not change the number of dislocations.
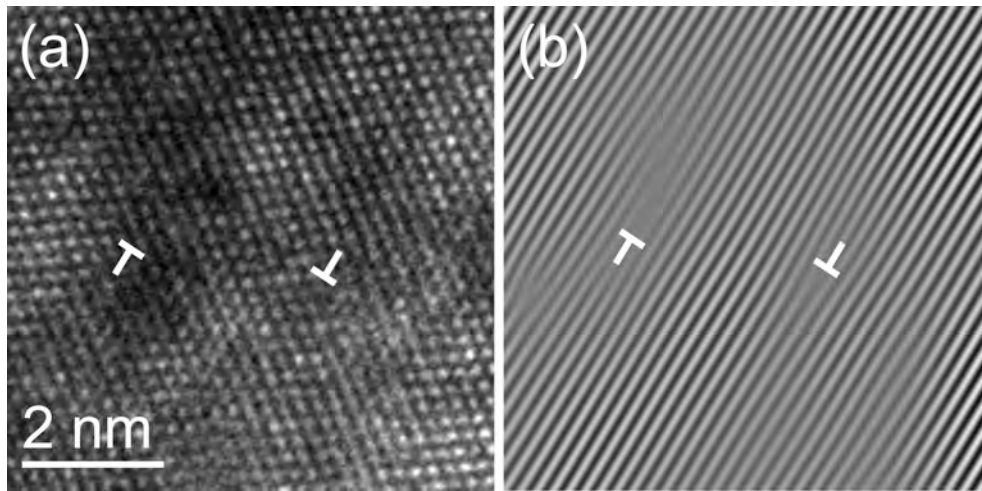
Figure 3.2 (a) HRTEM image of Pd nanograin containing lattice dislocations and (b) corresponding IFFT of (a) taken from one **g** vector showing 1D lattice fringes. The dislocations are indicated by "T" symbols.

The results are presented in Table 3.1. It is clear from the statistical measurements that the TB density and volume fraction of the grains containing twins increase with increasing deposition rate. Based on the coarsening of the spots of the 111 ring observed in the diffraction patterns of Fig. 3.1, it can be concluded that, at least qualitatively, a crystallographic {111} texture component is appearing with increasing deposition rate. On the other hand, within experimental error, the average grain size (width) and the twin spacing remain constant.

Table 3.1 Statistical measurements in nc Pd thin films at different deposition rates

Deposition rate (Å/s)	0.3	1	5
TB density (m^{-3})	$6.1\text{-}6.7\times10^{21}$	$9.4\text{-}10.3\times10^{21}$	$12\text{-}13.2\times10^{21}$
Average dislocation density (m^{-2})	$2.5\pm1.1\times10^{15}$	$2.4\pm1.3\times10^{15}$	$6.25\pm1\times10^{16}$
Grain size (width)(nm)	14-32	15-40	18-40
Grain size (height)(nm)	41-105	45-100	45-112
TB spacing (nm)	2-12	2-13	2-10
TB length (nm)	14-35	13-40	10-50
Grains containing TB (%)	25-30	35-40	50-54
Grains containing more than 2 TBs[*] (%)	4	10	20

Moreover, a clear increase of the dislocation density can be observed for the highest deposition rate (5 Å.s^{-1}). This can be attributed to the increase of internal stress upon deposition. Indeed, the internal stress measured using the Stoney method [149] in the films deposited at 1 Å.s^{-1} was equal to 300 MPa and jumps to 600 MPa for the films deposited at 5 Å.s^{-1} which is higher than the macroscopic yield stress measured by Colla et al. [69] on the same films (450±39 MPa). Based on these results of Colla et al. [69] it can thus be expected that dislocation activity will develop in the majority of the grains of the films deposited at 5 Å.s^{-1} (the equivalent plastic strain corresponding to a yield strength of 600 MPa is about 0.5%) while only few dislocations will nucleate in the films deposited at 1 Å.s^{-1} at places where the local stress stored within some grains becomes higher than the resolved shear stress required to activate the dislocation sources (and which depends on the local orientation of individual grains).

3.3.3. HRTEM investigations

In order to study the effect of the deposition rate on the coherency of growth nanotwins in Pd films, HRTEM images were taken from different regions of the sample. It can be seen that for the lowest deposition rates (0.3 and 1 Å/s) most of the TBs are fully coherent without any residual dislocations, as shown in the HRTEM image of Fig. 3.3(a). However, for the highest deposition rate (5 Å/s), the coherency of the TBs decreased significantly as shown in Fig. 3.3(b). In this figure, it can indeed be clearly seen that the atomic structure of the TBs is highly distorted.

Idrissi et al. [58] have shown that this lack of coherency can be due to the presence of a high density of Frank sessile dislocations located at the TB/matrix interfaces, with a Burgers vector pointing out of the twinning plane [58]. The presence of Frank dislocations at the TBs was attributed to the interaction of lattice dislocations with CTBs. Dark regions related to the strain field induced by some of these dislocations are indicated by white arrows in Fig. 3.3(b). Local **g**-mapping was performed on the Pd films deposited at the lowest and highest deposition rate to reveal the interplanar spacing variations as well as the exact position of the dislocations in the HRTEM images. The local **g**-maps in Fig. 3.3 (c) and (d) show the positions of the dislocations as hot-spots related to the high strain fields in the zone delimited by dashed lines in Fig. 3.3 (a) and (b), respectively. Comparison of these maps shows that the dislocation density in the film deposited at highest deposition rate (5 Å/s) is much higher than the film deposited at lowest deposition rate (0.3 Å/s) which is compatible with the measured dislocation density using inverse FFT from the original HRTEM images (Table 3.1).
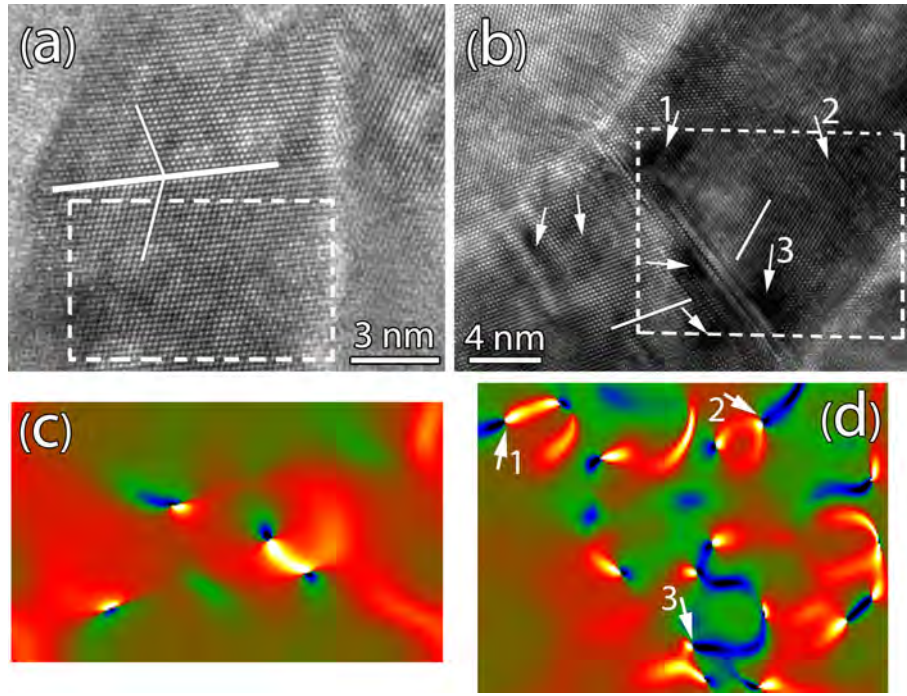
Figure 3.3 (a) HRTEM image showing a typical TB structure in Pd films deposited at 0.3 Å/s. Note the perfect coherency of the TB and the lack of dislocation contrast. Similar behavior was observed in films deposited at 1 Å/s [59]. (b) TB lost the coherency in films deposited at 5 Å/s. (c) and (d) local g maps from the zone indicated by dash lines at figure 3a and 3b, respectively.

Considering the (111) plane as a twin plane and $(1\overline{1}\overline{1})$ as the glide plane for lattice dislocations, initially, an extended perfect dislocation (a/2[101]) is dissociated into two SPDs bounding a SF ($\frac{a}{6}[1\overline{1}2]$ and $\frac{a}{6}[112]$). When this extended dislocation meets the TB, the two SPDs recombine at the $(1\overline{1}\overline{1})$ plane and form a perfect dislocation, a process which does not require a high stress due to the high SFE of Pd [58,150]. Then, the full dislocation dissociates into a sessile Frank partial dislocation and a new SPD in the twin plane. The reaction can be written as:

$$\frac{a}{2}[101]_{(1\overline{1}\overline{1})} \rightarrow \frac{a}{3}[1\overline{1}1]_{sessile} + \frac{a}{6}[121]_{(1\overline{1}1)} \tag{3.1}$$

Nanoscale CTBs can accommodate few amount of lattice dislocations. The strong loss of the coherency of these boundariesin the films produced at the highest deposition rate (5 Å/s) is thus in agreement with the increase of the lattice dislocation density in these films (see Table 3.1).

3.3.4. ACOM-TEM analysis of Pd films versus deposition rates

Figure 3.4 shows the ACOM-TEM results including orientation maps, grain size distribution and crystallographic texture of plan-view FIB samples of Pd films deposited at different deposition rates. The ACOM-TEM orientation maps are 250×250 pixels in size and were obtained using a step size of 4 nm with an acquisition frequency around 70 frames per second. In order to avoid ambiguities for the measurement of the grain size distribution, all coincidence site lattice (CSL) boundaries such as $\sum 3$ TBs were excluded from the measurements shown in Fig. 3.4. The grain size distribution is relatively narrow with the average grain size equaling to 23.7±0.5 nm, 34.4±0.4 nm, and 32.5±0.4 nm for Pd thin films deposited at 0.3 Å/s, 1 Å/s and 5 Å/s, respectively. These values fall within the ranges observed by conventional TEM (Table 3.1). These statistical results of the ACOM-TEM technique indicate that there is a true increase of the grain size with increase of deposition rate from 0.3 to 1 Å/s, whereas for 5 Å/s, the grain size does not change much compared to 1 Å/s. Castrup et al. [147] also reported that with decreasing the sputter deposition rate from 2.1 to 1.2 Å/s, the grain size of a Pd film decreases from 42 to 24 nm, which confirms our results.
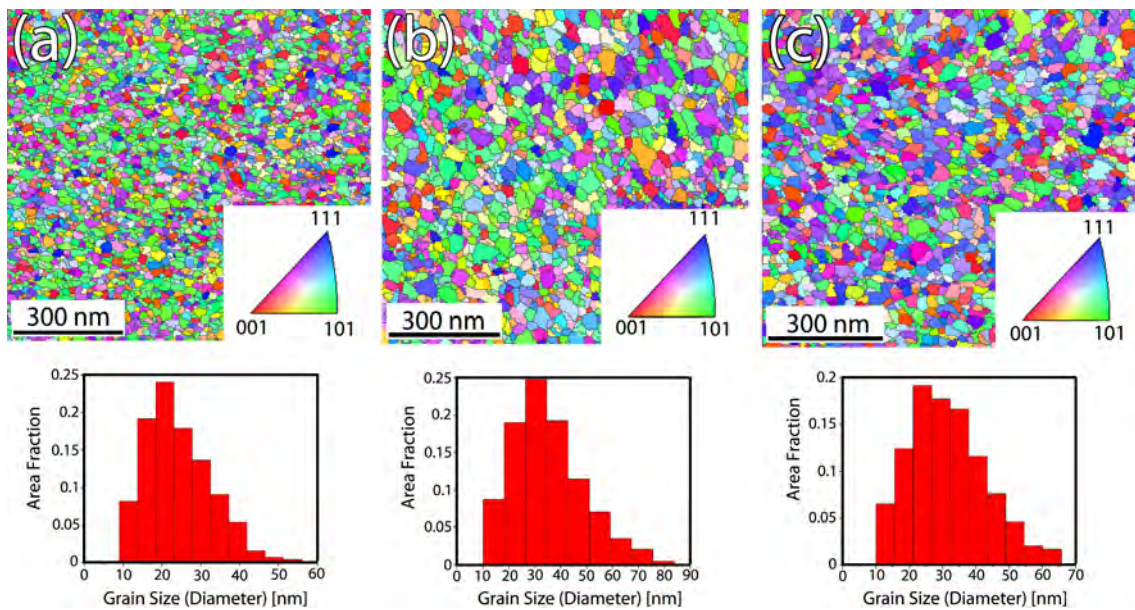
Figure 3.4 ACOM-TEM orientation mapping, crystallographic texture and grain size distribution of plan-view FIB samples of Pd thin films deposited at various rates of a) 0.3 Å/s b) 1 Å/s and c) 5 Å/s.

The crystallographic texture of Pd films deposited at different rates is displayed in Fig. 3.5. The results show that the Pd film deposited at the lowest deposition rate of 0.3 Å/s has a

strong {101} texture component, which decreases with increasing deposition rate. This is also consistent with the X-ray diffraction (XRD) measurements done by Castrup et al. [147] where they reported that the Pd film sputtered at the highest rate has a strong (111) texture, the extent of (111) texture decreases with decreasing the sputtering rate and the (220) texture becomes more dominant. It has already been confirmed that the absence of crystallographic texture in e-beam evaporated films allows the formation of nanoscale growth twins via GB migration [59]. Therefore, with increase of deposition rate, the possibility of formation of growth twins increases, resulting in a higher twin density. This assumption is in good agreement with the results extracted from BF and DF images (Table 3.1). The obtained ∑3{111} TB density (μm^{-3}) is 6100±600, 9350±900 and 12000±1200 μm^{-3} for the 0.3, 1 and 5 Å/s deposition rates, respectively. The {111} crystallographic texture analysis is shown in Fig. 3.5 from which this component is seen to become sharper with increasing deposition rate. However, a detailed analysis of the pole figures shows that a full {111} fiber texture has not been formed yet and that the {101} texture is still dominant.

Figure 3.5 {101} and {111} pole figures of plan-view FIB samples for Pd thin films deposited at various rates of a) 0.3 Å/s b) 1 Å/s and c) 5 Å/s.

An analysis of the GB character of the plan-view Pd films was performed using ACOM-TEM including grains with sizes as small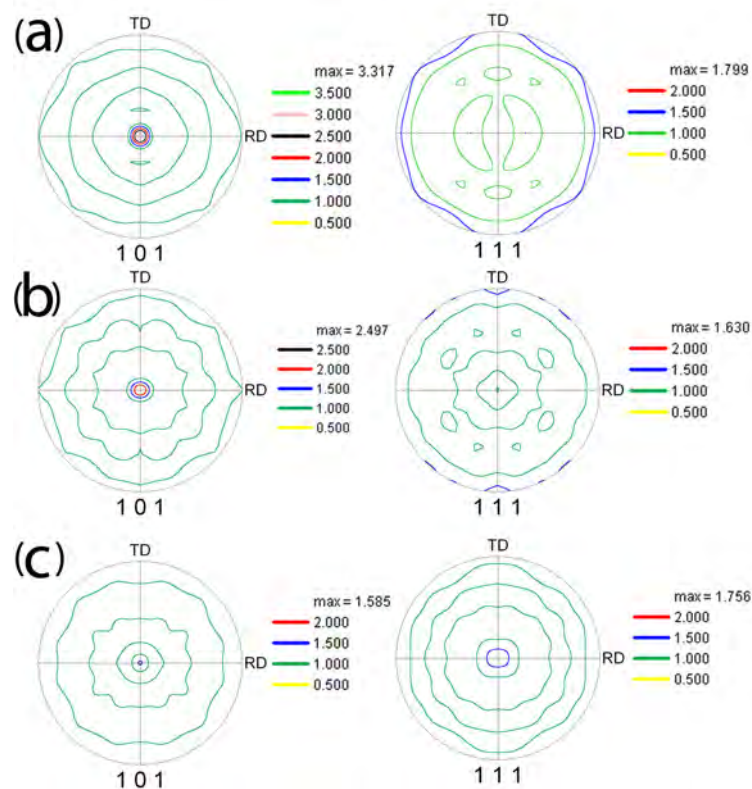 as 10 nm. The $\sum 3\{111\}$ TBs were excluded from the measurements in order to exclude counts of these types of interfaces from the measurements of the GB character. These results allow relating texture and microstructure changes with different deposition rates. Besides, the type of GB can also play a role in the formation mechanism of twins during the deposition. The GB character mapping of the Pd film deposited at 1 Å/s is shown in Fig. 3.6. The GBs are divided into LAGBs and HAGBs. A LAGB is a GB with a misorientation angle of lower than 15 and HAGBs have a misorientation angle higher than 15°. During atomic deposition of Pd films, it can be expected that the formation of twins is favored from HAGBs (excluding the $\Sigma 3$ types) which involve higher driving forces for the formation of twins. Although both LA- and HAGBs are detected in the Pd films obtained with different deposition rates, the fraction of different types of HAGBs plays an important role to understand the differences among the microstructures. The statistical measurements show that the fraction of HAGBs in the range of 55-65° is 19%, 22% and 25% for Pd thin films deposited at the various rates of 0.3 Å/s, 1 Å/s and 5 Å/s, respectively. On the other hand, the fractions of HAGBs in the range of 15-55° are almost independent of deposition rate.

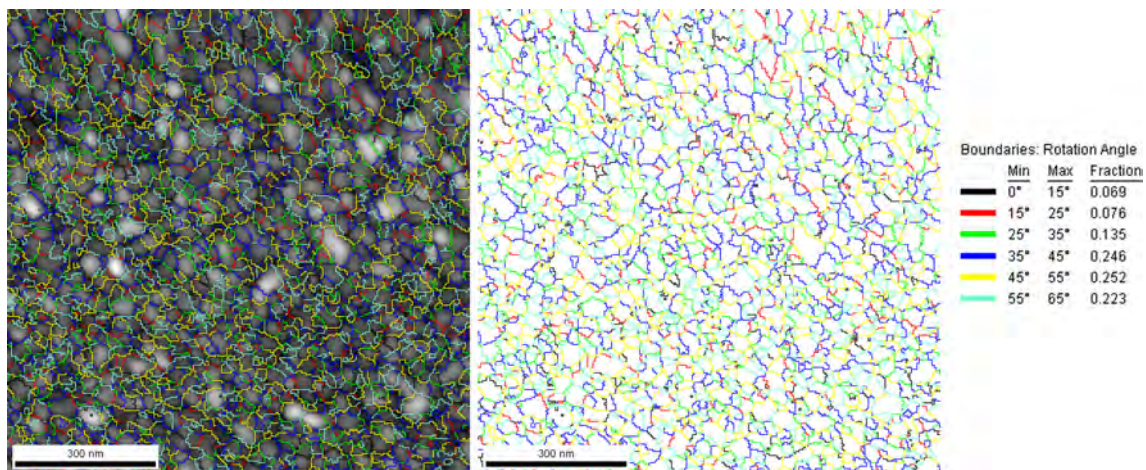| Boundaries: Rotation Angle		
Min	Max	Fraction
0°	15°	0.069
15°	25°	0.076
25°	35°	0.135
35°	45°	0.246
45°	55°	0.252
55°	65°	0.223

Figure 3.6 An example of the analysis of GB character using ACOM-TEM mapping. The table shows the fraction of different types of GBs.

In other words, the higher fraction of HAGBs in the range of 55-65° points towards a higher potential for formation of growth twins. Also, increasing the fraction of this family of HAGBs

with increasing deposition rate may explain the decrease of the {101} texture in the films produced at the highest deposition rate due to the increase of the angles between the 101 directions in neighboring grains.

Finally, based on these results, it can be concluded that the GB character and texture of thin Pd films can be controlled by optimizing the deposition conditions. Consequently, the TB density and coherency of TBs can be controlled by optimizing the GB character or texture through the selection of the deposition rate.

3.4. Conclusions

The effect of deposition rate on the microstructure changes of thin Pd films deposited by e-beam evaporation has been investigated by various TEM methods. The TEM results and statistics given here (crystallographic texture, grain size distribution, dislocation and twin density, etc.) will be useful for the analysis and understanding of the mechanical behavior of the Pd films produced with different deposition rates.

- All films reveal a columnar nanograin configuration containing nanoscale growth twins. TB density and volume fraction of grains containing twins increase with increasing deposition rate. A clear increase of the dislocation density was also observed for the highest deposition rate (5 Å.s^{-1}) which is related to larger internal stress at high deposition rates (5 Å/s).

- A {111} crystallographic texture component is appearing while the dominant {101} crystallographic texture is decreasing with increasing deposition rate. The latter is coupled with the increase of TB density. Also, a moderate increase of the mean grain size with increase of deposition rate is found.

- It was shown that, for the lowest deposition rates (0.3 and 1 Å/s), most of the TBs are fully coherent without any residual dislocations. For the highest deposition rate (5 Å/s), the coherency of the TBs decreased significantly due to dislocation/TB interactions. This result corresponds with the increase of the lattice dislocation density in the films with higher deposition rate. The fraction of HAGBs in the range of 55-65°continuously increases with increasing deposition rate, which again correlates with the increasing TB density.

Chapter 4

4. The study of time resolved creep/relaxation tests in nanocrystalline Pd thin films by using on-chip HRTEM testing

4.1. Introduction

Nc metals involve excellent mechanical performances in terms of strength and fatigue resistance but often at the expense of ductility [151]. Furthermore, nc systems show moderate to high rate sensitivity at room temperature [152] which might help restoring the ductility but can lead to detrimental creep/relaxation effects in applications. The time dependent creep/relaxation behaviour in nc materials is amplified more in comparison with micro-sized materials. This behaviour is due to the change in deformation mechanisms from dislocation mediated plasticity such as forest hardening, to more thermally activated processes such as GB mediated processes. These mechanisms include the nucleation of dislocations at GB ledges, diffusion along GB, grain growth, and GB sliding [153]. Thin metallic films constitute ideal candidates for looking at the mechanics of nc systems using TEM as they can be processed easily with nanograined structures often involving one grain over the thickness as well as sharp textures [154]. The small thickness allows for direct in-situ testing in TEM for analysis of the deformation mechanisms [109,155]. In addition of being adequate for fundamental investigations, thin nc metallic films are of direct interest in microelectronics, Microelectromechanical systems (MEMS), functional coatings or membrane applications. In the present chapter, the focus is on an extended time-resolved creep experiment including several TEM sessions on a single sample and spread over more than one month.

Different methods have been used to characterize creep or relaxation behaviour at the nanoscale, e.g. nanoindentation [156], strain rate jump tests [157, 158] or direct tensile testing [159]. The main drawbacks of these methods involve the difficulty to impose very small strain rates typical of real applications and to perform in-situ relaxation tests in order to characterize the underlying mechanisms. Also, the sensitivity to drift is increased at the nanoscale, which prevents imposing a constant load during long periods of time. Another technique consisting in stress evolution measurement during thermal cycling and allowing in-situ observation has been proposed in the literature but the interpretation of the results and high resolution observation are more complicated [160]. Here, we used for the first time time-resolved HRTEM relaxation experiments using an on-chip tensile testing method [161,162] which will be explained in more details in the following section.

4.2. Materials and methods

4.2.1. On-chip nanomechanical testing method

The original concept of the on-chip nanomechanical testing is to use the internal stresses (or equivalently the mismatch strain) present in a patterned thin Si_3N_4 layer (called 'actuator') which is 30 nm thick and which deforms the sample layer, here 90 nm thick Pd beams deposited by e-beam deposition [161], see Fig. 4.1(a). Both the actuator and the specimen lie on a 1µm thick amorphous SiO_2 sacrificial layer, deposited on a Si substrate. The actuator material is selected in order to yield large internal stresses created during the deposition process. The geometry of the actuator is defined by a first lithography step. The test specimen is deposited on top of the sacrificial and actuator layers, and patterned by a second lithography step. This elementary tensile testing machine is released by etching the sacrificial layer (Fig. 4.1(b)), the actuator pulling then on the test specimen. In the case of uniaxial tension, the stress σ and mechanical strain ε^{mech} in the specimen can be directly inferred from the displacement u as measured between a moving and a fixed cursor. One specimen, i.e. one beam plus its actuator, gives one point of the stress-strain curve. Different strains can be imposed by changing the geometrical dimensions of the actuator and/or of the test specimen, allowing the determination of a full stress strain curve. As a consequence, the design includes a series of test structures with varying dimensions. For further information regarding the measurement of stress and strain using on-chip nanomechanical testing see ref. [58,162].
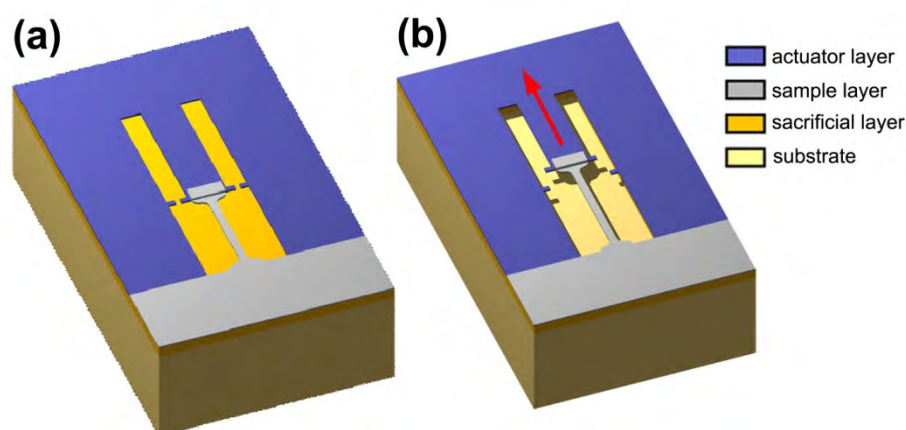

Figure 4.1 Elementary internal stress actuated tensile test structure, (a) before release, (b) after release.

In order to examine the microstructure changes by plan-view TEM during creep/relaxation tests, the Si substrate has to be removed to obtain electron transparency of the region of interest in the Pd sample. The Si substrate is selectively etched from the back face of the wafer using deep reactive ion etching (DRIE) to open windows under the structures of interest. The SiO₂ sacrificial layer is not etched during this process. The sacrificial layer is finally etched leading to the actuator contraction and deformation of the Pd beams on top of the open windows. These windows enable direct in-plane TEM observation for some selected Pd beams. The creep relaxation experiment is performed by measuring the displacement of the specimens at different time intervals. Note that both the stress and the strain vary during relaxation experiments. Figure 4.2(a) shows the schematic illustration of the on-chip tensile testing configuration which can be fitted into the TEM holder for in-situ observation.

4.2.2. FIB preparation and characterization by TEM

In order to concentrate the deformation in one region to facilitate local HRTEM and ACOM-TEM observations, notches have been milled every two Pd beams using FIB operating at 30 kV/7pA (Fig. 4.2(b)). It is worth mentioning that, most of the in-situ HRTEM investigations (i.e., dislocation density and TBs thickness measurements) were performed very close to the edge of the notches. Indeed, because of the FIB milling, the thickness of these edges was smaller than that in the rest of the Pd beam (~90 nm) where the samples are too thick for proper HRTEM imaging. Moreover, the HRTEM observations were made in the notched area of the beams to ensure to observe a plastically deforming or relaxing zone and to provide landmarks for the follow-up of exactly the same well-oriented grains during each session.

Conventional TEM and HRTEM have been used to characterize the evolution of the microstructure of the nc Pd thin films with time, in order to uncover the mechanism(s) controlling the creep/relaxation behaviour of these films. Conventional BF and DF characterizations and HRTEM were performed in a TECNAI G2 microscope operating at 200 kV. HRTEM was used to follow the microstructure changes with time. BF and DF techniques were performed to obtain morphological characterization of grains (columnar grains in this case) and grain size measurement (grain width and height) especially in as deposited Pd film.

The successive observations have been carried out carefully in nearly identical orientation and imaging conditions. Tilting the samples was thus intentionally avoided to facilitate the repeatability of the observations in similar orientation conditions. FFT patterns were recorded

68

and their symmetry was analysed and compared. By consequent, the dislocation density as well as the TBs thickness measurements do not suffer from misorientation artefacts. Furthermore, the edges of the notches often contain FIB induced amorphous domains that can be used as references for the acquisition of HRTEM images in similar defocus conditions. The unusual term "TBs thickness" refers here to the distance separating the two positions of the last non-distorted twinning planes in the matrix or in the twin grain (for further information see section 4.3.3.2).
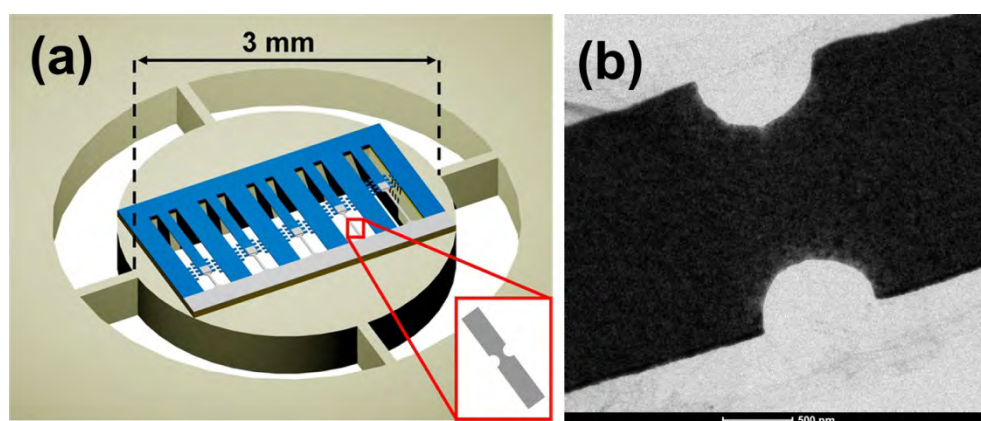
Figure 4.2 (a) Schematic view of the on-chip tensile testing method allowing in-situ TEM observation. Notches have been milled at every two beams using FIB. (b) Low magnification BF TEM micrograph of a Pd beam with notches prepared by FIB.

4.3. Results and discussion

4.3.1. Characterization of the as-deposited Pd film

Figure 4.3 shows the microstructure and texture of the as-deposited Pd films evaporated at 1 Å/s and which were investigated in both cross-sectional and plan-view thin foils prepared by FIB. The film has been thinned to ensure that there is only one grain through the thickness of the sample. Figure 4.3(a) represents the orientation mapping of the plan-view Pd film. The corresponding inverse pole figures in the direction perpendicular and parallel to the film surface are shown in Fig. 4.3 (b) and (c), respectively. A fibre texture is observed with the [110] direction oriented along the normal to the film. No preferential orientation was observed in the tensile direction (parallel to the film surface). The grain size distribution of the as-deposited Pd film is displayed in Fig. 4.3 (d). The average in-plane diameter of grains equals ~30 nm. The BF image of the cross-section FIB sample shows that the structure is columnar

with 2 or 3 grains over the thickness (Fig. 4.3 (e)). Investigation of BF and HRTEM images of the as-deposited film show that the microstructure contains $\Sigma 3\{111\}$ coherent growth nanotwins in ~ 25% of the grains as reported earlier [58,69,141]. Figure 4.3(f) shows a $\Sigma 3\{111\}$ growth nanotwin with perfectly coherent TBs. The average dislocation density of the as-deposited film measured using HRTEM images in four nanograins is $4\pm0.7\times10^{16}$ m^{-2}.
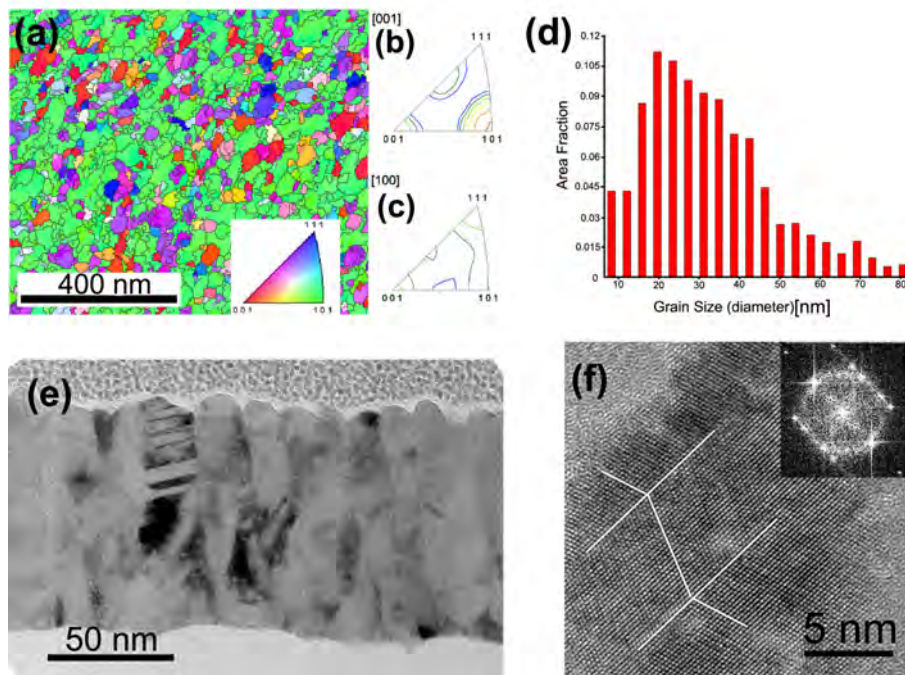
Figure 4.3 Various TEM results from the as-deposited Pd thin film: (a) ACOM-TEM orientation mapping of a plan-view FIB sample. (b) Inverse pole figure showing the {110} preferential orientation of the grains in the direction perpendicular to the film. (c) Inverse pole figure showing the random orientation of the grains in the direction parallel to the film, e.g., in the tensile direction. (d) Grain size distribution of the plan-view sample. (e) BF micrograph obtained on a cross-sectional FIB sample showing 2 or 3 grains along the thickness of the film. (f) HRTEM image showing a $\Sigma 3\{111\}$ growth nanotwin with perfectly coherent TBs.

The method for counting the dislocations is based on a number of [110] HRTEM images of selected regions taken at different defocus. From these 2D HRTEM images IFFT images with $\mathbf{g} = \bar{1}11$, $\mathbf{g}=1\bar{1}1$ and $\mathbf{g}=002$ are produced from which sites with edge dislocations can be recognized as ending fringes by following the 1D lattice fringes at a grazing incidence. An example of this is shown in Fig. 4.4 where all such clear sites are indicated by the dislocation

"T" symbol (except for those in a lower horizontal strip of the image since this region becomes covered by the labelling). However, due to the effects of the changes of defocus and image delocalisation on the actual observed configuration of lattice fringes, not all dislocations are recognized as such in every HRTEM image. In other words, one needs to look at a series of HRTEM images from a given region but obtained at different defocus to get a complete picture of the dislocations present. Furthermore, the precision of dislocation density measurement was calculated by enlarging or shrinking the selected region in a given HRTEM image as long as the number of dislocations does not change (the estimated uncertainty from counting too few (not observed) or too many (double counting) dislocations is found to be much lower). Since strong local variations in dislocation density are always possible, the averaged data presented below are obtained from several grains for each time step in the experiment. On one occasion, a particular region could be reinvestigated at several time steps.
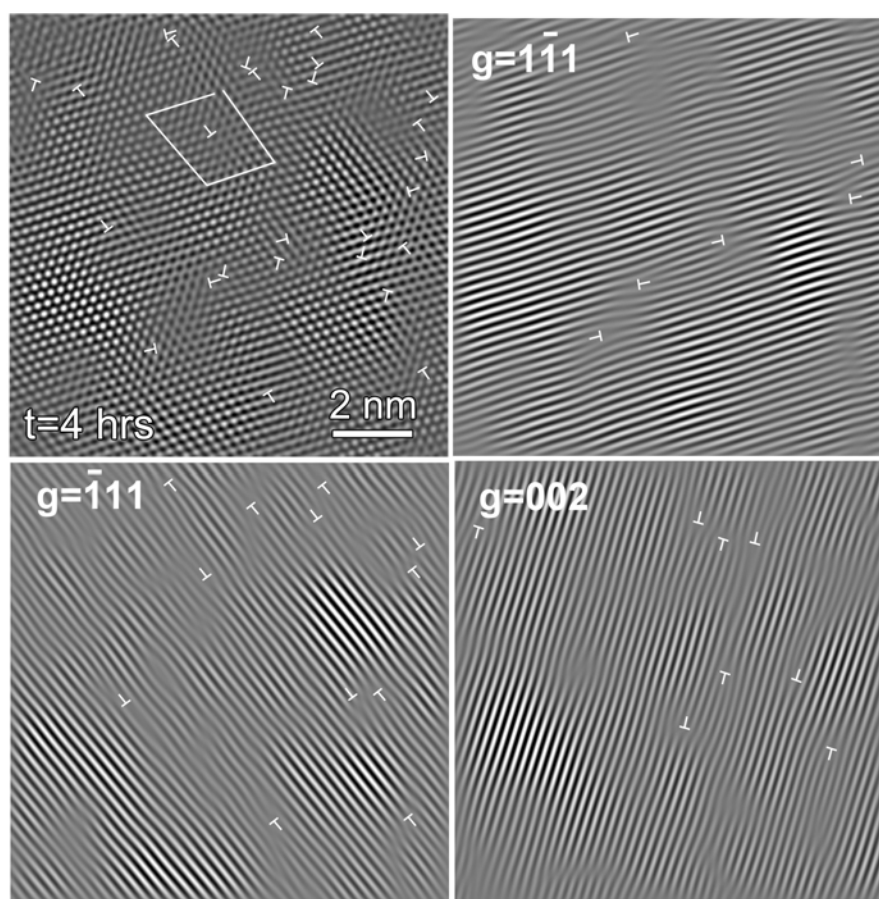
Figure 4.4 Determination of dislocation sites in a single HRTEM image via ending fringes in three IFFT images.

4.3.2. Evolution of stress and strain versus time for nc Pd films

The stress and strain evolution during relaxation has been recorded by M.-S. Colla (IMAP/UCL) from straight beams with a perfectly uniaxial stress state, see Fig. 4.5. As explained above, the four points belonging to a given relaxation time originate from beams with different length scales w.r.t. their corresponding actuator. The behaviour of these selected beams is followed for a period up to 38 days during which the relaxation behaviour was observed by decreasing the applied stress with time. The fracture strain of the 90 nm thick films is around 3% and the yield stress ∼ 500 ± 60 MPa (which is close to the internal stress value measured after deposition), both values being strongly dependent on the thickness of the thin films [58].
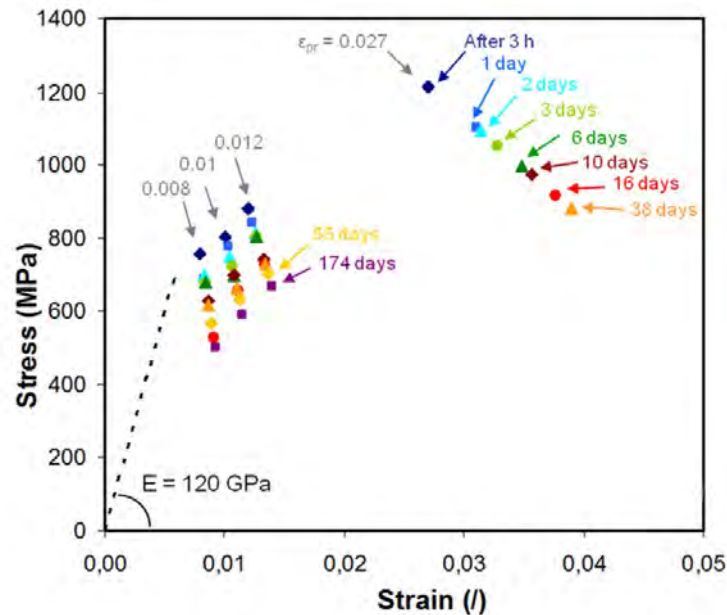
Figure 4.5 Stress-strain evolution of different Pd beams under uniaxial tension versus time. The linear elastic regime has been measured by nanoindentation as equal to 120 GPa. The initial strain level ε_{pr} before relaxation has been indicated on the figure [163].

4.3.3. HRTEM investigation of Pd films during creep/relaxation

After release of Pd beams, the specimens are transferred inside a TEM. Both time-resolved HRTEM and time-resolved ACOM-TEM methods were used to investigate the plasticity mechanisms activated at the nanoscale.

4.3.3.1. Evolution of dislocation density

The first TEM observation has been performed 4 hours after the release and has led to a second dislocation density measurement (the first being made on the as-deposited specimen, see above). The dislocation density increases up to $7\pm0.7\times10^{16}$ m^{-2} which is almost twice the initial density found in the as-deposited film, see Fig. 4.6(a). This dislocation density is more than one order of magnitude larger than the usually reported dislocation density of nc materials under deformation [163-166]. This change of dislocation density after deformation is unusual in nc metals in which it is usually claimed that the small grain size prevents any dislocation storage even though some recent investigations also found significant dislocation accumulation in nc Ni [166] and in nc Pt [165]. The presence of pre-existing dislocations and twins presumably favours additional storage. As soon as one defect gets blocked in the grain, pinning mechanisms can start acting, leading to dislocation accumulation. Only perfect dislocations were observed with no SFs or deformation twins appearing during deformation, in agreement with the high SFE of Pd ($\gamma_{sf} \approx 180$ mJ/m^2 [167]). For Pd, the critical grain size under which partial dislocations emission is favoured over full dislocations emission is around 13 nm [47,168], which implies that in the present case with average grain size of $\approx$30 nm, the SFs and partial dislocations are not expected.
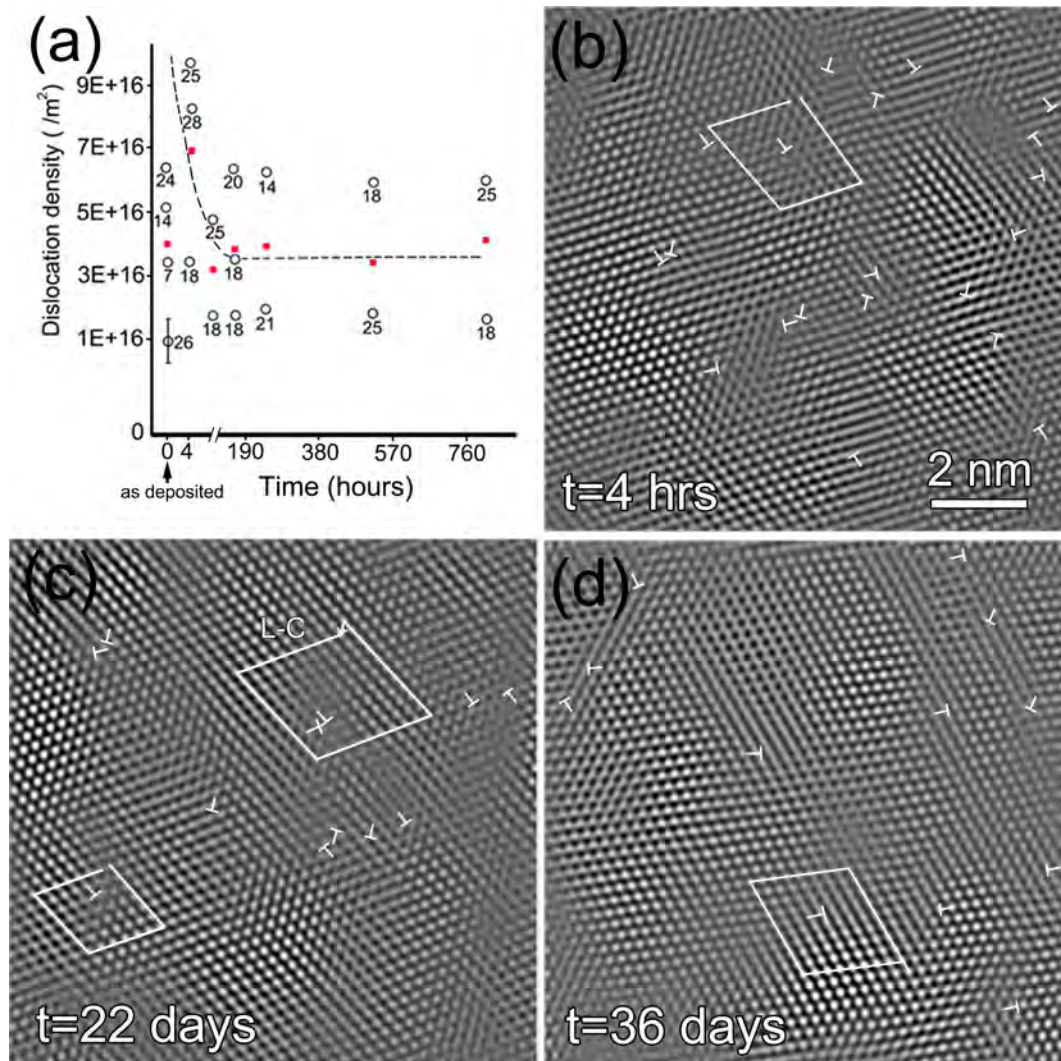
Figure 4.6 Dislocation density evolution upon relaxation as observed: (a) average dislocation density (red solid squares) evolution of the Pd film versus time (open circles are measurements of individual grains with listed numbers indicating the corresponding grain size (nm)). Dislocation density first increases when deformation is applied and then decreases upon relaxation. (b) to (d) Filtered HRTEM images showing the continuous change of the dislocation positions with time in exactly the same position of one selected grain. Note the formation and destruction of Lomer-Cottrell dislocations indicated by L-C in (c). The perfect dislocations are indicated by "T" symbols.

During relaxation, the dislocation density decreases by a factor ~2 and reaches a steady-state regime, see Fig. 4.6(a). On Fig. 4.6(b) to (d), the IFFT images extracted from HRTEM images taken after different time intervals after release (4 hrs, 22 days, 36 days) highlight the dislocation activity during relaxation. The images represent the microstructure evolution of exactly the same region over time. The positions of perfect dislocations lying in two different {111} slip planes are continuously varying. These dislocations are shown by "T" symbols in

Fig. 4.6. Interestingly, Lomer-Cottrell (L-C) dislocations have been detected. This kind of sessile dislocation is the most effective to induce hardening and is believed to be typical of fcc metals with medium to high SFE, like Pd [163]. More surprisingly, the L-C locks which normally yields a strong obstacle for moving dislocations to disappear with time, see Fig. 4.6(b) to (d). Recently, a similar formation and breaking of L-C junctions has been observed in Pt thin films with an average grain size of 10 nm [165]. Some simulation works in the literature predict that a stress of ~ 750 MPa or equivalently a strain of 2% is needed to destroy the junction in Pd [47], which falls in the range attained in the present study. Hence, despite the very small grain size, dislocation based-mechanisms clearly dictate the mechanical response of the Pd films.

Figure 4.7 shows a schematic illustration of the formation and destruction process of the L-C lock under applied stress. First, dislocations nucleate from GBs and/or of intragranular sources. When two perfect dislocations with Burgers vectors BC and CD lying respectively in the ABC and ACD slip planes glide and intersect under the applied stress, a L-C sessile junction may form following the reaction: BC+CD →BD.
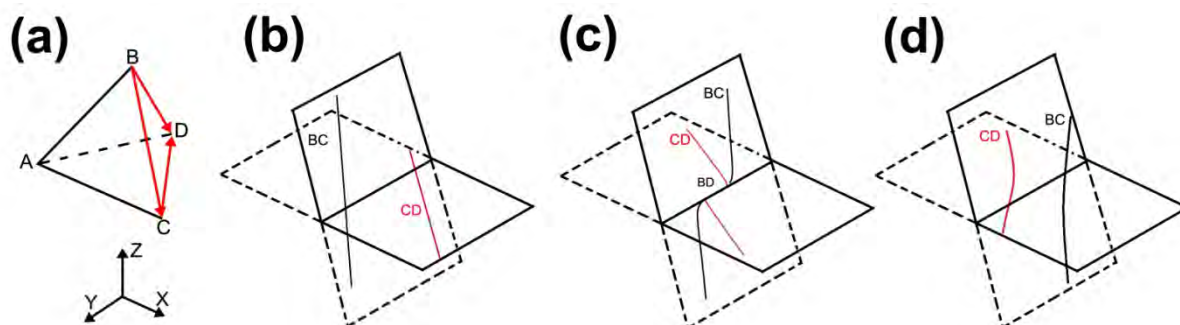
Figure 4.7 (a) Thompson tetrahedron showing the Burgers vectors of the interacting dislocations. (b),(c) Formation of L-C lock BD due to the interaction of two perfect dislocations BC and CD. (d) Destruction of the L-C dislocation at high stress.

The resulting Burgers vector BD is not contained in the two initial glide planes. Therefore, the L-C dislocation is of sessile type and could act as a strong barrier for glissile dislocations increasing the strain hardening capacity. However, these locks can be destroyed when a critical applied stress is reached as supported by recent MD simulations [168]. Fig. 4.7(d)

shows the unzipping of the L-C lock following the reaction: BD→ BC+CD. The length of the L-C segment decreases with increasing stress resulting in the junction breaking under high stress.

4.3.3.2. Twin boundary evolution during creep/relaxation of Pd film

Twins constitute strong barriers to dislocation motion. Initially, in the as-deposited state, most of the Σ3{111} TBs are perfectly coherent as can be seen in Fig. 4.3(f). However, this coherency is partially or totally lost during deformation due to the interaction of lattice deformation dislocations with the coherent TBs [58,141]. The evolution of TBs during creep/relaxation of the Pd films was also investigated using HRTEM. The evolution of the TBs thickness was performed on HRTEM images via the observation of the coherency of growth ∑3{111} TBs. The HRTEM images were acquired at different times (4 hrs, 3, 6, 9, 21 and 36 days) from the same regions containing these boundaries. The TBs thickness was determined using the variation of the intensity profile along the second set of {111} planes inclined relative to the twinning plane in the IFFTs. Figure 4.8 shows an example of this approach. In this figure, the position of the last non-distorted (111) twinning plane in the matrix grain is determined from the intensity profile plotted along the $(11\bar{1})$ plane in the IFFT. This position is indicated by a black arrow in Fig. 4.8(b) in which a clear drop of the intensity is observed due to a perturbation of the stacking sequence ABCABC… inducing a shift of the positions of the atoms. Such feature is attributed to a local loss of coherency of the TB due to the accumulation of dislocations at this boundary. The precision for the detection of the last non-distorted twinning plane using the IFFTs corresponds to one atomic plane (see the intensity profile of Fig. 4.8).
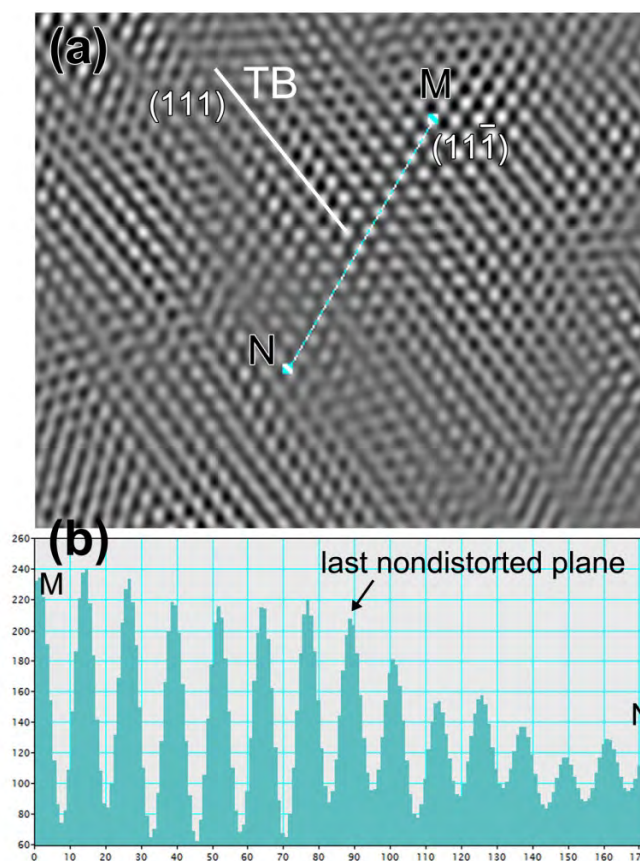
Figure 4.8 (a) IFFT of HRTEM image obtained on a Pd film relaxed for 36 days. (b) Intensity profile plotted from "M" to "N" along the $(11\bar{1})$ atomic plane in (a). The position of the last non-distorted twinning plane is indicated by a black arrow.

Figure 4.9(a-c) shows the TB thickness evolution upon relaxation. In the present study, upon relaxation, the loss of coherency of the {111} TBs keeps increasing as indicated by a progressive increase of the TB thickness until reaching a steady state, see Fig. 4.9(d). This is due to the formation of residual interfacial defects such as Frank sessile dislocations at the TBs [58,141] and/or the accumulation of lattice dislocations at these boundaries. The TBs thickness have been indicated by dashed white lines in the upper right insets of Fig. 4.9(a-c) from which the inclined {111} planes indicated by white solid lines in the same insets start to deviate from their initial position due to the accumulation of dislocations at the TBs. Because the TBs thickness may change along individual TBs, the measurements reported in the graph of Fig. 4.9(d) were performed in the same region indicated by dashed lines in Fig. 4.9(a) and shown in the upper right insets of Fig. 4.9(a-c). The calculated precision for the TB thickness ratio is ±0.3 (based on the precision of 1 atomic plane for the determination of the non-distorted plane). Furthermore, in order to ensure HRTEM observation of TBs at identical local

orientation conditions and thus to avoid artefacts during the TB thickness measurement, the intensity symmetry of the FFT patterns were accurately compared (see the FFT patterns shown in the lower right insets of Fig. 4.9(a-c)).
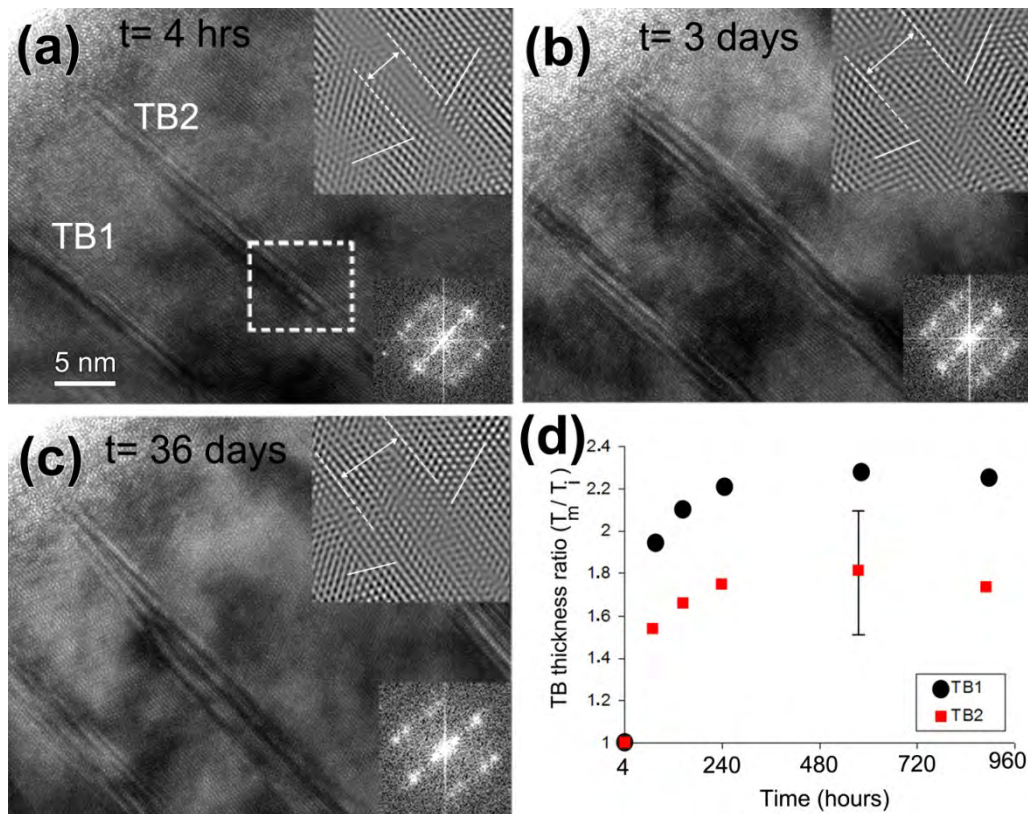
Figure 4.9 TB thickness evolution upon relaxation: (a) to (c) HRTEM images showing $\Sigma3\{111\}$ TBs at t=4 hours, 3 and 36 days, respectively. Note the increase of the TBs thickness from (a) to (b) in the filtered images at the upper right insets of the micrographs. No significant change of the TB thickness from (b) to (c) is observed. (d) Evolution of the TB thickness ratio (T measured / T initial) of the TB1 and TB2 in (a). A plateau is reached after 10 days.

The HRTEM measurement of $\{111\}$ TB thickness was performed in nanograins exhibiting different grain size and local orientation. Figure 4.10 shows the TB thickness evolution versus time including the TB1 and TB2 of Fig. 4.9. The two groups (TB1, TB2, TB3) and (TB4, TB5) were observed in two different grains. In the graph of Fig. 4.10, it can be seen that all the $\{111\}$ TBs are following the same trend with a clear increase of the TB thickness at the first stage of relaxation followed by a steady state. It is worth noting that nanograins exhibiting different local orientation will develop different amount of plastic deformation with

different numbers of activated slip systems and nature of dislocations interacting with the TBs. This could explain the variation of the TB thickness ratio in Fig. 4.10. The TB thickness may also vary in one individual nanograin as can be seen for example for TB1, TB2 and TB3. This can be explained by taking into account the position of the TBs relative to the active dislocation source in one nanograin. The TB thickness can also be used as comparitive parameter for future modeling approaches in which the numbers, types and interactions of the dislocations with the TB are investigated.
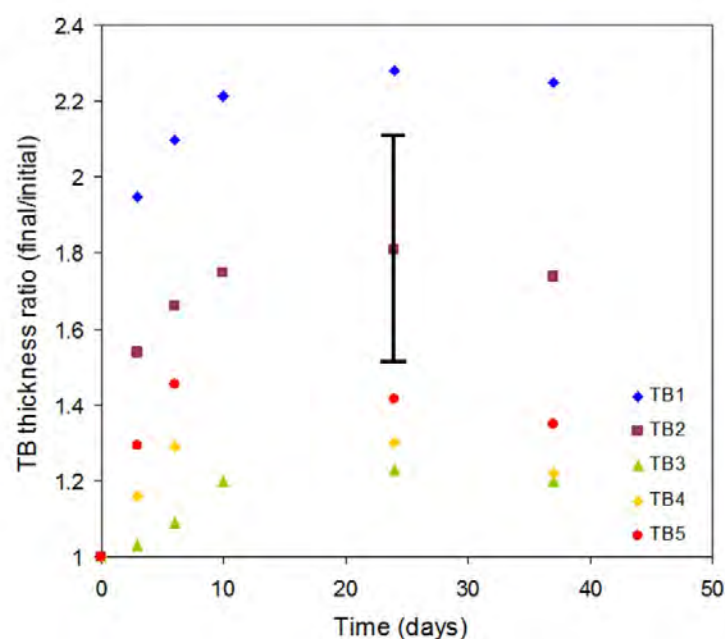
Figure 4.10 Evolution of the TBs thickness ratio with time. Similar behaviour can be seen for all the observed TBs. The error for the measurement of the TBs thickness ratio is ±0.3.

It is worth justifying that the distortions observed at the TBs shown in Fig. 4.9 cannot be attributed to a slight misalignment of these boundaries relative to the electron beam. Although the FFTs of the images in Fig. 4.9 indicate a very small misalignment, this is insufficient to account for the observed blurring. This is indeed confirmed in Fig. 4.11 showing multislice simulations of a sharp and coherent $\Sigma3\{111\}$ TB with an electron beam parallel to the <110> zone axis as well as with slight misorientations (up to 2.5°) around the <112> trace of the TB (note that such a choice of tilt axis can be expected to yield the most severe imaging effect). In this figure, it can be clearly seen that, as long as the atomic columns are resolved away

from the boundary (up to 1.5°), a sharp twin boundary remains visible, which is due to electron channeling [169]. However, for higher misorientation angles, fringe contrast dominates the matrix image and it becomes more difficult to define precisely the position of the TB. In Fig. 4.9, the atomic columns are clearly resolved on both sides of the TBs, indicating that the blurring of the image at the TB does not result from a slight misorientation of the boundaries relative to the electron beam.

| tilt 0 degree | tilt 0.3 degree | tilt 1 degree | tilt 1.5 degree | tilt 2 degree | tilt 2.5 degree |
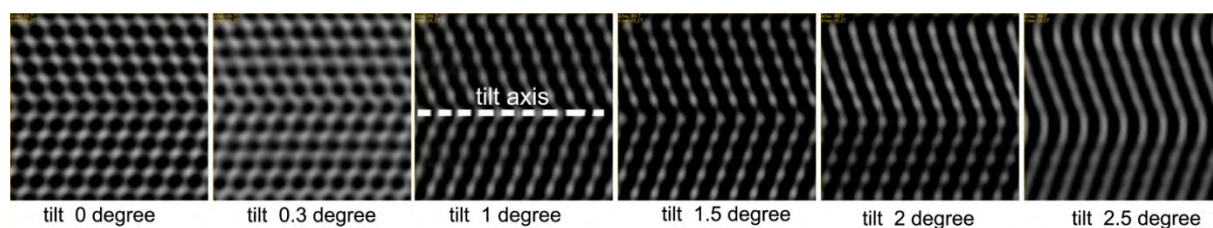
Figure 4.11 Multislice simulations of the effect of a misorientation between the electron beam and the <110> zone axis on the HRTEM contrast of $\Sigma 3\{111\}$ coherent TB. Foil thickness = 86.7 nm and defocus = 15.27 nm.

Below we have also repeated such a series but now with an inclined tilt axis more resembling the real situation observed, which is seen from the simulated diffraction patterns also presented in Fig. 4.12. It can be seen that already for these small tilts, for which the image of a sharp interface does not yield a blurred TB, one can observe a clear change in the intensity ratio between the different $002/1\bar{1}\bar{1}$ doublets (indicated by circles in one of the simulated patterns). (Note that due to the limited size of the unit cell including the twin defect, extra spots are generated, but this does not affect a general conclusion on intensity ratios). So in other words, noting a small off-zone axis deviation from the FFTs in Fig. 4.9 cannot explain the blurred image.
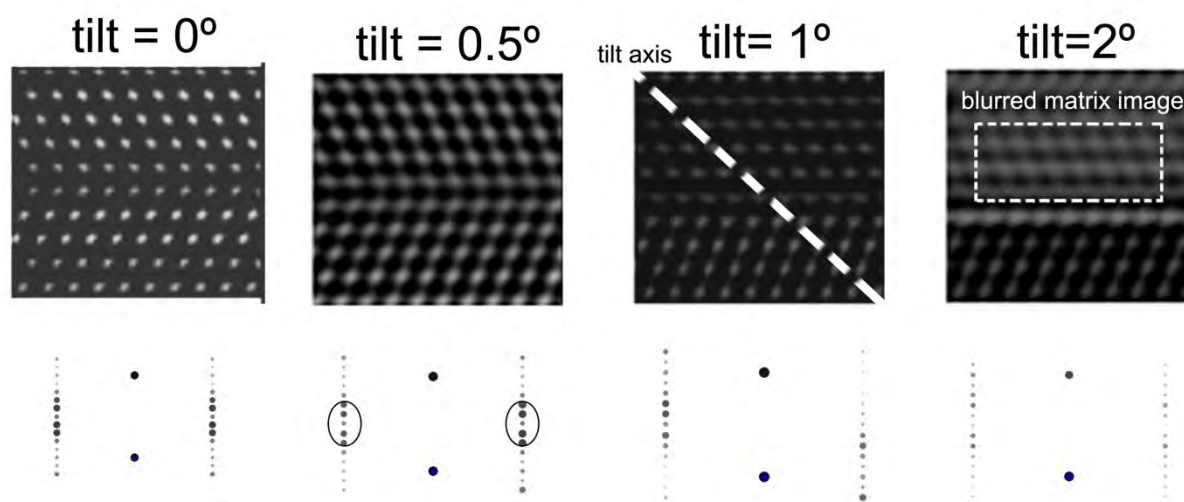
Figure 4.12 Multislice simulations of the effect of an inclined misorientation on the HRTEM contrast and corresponding diffraction patterns of $\Sigma 3\{111\}$ coherent TB. Foil thickness = 86.7 nm and defocus = 15.27 nm.

4.3.3.3. Investigation of GB mediated processes during the creep/relaxation tests

Another set of test structures was used for ACOM-TEM measurements to provide statistical data on the grain size distribution variation upon relaxation. The thickness of the beams under tensile stress coming from on-chip nanomechanical testing was not reduced using FIB. This could make the orientation indexation impossible using ACOM-TEM due to grain overlapping, however, thanks to the columnar structure, this is not the case and the extraction of the grain size distribution evolution upon relaxation was possible. Figure 4.13 presents the grain size evolution of a fixed selected region in a beam subjected to a deformation level of ~0.6 %. Based on the average grain size obtained using ACOM-TEM experiments over a period of several days, no variation in the grain size distribution is found. Under ideal circumstances, i.e. when using an identical small region, this could be attributed to the absence of grain growth during relaxation. However, due to the large area with strong variations in grain sizes and a resulting large spread of the measurements, no firm conclusions on the existence or absence of grain growth and GB migration during relaxation can be made.

The same observation for the grain size evolution is made on other beams with different initial strain levels before relaxation and average grain size did not change during relaxation. Also, no clear GB sliding has been observed by conventional time-resolved HRTEM analysis. Hence, there is some evidence that no GB type mechanisms contribute to relaxation in the

present <110> textured columnar grained specimens. These experimental observations match with the calculation of activation volume performed by UCL where no GB mediated process was predicted [163]. Obviously, this specific columnar microstructure may affect the importance of GB processes and further experimental and modeling studies are required to better understand the impact of these morphological features on the competition between the different deformation mechanisms. Some studies postulate that Coble creep is the dominating mechanism in nc materials and which occurs through the diffusion of atoms in a material along the GBs, which produces a net flow of material and a sliding of the GBs [170] however these studies involve stresses below the yield stress while in the present work the stresses are higher. Moreover, Coble creep and GB sliding are strongly influenced by the grain size and are not expected at grain size of ~30 nm [171, 172].
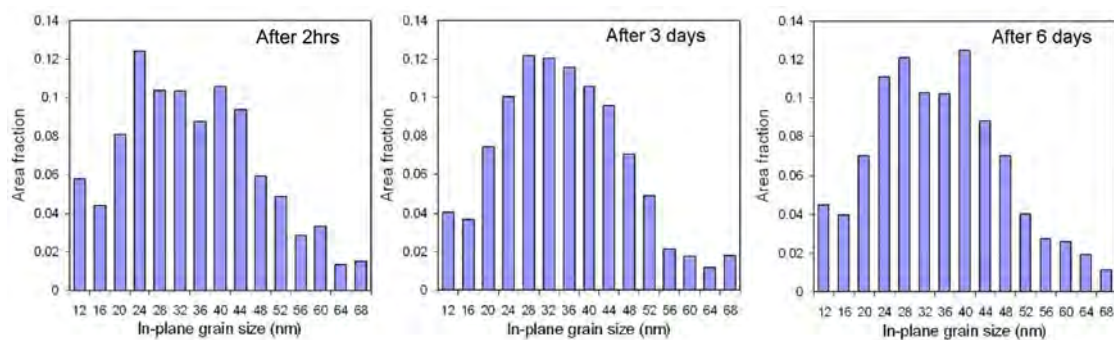
Figure 4.13 Grain size distribution of a Pd beam deformed at 0.6%. The average grain size is equal to 23±11 nm immediately after the first applied deformation) and 25±11 nm and 24±11 nm after 3 and 6 days respectively. The variation of the average grain size is below the spot size used in the scan (~8 nm). The grain size can consequently be considered as constant upon relaxation (performed by L. Malet at ULB).

4.4. Conclusions

The on-chip testing technique in combination with time-resolved observation of the relaxation mechanisms yields data difficult to obtain using classical methods during long periods of time. The technique is compatible with fully in-situ analysis in case of faster relaxation rates or if an external perturbation is added to slightly modify the load equilibrium condition such as with a small temperature change. The observation that dislocations can dominate both the hardening and relaxation behaviors in the present <110> textured columnar nc materials even at 30 nm grain size opens perspectives to control the mechanical properties of nanostructured

materials. For instance, GB-mediated mechanisms which often lead to a high rate sensitivity of nc materials can be avoided or, at least, mitigated based on the average data obtained using ACOM-TEM experiments. The lack of GB mediated process can be attributed to the presence of a <110> textured columnar microstructure containing nanotwins. Also, the relaxation mechanisms observed in this study can be detrimental to the mechanical stability in applications involving Pd-based nanobeams or membranes.

Chapter 5

5. Formation of 9R phase in nanocrystalline palladium films due to dissociation of $\sum3\{112\}$ incoherent twin boundary during hydriding

5.1. Introduction

As explained in chapter 1, thin Pd membranes can be used in hydrogen technology applications such as purifications and sensing applications. These Pd membranes must be as thin as possible to ensure high hydrogen permeability while remaining mechanically stable. Therefore, obtaining high mechanical properties in nc films is getting more attention in recent years.

Recently, the production of fcc nc metallic systems with nanotwinned structures has obtained new interests in the field of materials with ultra-high mechanical performances. Nanotwinned fcc metals exhibit a combination of high strength, ~1 GPa in ultrafine-grained Cu [50,52,173] and in nc Cu foils [53,140] and high ductility with more than 10% elongation to failure in ultrafine-grained Cu [50,52,173]. This unusual high strength/ductility balance originates from $\sum 3\{111\}$ CTBs which act as strong barriers for slip transfer of lattice gliding dislocations as well as sources for dislocation multiplication. Atomistic simulations are used to study the interactions of TBs with lattice glide dislocations with respect to both the kinetics and energetics of slip transfer across the CTBs [174-176].

Apart from $\sum 3\{111\}$ CTBs, $\sum 3\{112\}$ incoherent TBs (ITBs) were recently observed in epitaxial nanotwinned Cu films [177-181]. ITBs in fcc metals have been studied using HRTEM and molecular static and dynamic simulations [178-188]. The results show that $\sum 3\{112\}$ ITBs can be represented as an array of SPDs on every $\{111\}$ plane. Figure 5.1(a) shows the schematic illustration of an ITB in an fcc crystal (based on atomistic simulation results [177]). The SPDs along the ITB consist of $\mathbf{b_1}$, $\mathbf{b_2}$ and $\mathbf{b_3}$ partial dislocations with a repeatable sequence $\mathbf{b_2}$:$\mathbf{b_1}$:$\mathbf{b_3}$. The character of these SPDs is shown in Fig. 5.1(b) which represents the plan-view observation of a (111) stacking in the fcc crystal. The Burgers vector $\mathbf{b_1}$ is equal to $\frac{1}{6}[11\bar{2}]$, a pure edge partial dislocation. However, $\mathbf{b_2}$ and $\mathbf{b_3}$ are equal to $\frac{1}{6}[\bar{2}11]$ and $\frac{1}{6}[1\bar{2}1]$, respectively, which are mixed partial dislocations containing opposite sign screw components.
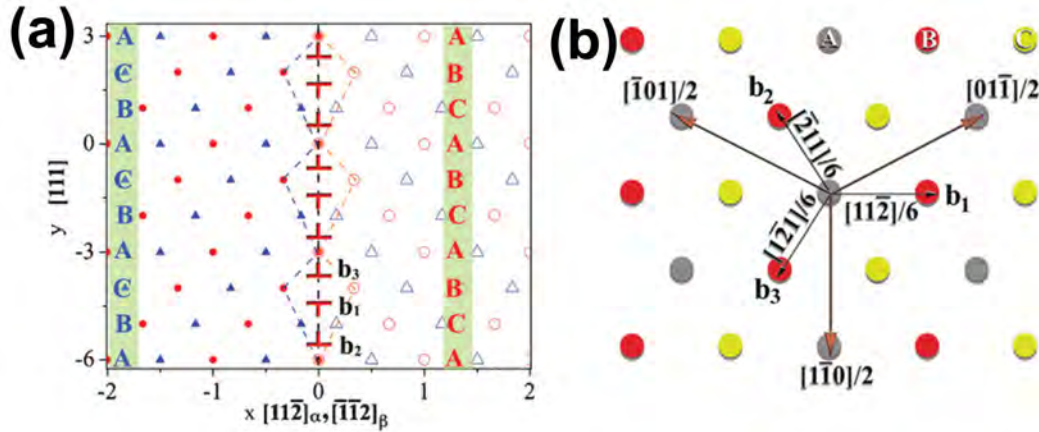
Figure 5.1 (a) schematic illustration of the ITB structure containing a set of partial dislocations on every (111) plane with a repetitive sequence **b₂**:**b₁**:**b₃**. (b) The character of the partial dislocations is shown in plan-view observation of a (111) stacking in the fcc crystal [after 177].

An ITB can dissociate into two tilt walls bounding a 9R phase. The dissociation occurs by the emission of one set of SPDs on every three {111} planes in the fcc structure [182,183]. Very recently, in-situ TEM and MD simulation studies have addressed the mobility of ITBs under external mechanical loading in nanotwinned Cu [177]. Because of their incoherent character and of the presence of glissile partial dislocations at the twin/matrix interfaces, $\sum$3{112} ITBs could migrate under moderate applied stress causing twin expansion or detwinning, depending on the sign of the applied shear stress, thus affecting the mechanical behavior of nanotwinned metals.

$\sum$3{111} nanoscale growth CTBs have been observed in e-beam evaporated nc Pd thin films dedicated to hydrogen permeation [58,141]. It was also demonstrated that, under uniaxial tension the presence of these boundaries contributes to an enhanced strength-ductility balance of nc Pd films by providing both increasing resistance to dislocation motion with deformation and a source for dislocation multiplication at the $\sum$3{111} CTBs [58,69,141]. However, the characterization of $\sum$3{112} ITBs in nc Pd as well as the effect of hydrogen loading on the structural properties and on the stability of both $\sum$3{111} CTBs and $\sum$3{112} ITBs has not been addressed in the literature.

In this study, nc Pd films with nanoscale growth $\sum$3{111} CTBs and $\sum$3{112} ITBs were produced using sputter deposition and subjected to hydriding cycles at UCL. The evolution of the internal stress within the films was monitored in-situ. The microstructure changes of the TBs under hydrogen loading were investigated using HRTEM and compared to recent experimental and simulation works in the literature.

5.2. Materials and methods

Pd films with 150 nm thickness were sputter-deposited at UCL at room temperature with a deposition rate of 0.3 nm s^{-1} and an argon plasma pressure of 1.07 Pa. The hydriding cycles were performed after pumping down a vacuum chamber to base pressures better than 10^{-6} mbar, after which ultra-pure Ar/H$_2$ gas mixtures are introduced into the chamber to instantaneously impose a desired total pressure (p_{H_2}= 97.5 mbar). In order to measure the internal stress in Pd films during hydriding, a high-resolution curvature measurement setup is mounted onto the hydriding chamber, and which continuously detects the positions of multiple laser beams reflecting off a cantilevered sample, hence monitoring the sample curvature in real time [25] (Fig. 5.2(a)). The change in internal stress in the Pd layer, which is the result of the restricted in-plane expansion during Pd–H interaction in the film-on-substrate geometry, can be derived from the measured changes in curvature [189]. Figure 5.2(b) shows the evolution of the internal stress as a function of time during a complete hydriding cycle at p_{H_2}= 97.5 mbar. This pressure is large enough to induce the α→β transformation in nc Pd [23-25]. The formation towards the β-phase causes a 10% volume change, which will induce plastic deformation within the Pd film (see section 1.2.2 for further details).

After hydriding, the system returns to ambient conditions, i.e. room temperature and atmospheric pressure. The hydrogen is released from the film and TEM specimens are prepared ex-situ.
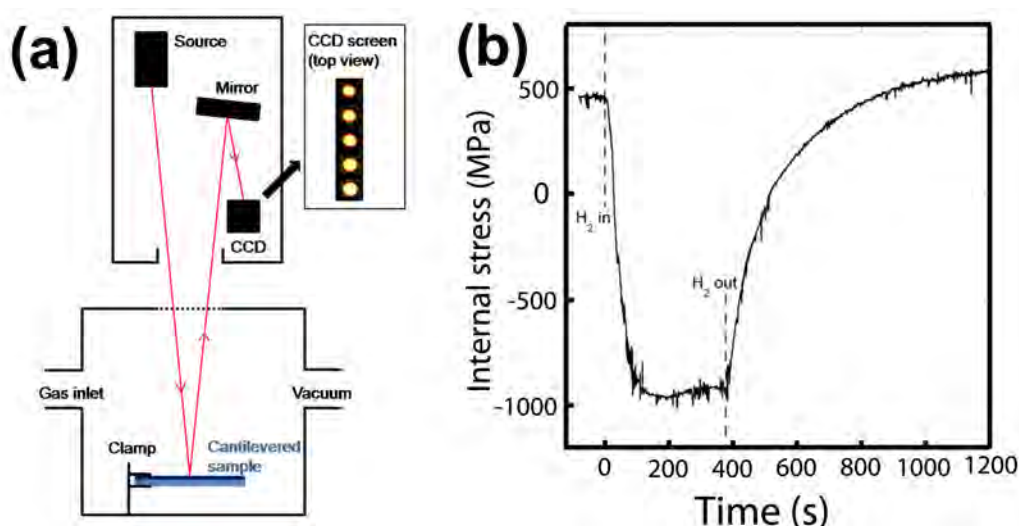

Figure 5.2 (a) the schematic illustration of a high-resolution curvature measurement setup [after 23]. (b) Example of the evolution of the internal stress as a function of time during a hydriding cycle recorded at p_{H_2}=97.5 mbar.

Conventional and HRTEM characterizations of the films before and after hydriding were carried out using a TECNAI G2 (FEG, 200 kV). A FEI Titan 80-300 "cubed" microscope with aberration correctors for imaging and probe was also used to reveal the near-core properties of defects. Cross-sectional and plan-view TEM thin foils were prepared using FIB thinning with the "lift-out" procedure.

5.3. Results and discussion

5.3.1. As-sputtered nc Pd film

Figure 5.3(a) shows a BF image of a plan-view Pd sample before hydriding, i.e., as-deposited. The corresponding SAD pattern of the same sample covering a circular area with a diameter of 200 nm is shown in the upper right inset. The obtained ring pattern shows the fcc Pd crystalline structure. The distribution of the in-plane grain size as measured from such BF and similar DF micrographs of both plan-view and cross-section Pd samples is shown in Fig. 5.3(b). The average in-plane grain size is equal to 26±1 nm while the cross-sections reveal a columnar morphological texture with an average elongated aspect ratio (height/lateral dimension ratio) of 3. Moreover, growth nanotwins are observed within the grains. Some of these twins are indicated by white arrows in the BF micrograph of Fig. 5.3(a). Moreover, Fig. 5.3(c) shows a HRTEM image of a single grain along a <110> zone axis. This HRTEM image reveals parallel $\sum 3\{111\}$ CTBs connected by a $\sum 3\{112\}$ ITBs. The corresponding FFT pattern taken from Fig. 5.3(c) is shown in the upper right inset of the same figure, indicating the twin relation in the FFT pattern.

In Fig. 5.3(d), the local **g**-map technique was applied on the HRTEM image of Fig. 5.3(c) to reveal the interplanar spacing variations as well as the exact position of the dislocations. The incoherent character of the $\sum 3\{112\}$ ITBs can be clearly distinguished in this **g**-map with an array of misfit dislocations located at $\sum 3\{112\}$ ITBs/matrix interface. The extra half planes related to these dislocations are also indicated by white arrowheads in Fig. 5.3(c). No local core relaxation of the $\sum 3\{112\}$ ITBs with possible formation of 9R phase can be distinctly resolved in Fig. 5.3(c) and 5.3(d). This result is in agreement with the MD calculations of Wang et al. [182] which predict a dissociation distance at $\sum 3\{112\}$ ITBs of 0.5 nm in Pd in the absence of mechanical stress. This dissociation distance corresponds to 1.81$|\mathbf{b_p}|$ where $|\mathbf{b_p}|$ is the length of the partial dislocation Burgers vector in Pd. This small dissociation distance is due to the high SFE of Pd ranging between 130 and 180 mJ.m^{-2} [167].
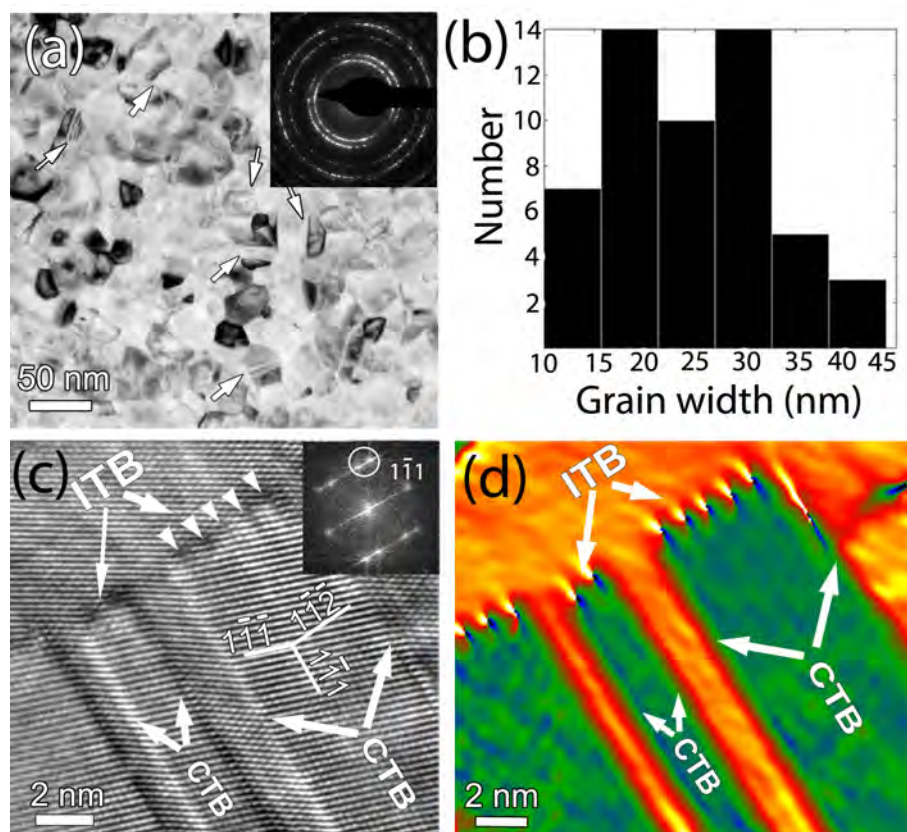
Figure 5.3 (a) BF micrograph of a plan-view FIB specimen prepared from as-deposited Pd film. Growth twins are shown by white arrows. (b) Grain width distribution of as-deposited Pd film. (c) [110] HRTEM micrograph in an as-deposited cross-section specimen showing $\Sigma 3\{111\}$ CTBs and $\Sigma 3\{112\}$ ITBs. (d) Local **g**-map obtained with the two diffracting vectors indicated by a circle in (c) (i.e., $1\bar{1}\bar{1}$ in the matrix and 002 in the twin).

5.3.2. Characterization of $\Sigma 3\{111\}$ CTBs in Pd film after hydriding/dehydriding cycle

The measurement of internal stress of Pd film during hydriding provides the value and the sign of the initial internal stress in the as-deposited films. Figure 5.2(b) shows that the stress in the as-deposited Pd film is tensile and is equal to 450 MPa. A gas mixture of $Ar/(H_2\ 1\%)$ was introduced in the chamber to instantaneously generate the desired P_{H_2}. As a result the internal stress increases rapidly in the compressive direction, and gradually reaches a constant value of -920 MPa corresponding to an absolute change of stress equal to 1370 MPa. After 380s, the gas mixture was then pumped out of the chamber, resulting in a gradual decrease of the internal stress due to room temperature dehydriding.

The ex-situ TEM investigation of the Pd film after such a hydriding/dehydriding cycle is presented in this section. The measurement of grain size using BF and DF images shows that no significant changes of the grain size and/or grain morphology were observed after hydriding. Therefore, the following sections focus on the effect of the hydrogen loading on the structure of the $\sum 3\{111\}$ CTBs and $\sum 3\{112\}$ ITBs in the Pd films (Fig. 5.3(c) and (d)).

Figure 5.4(a) and (b) show HRTEM micrographs along the [110] zone axis containing nanoscale $\sum 3\{111\}$ CTBs before and after hydriding of the Pd films. The $\sum 3\{111\}$ CTBs have lost their coherency after hydriding which can be attributed to the interaction of full lattice dislocations with $\sum 3\{111\}$ CTBs inducing different types of structural irregularities such as residual sessile dislocations at the TBs or lattice dislocations tangling in front of the TBs [45,58]. This is also in agreement with the strong but local intensity variations within the HRTEM image shown in Fig. 5.4(b). This is characteristic of large elastic strains related to a high dislocation density within the matrix, as confirmed by local **g**-mapping shown in Fig. 5.4(c). The local **g**-map is taken from the region indicated by dashed lines in Fig. 5.4(b). The increase of dislocation density after hydriding can be attributed to the increase of the internal stress during hydriding. Indeed, during hydrogen loading, the internal stress experienced by the film at equilibrium (~920MPa) is significantly higher than the macroscopic yield stress of the same film (580 ± 50 MPa [69]) allowing the generation and glide of a vast amount of dislocations in the majority of the grains. Moreover, mismatch dislocations could form during the $\alpha \rightarrow \beta$ transformation occurring at $p_{H_2} = 97.5$ mbar in order to release part of the excess energy stored at the phase boundaries. The literature on coarse-grained Pd shows that the dislocation density increases by three orders of magnitude when the value of the relative difference in the specific volumes $\Delta V/V$ of α and β reaches about 8% due to the $\alpha \rightarrow \beta$ hydride phase transformation [25].
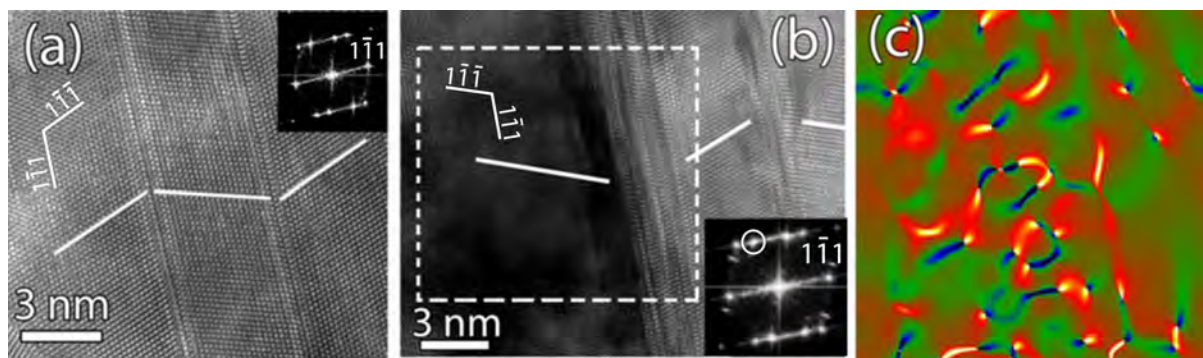
Figure 5.4 (a) [110] HRTEM micrograph of a nc grain of Pd thin film before hydriding showing a Σ3{111} CTBs. (b) [110] HRTEM image showing Σ3{111} CTBs after hydriding. Note the clear loss of the TB coherency after H loading due to the interaction with lattice dislocations. (c) Local **g**-map from the region indicated by dashed lines in (b) using **g** =$\bar{1}$11.

5.3.3. Characterization of ∑3{112} incoherent TBs in Pd film after a hydriding/dehydriding cycle

5.3.3.1. 9R formation after hydriding the Pd film

Figure 5.5 shows a [110] oriented HRTEM micrograph of a straight band exhibiting two common {111} interfaces with the fcc matrix in a hydrided Pd sample. Careful analysis of this band reveals a dissociation-like morphology with a change of contrast every three planes similar to a 9R structure. Unfortunately, the HRTEM images seldom reveal the perfect stacking as clear a dot pattern due to internal stresses, possible stacking defects or the overlapping between the 9R structure and the matrix caused by the small grain size.
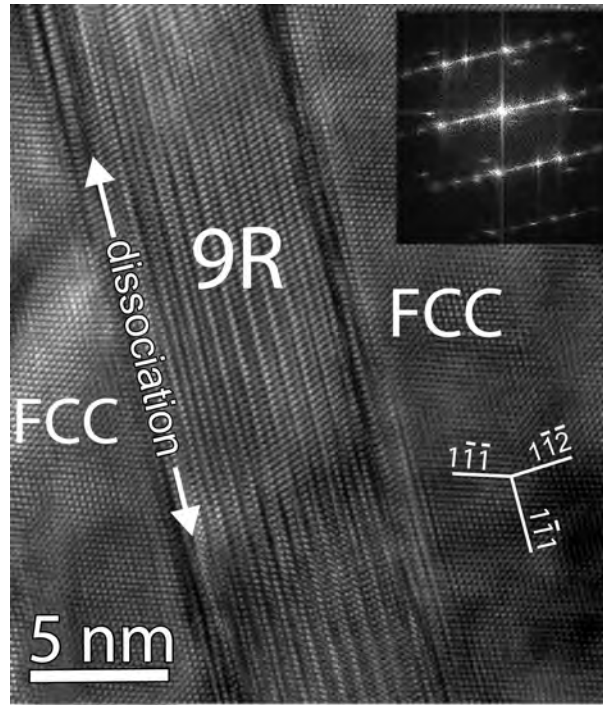
Figure 5.5 [110] HRTEM image of 9R band embedded in the Pd matrix after hydriding. corresponding FFT pattern is shown in the upper right inset.

Moreover, the observation of the contrast in this figure is not sufficient to confirm the fcc→9R transformation. Indeed, there are two possibilities which could explain the three layer periodic contrast of Fig. 5.5. One is the formation of a 9R structure with the emission of one SF every three {111} planes in the fcc structure and the resulting stacking sequence of ABCBCACAB [191,192]. The other possibility is an overlapping twin-matrix configuration which reveals an almost similar HRTEM contrast [191,192]. In the present work, based on the analysis of the FFT pattern of the HRTEM images (see the next section) the three-layer periodic contrast observed in the band of Fig. 5.5 was attributed to a genuine 9R phase region.

5.3.3.2. Distinguishing between the 9R structure and twin/matrix overlapping

In the literature, in order to distinguish the true 9R structure from an overlapping region between twin and matrix grains, both occurring in twinned materials and both causing an extra threefold periodicity in the <110> HRTEM images of an fcc lattice, the local diffraction patterns must be analyzed in detail [191,192]. In the present work, both situations occur, as seen from the comparison in Fig. 5.6, in which the low magnification HRTEM images look very much alike. In both cases, the FFT reveals a superperiodicity of 1/3 in the <111>

direction corresponding with the long period of the image. The difference between both cases can be observed from the actual position of these 1/3 extra spots in the first rows next to the central <111> row. For a true 9R structure, observed along a <110>$_{fcc}$ direction, none of the spots in these rows coincides with the center normal to the <111> long period axis, as seen in the example of Fig. 5.6(a). On the other hand, for the overlapping case, this normal crosses the middle spot in the adjacent row, as seen in Fig. 5.6(b) (for a detailed explanation on the origin of this difference see [191,192]). This method was essential in the present study to discriminate between the 9R and twin/matrix overlapping. Because of the nanometer size of the grains and the resulting three-dimensional microstructure of the FIB foils, 9R often overlaps with matrix and the exact stacking sequence of the 9R phase cannot be resolved in most cases.
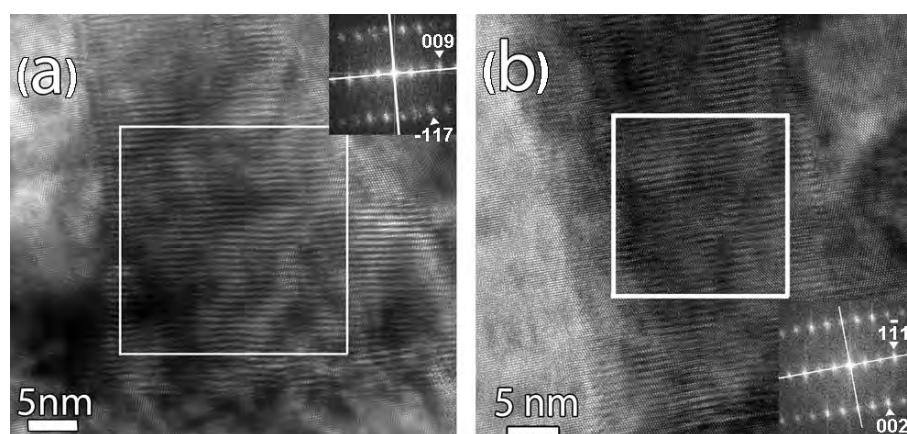
Figure 5.6 HRTEM micrographs along [110]$_{fcc}$ orientation and corresponding FFT patterns of (a) 9R structure and (b) overlap structure of twin and matrix for Pd thin film after hydriding. The FFT was performed from the regions indicated by white squares.

5.3.3.3. HRTEM investigation of 9R structure after hydriding

Using the method explained in section 5.3.3.2, numerous large 9R domains were observed in the Pd samples after hydriding. The sizes of the observed 9R regions and thus the dissociation width of the $\sum 3\{112\}$ ITBs are in the 5 to 30 ±1 nm range. Figure 5.7(a) shows an example of a smaller 9R region after hydriding indicating that not all regions involve extended dissociation. The inserted FFT of Fig. 5.7(a) also shows the twin relationship between both matrix sides of the 9R region (the latter being too small for a proper FFT), which confirms also the dissociation of the $\sum 3\{112\}$ ITB into the 9R structure. Fig. 5.7(b) exhibits a local **g-**

map of the region indicated by solid lines in Fig. 5.7(a); the misfit dislocations located at the two 9R phase boundaries can clearly be observed.

In the area indicated by dashed lines in Fig. 5.7(a), the exact stacking is revealed from the HRTEM lattice micrograph, further enlarged in Fig. 5.7(c). It is obvious from the enlarged image that there are some stacking defects within the perfect 9R sequence. The reason for the formation of stacking errors within the 9R phase can presumably be attributed to the presence of secondary GB dislocations. These dislocations form to accommodate small angular deviations from the ideal $\sum 3$ coincidence orientation [140,193,194]. In the present study, 4 and 5-layer stacking defects have been observed.
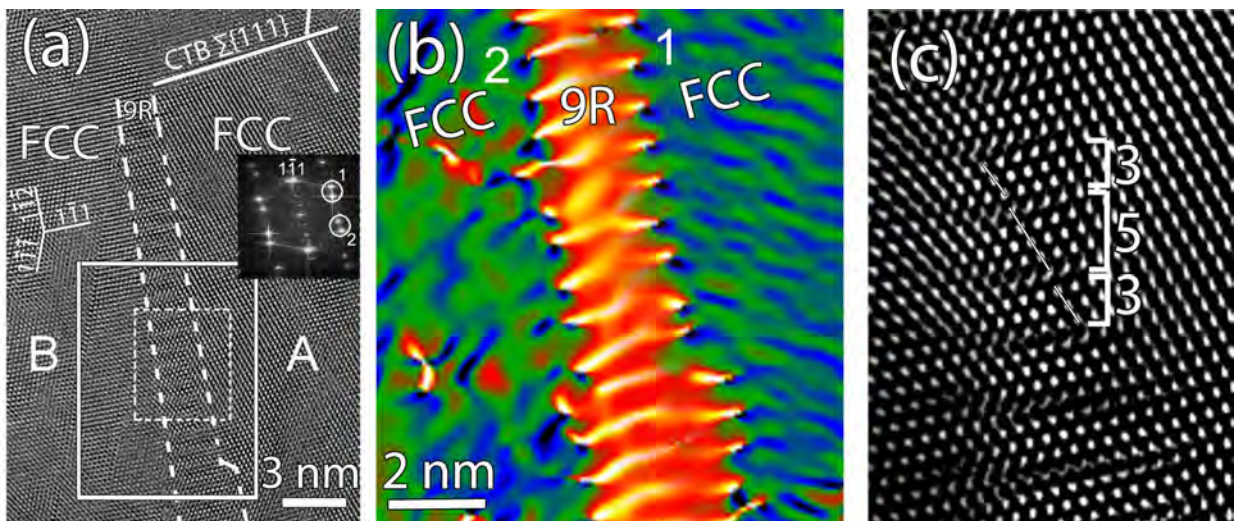
Figure 5.7 (a) [110] HRTEM image of narrowly dissociated $\Sigma 3\{112\}$ ITBs with the corresponding FFT pattern showing the local 9R structure fingerprint. (b) Collated local **g**-map of the region indicated by solid lines in the HRTEM image of (a). Phase boundaries 1 and 2 were obtained using the pairs of diffracting vectors indicated by circles 1 and 2 in (a). Circle 1 includes $\mathbf{g} = 1\bar{1}\bar{1}$ from region A in the twin and $\mathbf{g} = \bar{1}14$ from the 9R band while circle 2 involves $\mathbf{g} = 1\bar{1}\bar{1}$ from region B in the matrix and $\mathbf{g} = \bar{1}1\bar{5}$ from the 9R band. (d) Enlargement of the region of (a) indicated by dashed lines showing a (defected) atomic stacking sequence of the 9R phase.

This 9R structure was not reported before in nc Pd. This observation is unexpected when considering the high SFE of Pd. The same stacking has been observed in other metals such as Au [184,185], Ag [186-188] and Cu [178-181] in which the formation of a 9R phase can be explained, supported by atomistic simulations [182,183], based on the low and moderate SFE

of these materials and the dissociation at the ITBs. This surprising result raises several questions regarding the driving force(s) responsible for the formation of the 9R phase during the hydriding of the Pd films.

Based on molecular static and dynamic simulations, Wang et al. [182,183] estimated that the 9R phase forms because the dissociation of a $\sum 3\{112\}$ ITB is driven by the accompanying decrease of the core energy of the boundary or due to the presence of stress associated to the Peach-Koehler force. These two factors can operate simultaneously in the Pd films. The increase of the internal stress (Fig. 5.2(b)) during the α→β transformation in hydrided Pd films could facilitate this dissociation process.

Wang et al. [182,183] also performed atomistic simulations for the movement of ITBs (phase boundary migration) under shear stresses τ_{xy} acting in the interface plane of different fcc metals. Fig. 5.8 shows the shear stress as a function of the applied shear strain. The results show that the stress-strain curve gradually increases and then becomes flat. It can be seen from Fig. 5.8 that the required shear stress for the phase boundary migration of an ITB is dependent on the SFE. The critical value of the shear stress required for the activation of the dissociation process (the flat part in the stress-strain curve) decreases with decreasing SFE [182].
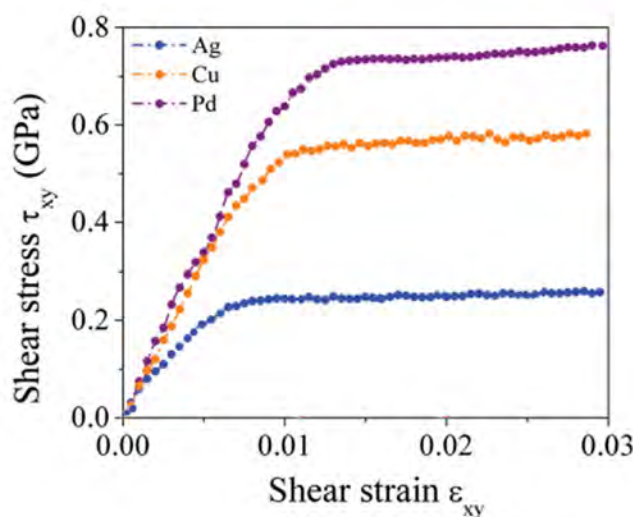
Figure 5.8 Mechanical response of ITBs in different fcc metals when the bicrystal model is subjected to shear stresses acting in the ITB plane [after 182].

Wang et al. [182,183] proposed that, under an applied shear stress of 0.7 GPa (Fig. 5.8), the 9R phase can expand in Pd by the migration of ITBs in the direction favoured by the applied force acting on the more mobile phase boundary. The formation of 9R phase is attributed to the emission of the $\mathbf{b_1}$ SPDs gliding on every three $\{111\}$ planes in the fcc structure (and

present in an ITB) when subjected to an applied stress. In contrast with the partials $\mathbf{b_1}$, the mobility of the partials $\mathbf{b_2}$ and $\mathbf{b_3}$ is significantly reduced since these two partials attract each others because of their opposite sign screw components.

In the present work, the internal (compressive) stress reached during the hydriding of the Pd films was about 0.92 GPa (Fig. 5.2(b)). The corresponding maximum shear stress is equal to 0.46 GPa. However, significant variations of the local stress will exist from grain to grain [69] due to differences in crystal orientation, in twin orientation, in grain size and in the presence or lack of twins. Furthermore, very local stress concentration can be present near TBs due to the presence of dislocations at these TBs. It is thus reasonable to envisage that a fraction of the twins undergo a resolved shear stress near or above 0.7 GPa. The microstructure and accompanying stress heterogeneities explain also the wide variations in the extension of the 9R domains. The presence of hydrogen could also contribute to the dissociation of ITBs and to the expansion of the 9R phase by reducing the SFE of Pd and, as a consequence, the critical value of the shear stress required for the activation of the dissociation process (Fig. 5.8). Very recently, Apostol et al. [195] have used atomistic calculations to investigate the effect of a (111) hydrogen layer embedded in Al on the GPFEs. The authors demonstrated that the presence of hydrogen reduces the stable and unstable SFEs relative to pure Al. Assuming the same effect in Pd, when the hydrogen is released at the end of the hydriding cycle, the SFE should increase towards its initial value and lead to a reversible contraction of the 9R domains. The fact that extended 9R regions persist can be attributed to the high density of dislocations generated within the grains during the hydrogen loading (Fig. 5.4(b)). These dislocations stabilize the 9R phase by acting as pinning centers for the two 9R phase boundaries. Besides, due to the high surface/bulk ratio of the films, the free surface and the film/substrate interface could also play a role by hampering the reverse motion of the two-phase boundaries bounding the 9R phase. Indeed, the more mobile phase boundary could easily escape to the surface due to the strong attractive image forces applied on the phase boundary dislocations. These dislocations can also be incorporated in the film/substrate interface. Several HRTEM observations have indeed revealed 9R domains ending at the film/substrate interface or at the free surface of the films.

5.4. Conclusions

The effect of the α↔β phase transformation during hydriding and dehydriding on the microstructure changes of sputtered Pd thin films has been investigated by TEM. Results

show that volume changes of α and β phase during hydriding induce internal stress which is higher than the yield stress of the film. This leads to an increase of dislocation density stored within the nanograins. No grain growth was observed after hydriding. It is also demonstrated that the {111} nanoscale growth twins lose their coherency. Surprisingly, $\sum 3\{112\}$ ITBs largely dissociate after hydriding into two-phase boundaries bounding a new and thermodynamically unstable 9R phase. The observation of this phase which corresponds to single SF located every three {111} planes in the fcc structure is not expected here because of the high SFE of Pd.

Chapter 6

6. Hydriding of nc Pd thin films

In this chapter, first the effect of initial microstructure on the hydriding mechanisms of the nc Pd films will be presented. Then, the effect of hydriding on the microstructure changes of Pd films will be documented using advanced TEM techniques.

6.1. Effect of initial microstructure on the hydriding behavior of nc Pd films

6.1.1. Introduction

As explained in section 1.2.4, increased attention is recently paid on clean and renewable energy systems due to environmental concerns such as emissions of pollutants produced by fossil fuels. Hydrogen technology is seen as a clean alternative [29] and Pd proofs to be a good candidate for hydrogen storage, hydrogen purification and sensing applications due to its large hydrogen absorption capacity [23]. Pd has also high sensitivity and selectivity of hydrogen gas and can release hydrogen at room temperature [23].

Microstructure plays a key role in the mechano-chemical properties of materials, including their hydriding properties. In particular, the microstructure of a metal can offer several types of hydrogen trapping sites [29], in the bulk as well as in the surface and subsurface layers. In the case of nanostructured Pd, the contribution of GBs, lattice defects, etc. to the total hydrogen content becomes significant. For thin films, this is supplemented by surface effects which make thin films attractive to study microstructural aspects of hydriding.

In the case of nc thin films, the high density of GBs as well as the disordered nature of these defects offer a high concentration of low-energy trapping sites for the absorbed hydrogen atoms [196]. Moreover, the introduction of dislocations and growth twins during deposition may also affect the hydriding mechanisms. Dislocations play an important role in the hydriding of metals, as the hydrostatic stress component of the hydrogen atoms strongly interacts with the local tensile stress field of an edge dislocation [29,197]. Dislocations can also be created by both hydrogen absorption/desorption [29], where they accommodate the lattice mismatch present when the hydride phase nucleates and grows/shrinks in the solid solution. The exact role of twins on the hydrogen absorption by metals remains unclear. Several authors claim that twins can act as hydrogen traps [42,198], but not all studies confirm these observations.

In this study, the microstructure of the Pd films has been controlled by annealing for 20 min at 300°C in order to eliminate part of the defects massively generated by the room temperature magnetron sputtering deposition. The annealing process has been coupled to a high-resolution in-situ curvature measurement system in order to be able to compare the hydriding properties of the annealed films with as-deposited specimens exhibiting the same initial internal stress state, and to correlate the stress evolution with defect recovery. Many authors indeed identified direct relationships between the stress evolution during annealing and the density of

GBs [199,200], point defects [201,202] and dislocations [199,202,203]. The twin concentration can also be expected to be affected by annealing [204,205], but should not give rise to volume changes, and hence to stress changes (although twin is expected to affect the hydriding behavior). Defect statistics obtained by TEM will finally be compared with the internal stress data obtained during annealing and hydriding in order to identify the defects responsible for the microstructural effects on the hydriding equilibrium and kinetics.

6.1.2. Result and discussion

Figure 6.1 shows two hydriding cycles recorded at similar hydrogen partial pressures which induce the α-phase. One of the Pd films used in these experiments has been directly cut out of the deposited wafer exhibiting 491 MPa initial internal stress, while the second one comes from the other deposition process and has undergone an annealing cycle for 20 min at 300C inside the quartz tube so that these films have very close internal stress levels before hydrogen introduction. It is obvious from Fig. 6.1 that the as-deposited specimen exhibits a faster hydriding kinetics than the annealed specimen. The time needed for chemical equilibrium to be reached between gaseous hydrogen in the quartz tube and atomic hydrogen inside the annealed sample is one order of magnitude longer than the as-deposited Pd film. The time needed for chemical equilibrium raises from about 100 sec for the as-deposited specimen to about 1000 sec for the annealed specimen (Fig. 6.1). This is the expected behavior for a film containing less growth defects. As discussed above, some of these growth defects such as GBs, dislocations and twins have recently been shown to act as pathways for hydrogen transport, thereby potentially accelerating the kinetics of mechanisms such as surface-to-bulk transition or diffusion of hydrogen atoms. This issue will be quantitatively considered in the next section.
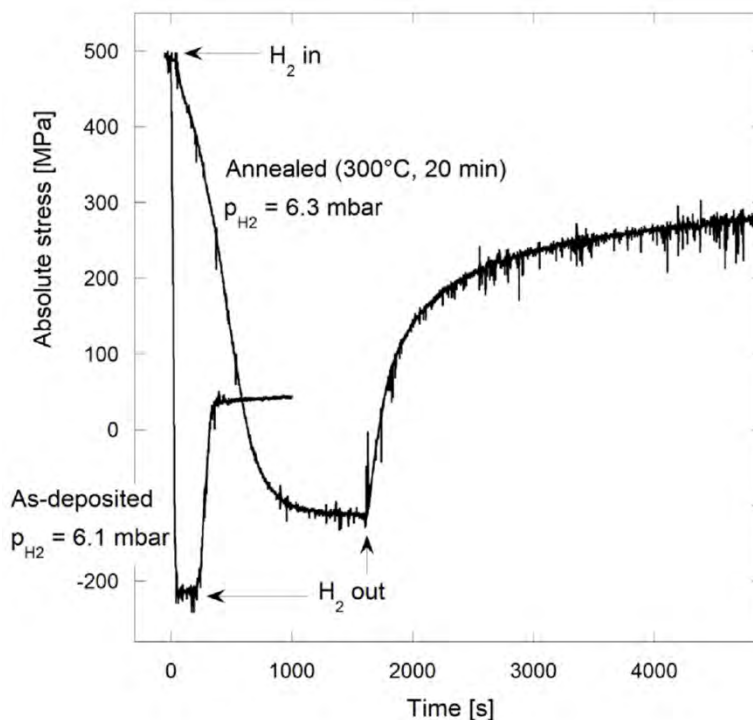
Figure 6.1 Evolution of the internal stress as a function of time during two hydriding cycles to α-phase recorded using an as-deposited Pd thin film and a film annealed 20 min at 300°C, respectively.

Figure 6.2(a) and (b) show cross-sectional BF-TEM images obtained in as-deposited and annealed Pd films, respectively. Figure 6.2(a) reveals the columnar nanograin morphology of the films. It can be seen that several grains are confined within the thickness of the films, i.e. most grains do not run through the entire film thickness. The SADP (repeated on different regions throughout the sample) shown in the lower right part of Fig. 6.2(a) reveals that the film exhibits a strong <111> fcc crystallographic texture. Some growth twins indicated by white arrows can be observed in Fig. 6.2(a). The HRTEM image of Fig. 6.2(c) obtained along <110> direction exhibits an example of Σ3{111} growth TBs observed in the as-deposited films. Figure 6.2(b) shows that, together with the 525 MPa of tensile stress generated during the annealing cycle, both the morphological texture and the crystallographic texture have been conserved after annealing. However, a clear increase of grain size and aspect ratio of the grains accompanied with a decrease of the number of growth twins can be qualitatively seen in Fig. 6.2(b).
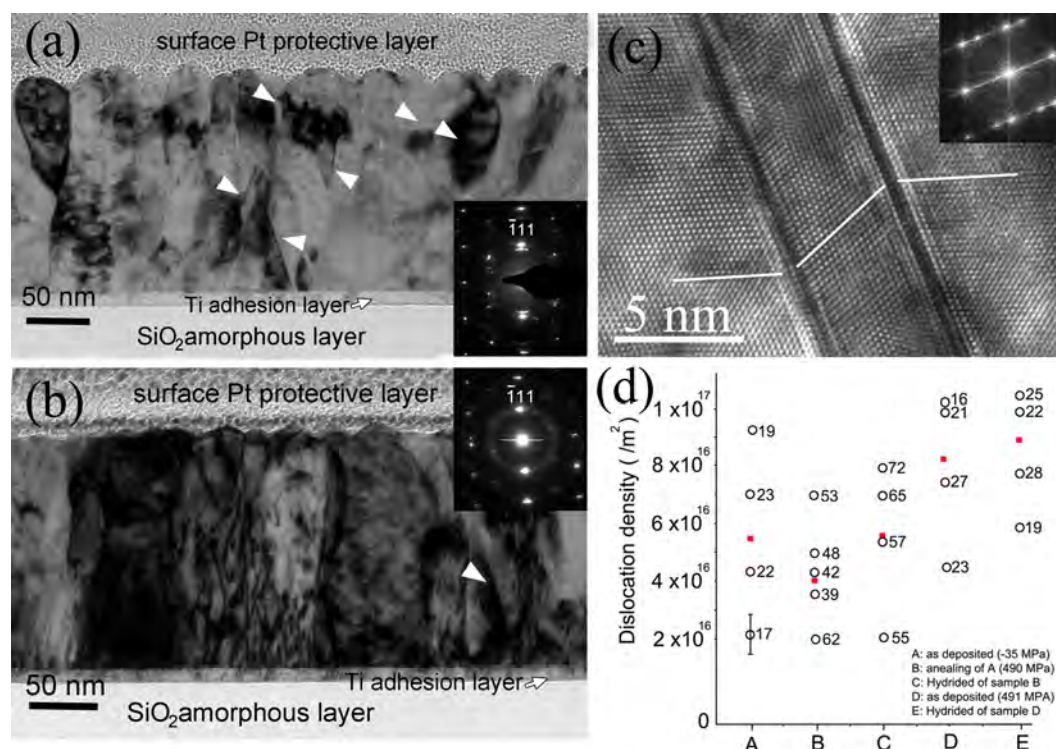
Figure 6.2 BF micrographs of cross-sectional FIB foils of (a) as-deposited Pd films and (b) after annealing at 300 ˚C for 20 min. Growth twins are indicated by white arrows. Corresponding SADPs are presented in each figure. (c) HRTEM image of growth TBs in the as-deposited films. (d) Average dislocation density (red solid squares) evolution in the Pd films. Numbers beside unfilled circles indicate the corresponding grain size (nm) of individual measures.

Statistical analysis of grain size and TB density has been performed using BF-TEM and DF-TEM in the as-deposited, annealed and/or hydrided Pd films. Around 100 grains for each film were included in the analysis. Table 6.1 summarizes the result of such analysis. First of all, it is clear that both the height and the width of the grains are affected by the grain growth induced by annealing. The average height of the grains increased by a factor 1.6, while their width was more affected, increasing by a factor 1.9. The fraction of GBs was thus significantly reduced, in the plane of the film as well as in the direction perpendicular to this plane. The presence of a higher GB density in the as-deposited films improves the hydriding kinetics. Additionally, the GBs offer low-energy sites for hydrogen, which leads to the increase of the solubility of hydrogen in the α-phase of the Pd-H system [196].

Figure 6.2(d) shows the evolution of dislocation density measured using HRTEM in as-deposited, annealed and/or hydrided Pd films. The scatter in these measurements is caused by

the local nature, i.e., individual nc grains, used for the HRTEM based measures. The dislocation density decreases by 27% after annealing, therefore reducing the hydriding kinetics [41,206].

The TB density has also been decreased by 41% (see Table 6.1) after annealing. It is worth mentioning here that growth TBs were observed to be connected to GBs. Thus, the decrease of the TB density after annealing is probably due to the shrinking and the disappearance of grains containing twins. Finally, one can notice that, except for the slight increase of dislocation density shown in Fig. 6.2(d), hydrogen cycling in the α-phase does not significantly modify the defect concentrations (see Table 6.1 and Fig. 6.2(d)).

Table 6.1 Argon plasma pressure p_{Ar} for sputtering, deposited Pd film thickness t_f, average initial internal stress σ_0 and TEM defect statistics of the Pd films studied in this work: grain height (perpendicular to the plane of the film) and width (in the plane of the film), aspect ratio (minimum and maximum values), TB and dislocation density. Data is provided for as-deposited specimens, as well as after annealing and hydriding (α-phase transformation).

p_{Ar} [Pa]	t_f [nm]	σ_0 [MPa]	Specimen state	Grain height [nm]	Grain width [nm]	Aspect ratio [-]	TB density [$1/\mu m^3$]	Dislocation density $\times 10^{16}$ [$1/m^2$]
0.92	157	491	As-dep.	81 ± 6	31 ± 3	1 - 4	9300 ± 600	8.1 ± 1.4
			After H_2	86 ± 7	30 ± 3	1 - 4	9500 ± 600	8.8 ± 1.2
0.46	156	-35	As-dep.	102 ± 13	42 ± 6	1 - 4	8600 ± 500	5.5 ± 1.5
		490	After anneal.	160 ± 5	79 ± 5	1 - 2	5100 ± 300	3.9 ± 0.9
			After anneal. + H_2	162 ± 6	82 ± 5	1 - 2	5200 ± 400	5.6 ± 1.3

6.2. Nanoscale plasticity mechanisms after hydriding/dehydriding cycle of nc Pd thin films

6.2.1. Introduction

Although several experimental studies have been dedicated to the study of the effect of hydrogen on the microstructure and mechanical properties of bulk coarse-grained Pd such as the evolution of dislocation density and hardness after hydriding [207,208], experimental evidences on the elementary plasticity mechanisms activated in nc Pd thin films under hydrogen loading are still missing in the literature. This is a critical point since these mechanisms may strongly differ from those reported in bulk Pd due to the small grain size and the predominance of GBs in nc Pd films. Similar to nanostructured bulk metallic materials, forest hardening mechanisms and dislocation networks are often not favored in nc metallic thin films [58]. Indeed, nc materials have a large population of GBs which are effective sources and sinks for dislocations. Dislocations once emitted from a GB may be absorbed rapidly by an opposite GB due to the very small grain size [166]. Additionally, at very small grain sizes, GB mediated processes such as GB sliding [209,210], GB migration [101,211] and grain rotation [171,172] can be activated at room temperature.

Another unexplored aspect concerns the effect of hydriding on nanoscale growth twins recently reported in as-deposited nc Pd thin films [59]. The formation of these twins has been attributed to the dissociation of high energy GBs during deposition, in spite of the high SFE of Pd (130-180 mJ.m^{-2}) [44,59]. On the other hand, to the best of our knowledge, studies on dislocation/hydrogen interaction in Pd and on the effect of hydriding on the SFE of Pd have not yet been addressed in the literature. Only few investigations using simulations have recently tackled these questions in other metals such as Ni, Al and α-Iron (Fe) [212,213]. Because of the complexity of the microstructure of nc Pd films, the microstructural changes associated to the effect of hydrogen on the SFE of Pd may strongly differ from coarse-grained Pd. Indeed, in nc metals, depending on the grain size and the local stress, the nucleation of leading partial dislocations from GBs can be favored over the formation of full lattice dislocations even in high SFE metals [214]. In the present study, this feature is seen to be further enhanced with a possible decrease of SFE in hydrided nc Pd. Furthermore, because of the very small grain size and the increase of the internal stress accompanying the hydriding process, the leading partial can easily annihilate at the opposite GB leaving wide SFs which can act as twinning precursors [166,214].

It is also confirmed that the initial volume of the Pd structure expands by about 10% when the H/Pd ratio reaches 0.5 (for β-phase transformation), which induces a large plastic deformation within the material [23-25]. It is confirmed that structural swelling of Pd upon hydrogen loading by interstitial introduction of the hydrogen atoms can result in the closing of nanoscopic gaps followed by a decrease in net electrical resistance of the system [32]. On the other hand, the volume changes of the Pd lattice by hydrogen loading may lead to the generation of dislocations within the Pd matrix which can affect the mechanical properties of the system (please see chapter 5).

In the nc Pd thin films used in the present study, the structural properties of the hydrides (i.e., nucleation sites, size distribution, interaction with dislocations and interfaces, etc.) can be strongly affected by both the extrinsic (i.e., dimensions) and intrinsic (i.e., microstructure) effects. Finally, there is no doubt that the accumulation of irreversible microstructural changes during hydriding cycles on nc Pd films can alter the mechanical properties of these films (i.e., ductility, hardening, creep, etc). Defects generated in hydrided nc Pd used in sensing applications can also have other effects such as shortening of a sensing cell's lifetime, interruption of the electrical circuitry and lowering of the device's sensing sensitivity and proficiency [33]. Therefore, it is of primary importance to uncover the elementary plasticity mechanisms activated during hydriding of nc Pd thin films.

In the present study, we have performed advanced TEM characterizations on nc Pd thin films prepared using sputter deposition and hydrided at low (for α-phase transformation) and high pressures (for β-phase transformation). The internal stress developing within the films during hydriding has been monitored in-situ. Statistical analyses of the grain size/morphology as well as the crystallographic texture have been performed using ACOM-TEM while aberration corrected high resolution TEM has been used to unravel the nature and the near-core properties of the defects generated during hydriding. The results revealed strong interaction of hydrogen with extended defects as well as a clear effect of hydrogen on both the stable and unstable planar fault energies of Pd. The effects of these mechanisms on the hydrogen cycling and on the mechanical properties of nc Pd films are discussed and compared to recent works in the literature.

6.2.2. Materials and methods

Pd films with 150 nm thickness were sputter deposited (for further details see section 5.2). The hydriding/dehydriding cycles were performed at total pressure of p_{H_2}=2.26 for α-phase and 97.5 mbar for β-phase formation. A high-resolution curvature measurement setup is used to monitor the internal stress changes of the Pd film with time [23].

Conventional BF, DF and HRTEM characterizations of the Pd films were carried out using a FEI Tecnai G2 (FEG, 200 kV) and a FEI Titan 80-300 "cubed" microscope with aberration correctors for imaging and probe.

BF and DF techniques were used to obtain quantitative data on grain size (width and height), aspect ratio of grains, TB density and the fraction of grains containing TB in cross-section samples. HRTEM was used to investigate the microstructure changes at the atomic scale and to measure the evolution of dislocation density induced by hydriding. Dislocation density was measured by counting extra half planes in HRTEM images. For better visualization of extra half planes, a mask was applied on each **g** vector and then IFFT was generated showing one family of planes. Since, a dislocation induces the lattice strain in 3D, therefore, this procedure was used for all main spots presented in a given FFT pattern. Therefore, the dislocation density was calculated based on the number of extra half planes presented in all IFFT images. In order to allow easy visualization of single dislocations, local **g**-maps were also used (for further details see section 3.2.1). The evolution of the grain size distribution and the crystallographic texture of the Pd films were investigated using ACOM-TEM in a CM20 (LaB$_6$, 200 kV) microscope equipped with the ASTAR hardware at ULB. FIB thinning with the ''lift-out'' procedure was used for the preparation of both cross-section and plan-view TEM thin foils.

6.2.3. Results

6.2.3.1. Internal stress evolution during hydriding of nc Pd films

Figure 6.3 shows the evolution of the internal stress as a function of time during a complete hydriding cycle of Pd films at p_{H_2}= 2.28 and 97.5 mbar which correspond to α- and β-phase transformations, respectively. The internal tensile stress in the as-deposited Pd films is ~450 MPa. After inserting a gas mixture of Ar/(H$_2$ 1%), the internal stress decreases rapidly in the compressive direction, and gradually reaches a constant value of 120 MPa tensile stress for the α-phase transformation (curve 1 in Fig. 6.3) and 920 MPa compressive stress for the β-phase transformation (curve 2 in Fig. 6.3). This leads to an absolute change of stress of 330

MPa and 1370 MPa, for Pd films hydrided to α- and β- phase, respectively. The gas mixture was then pumped out of the chamber after 225s and 380s for Pd films hydrided to α- and β-phase, respectively, resulting in a gradual decrease of the internal stress due to reversible dehydriding at room temperature. These results will be used to discuss the role of the internal stress building up during hydriding on the activation of plasticity mechanisms.
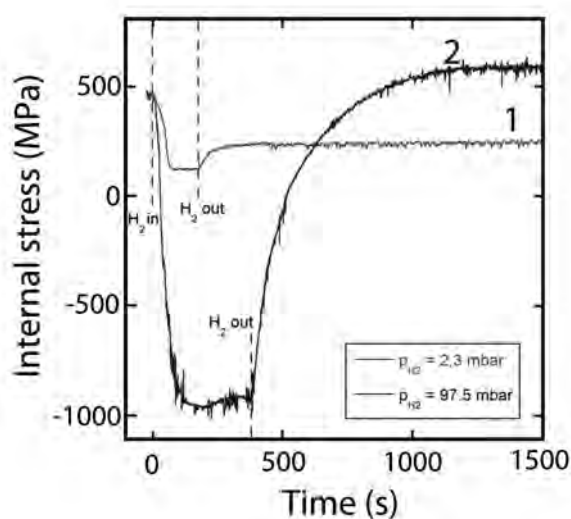
Figure 6.3 Evolution of the internal stress in nc Pd thin films as a function of time during hydriding cycles recorded at p_{H_2}= 2.28 and 97.5 mbar, the former transforms to the α-phase, the latter transforms to the β-phase.

6.2.3.2. TEM characterizations of nc Pd films before and after hydriding
In this section, ex-situ TEM analyses of hydrogen induced plasticity mechanisms have been performed on thin foils prepared by FIB on as-deposited Pd films as well as after dehydriding (i.e., at ambient conditions).

6.2.3.2.1. Effect of hydriding on grain size and crystallographic texture
First, the ACOM-TEM technique was performed before and after hydriding of nc Pd films in order to investigate the contribution of GB mediated processes such as grain growth, GB sliding and/or grain rotation. Figure 6.4(a) and (b) show the ACOM-TEM results including orientation maps and crystallographic texture analysis along <100>, <110> and <111> directions which were performed on plan-view FIB samples of Pd films before and after hydriding to β-phase, respectively. It is worth noting that the presence of more than one grain

across the thickness of the TEM thin foils can affect the automated indexation of the diffraction patterns leading to severe uncertainties on the ACOM-TEM results. In the present work, the plan-view foils have been thinned using FIB to ensure that only one grain is confined through the thickness. Furthermore, in order to avoid ambiguities for the analysis of the grain size distribution, all CSL boundaries such as $\sum 3$ TBs, have been excluded in the ACOM-TEM measurements. The results show that the average lateral grain size in as-deposited Pd film is 61 ± 20 nm and slightly increases to 72 ± 20 nm after hydriding to β-phase, which can be compared with the investigation of the mean grain size after hydriding to α-phase which did not show significant changes (i.e., 60±5 nm). However, because the above increase after β-phase hydriding still falls within the uncertainties of the measurements, the activation of grain growth under hydrogen loading cannot be confirmed.

The analysis of the average crystallographic texture in the as-deposited films reveals a sharp {111} fiber texture normal to the film surface (Fig. 6.4(a)) which corresponds to the minimum surface energy of fcc metallic films. From Fig. 6.4, and even without performing an extensive quantitative analysis, it is clear that the texture intensities along <100>, <110> and <111> directions remain constant after the hydriding/dehydriding cycle to β-phase. As expected, similar results were obtained in Pd films hydrided to α-phase. These observations indicate that, within the angular resolution limit of the ACOM-TEM technique (~1°), GB mediated processes such as GB sliding and grain rotation that can affect the local grain orientation (i.e., the crystallographic texture of the films) can be excluded as dominant plasticity mechanisms in hydrided Pd films.

However, due to the large data spread in the grain size histograms, it is possible that the ACOM-TEM data of Pd films before and after hydriding/dehydriding are not conclusive. An alternative would be to study the hydriding effect in-situ. Due to the high vacuum condition in a conventional TEM, it is however not possible to hydride the sample in-situ, although special holders can be designed to allow gas pressure on the sample site. Therefore, in the present work, only ex-situ TEM studies were performed on the same Pd sample before and after hydriding using ACOM-TEM technique. Any reversible rotation of grains during dehydriding is not expected due to high internal stress induced during hydriding to β-phase which leads to irreversible plastic deformation in the Pd films (see below).
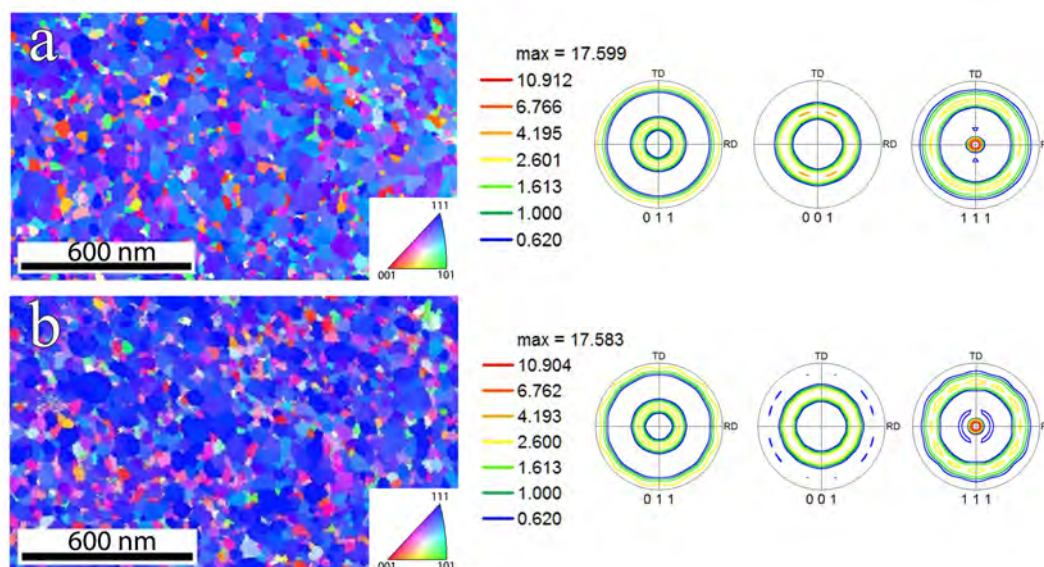
Figure 6.4 Orientation mapping and crystallographic texture along <100>, <110> and <111> directions on plan-view FIB samples prepared on (a) as-deposited Pd film and (b) Pd film after hydriding to β-phase.

6.2.3.2.2. Effect of hydriding on dislocation density

Figure 6.5(a) shows a BF image obtained from a cross-sectional FIB foil of an as-deposited Pd film. It can be seen that the films exhibit a morphological texture with columnar grains elongated parallel to the growth direction with an average elongated aspect ratio (height/lateral) equal to ≈ 2. The SADP shown in the upper right inset of Fig. 6.5(a) reveals a preferential crystallographic orientation of the nanograins along the <111> direction which is consistent with the ACOM-TEM results reported in Fig. 6.4(a). ∑3{111} coherent growth twins were occasionally observed as indicated by white arrows in Fig. 6.5(a). Figure 6.5(b) shows a HRTEM image of such a growth ∑3{111} CTB. The inserted FFT pattern in Fig. 6.5(b) shows a typical twin relationship for ∑3{111} CTBs in the fcc structure. It can be seen that, except for a few atomic steps indicated by arrowheads, the TB is almost coherent and atomically sharp. The IFFT filtered HRTEM image in the lower right inset of Fig. 6.5(b) shows that these steps correspond to glissile twinning dislocations (TDs) of type **b**=a/6<112> stopping in the interior of the grain and along the CTB. No residual sessile dislocations such as sessile Frank dislocations or stair-rod dislocations have been observed at the CTBs. The local **g**-map shown in the upper left inset in Fig. 6.5(b) reveals a few lattice dislocations in the matrix. The upper right inset IFFT in the same figure reveals one full lattice dislocation. This is also in agreement with the absence of single or multiple SFs lying in the interior of the grains and at the vicinity of GBs or growth TBs. The origin of full lattice dislocations in the

as-deposited films can be attributed to the internal tensile stress developed during the deposition of the films (~ 450 MPa).
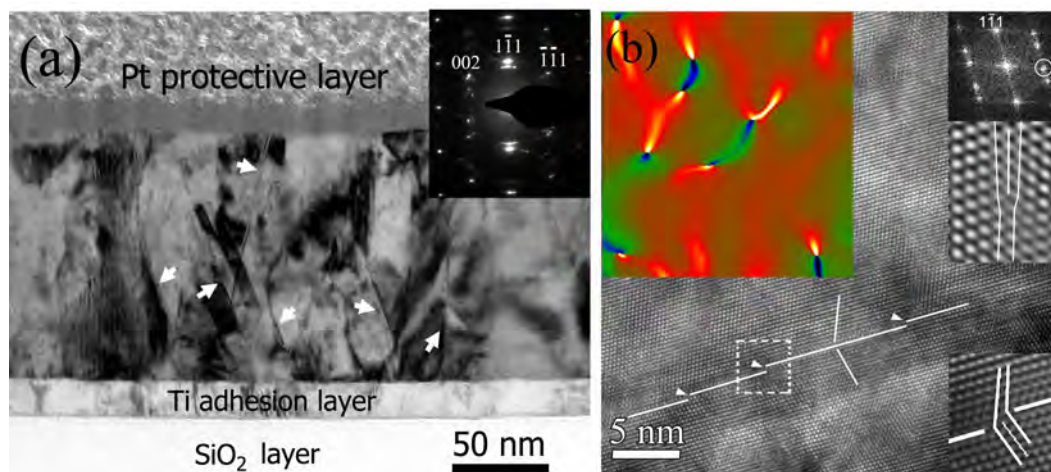
Figure 6.5 (a) BF micrograph of a cross-sectional FIB foil prepared from as-deposited Pd film. Growth twins are indicated by white arrows. SADP in the upper-right inset shows the preferential orientation of the grains along the <111> direction normal to the plane of the film. (b) <110> HRTEM micrograph of a $\sum3\{111\}$ CTB in the as-deposited Pd film. The local **g**-map shown in the upper left inset was obtained from the region covered by the map. The map was obtained using $\mathbf{g} = 1\bar{1}\bar{1}$ indicated by a white circle on the FFT in the upper right inset of (b). The lower right inset represents the IFFT of the region indicated by dashed lines, showing one twinning dislocation at the twin/matrix interface. The IFFT in the upper right inset reveals one full lattice dislocation in the matrix.

Figure 6.6(a) shows a <110> HRTEM image in a Pd film after hydriding to α-phase. In the upper right inset of this figure, one full lattice dislocation can be seen. Note that local dissociation of the dislocation core cannot be resolved similarly to dislocations observed in the as-deposited films (Fig. 6.5(a)). This is confirmed by the IFFT obtained with **g**=002 and shown in the lower left inset of Fig. 6.6(a). In contrast with Pd films hydrated to β-phase (see below), intrinsic or extrinsic SFs have not been observed in Pd films after hydriding to α-phase. Figure 6.6(b) and (c) show HRTEM images of a growth $\sum3\{111\}$ CTB and $\sum3\{112\}$ ITB respectively, observed in Pd film after hydriding to α-phase. The FFTs in these figures show a typical twin relationship for CTBs and ITBs in the fcc structure. It can be seen in Fig. 6.6(b) that, except for a few atomic steps due to the presence of a/6 <112> TDs, the TB is almost coherent and atomically sharp. Also, no local dissociation of the ITB of Fig. 6.6(c) into

two walls bounding a 9R phase was observed. This is also confirmed by the local **g**-map shown in the lower right inset of the same figure. The growth twin behavior is thus identical to those observed in the as-deposited films.

These results can be explained by the low amount of hydrogen incorporated in the Pd films during hydriding to α-phase leading to very limited hydrogen/defect interactions as well as the small variation of the internal stress during hydriding to α-phase (curve 1 in Fig. 6.3).
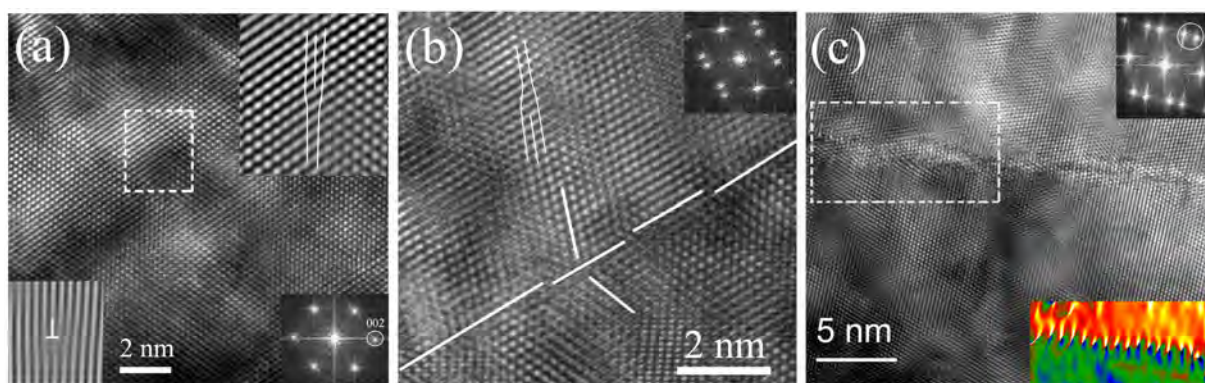
Figure 6.6 (a) <110> HRTEM micrograph of a nanograin in Pd film after hydriding to α-phase showing a full lattice dislocation. The IFFT filtered and magnified image from the region indicated by dashed lines is presented in the upper right inset showing the compact core of the dislocation. The IFFT of **g**=002 is also presented in the lower left inset. (b) <110> HRTEM micrograph of ∑3{111} CTB in the Pd film hydrated to α-phase showing the existence of a few steps along the TB. (c) HRTEM micrograph of a ∑3{112} ITB in Pd film after hydriding to α-phase. Local **g**-map from the region indicated by dashed lines in (c) is shown in the lower right inset of the same figure. This map was obtained with the two diffracting vectors, $\mathbf{g} = 1\bar{1}\bar{1}$ in the matrix and **g**= 002 in the twin, indicated by a circle in the FFT shown in the upper right inset of (c) and does not reveal any splitting of the ITB.

Figure 6.7(a) shows a HRTEM image obtained along the <110> zone axis in a Pd film after hydriding to β-phase. In this figure, it can be seen that the dislocation density has significantly increased after hydriding compared to the as-deposited films (Fig. 6.5). Indeed, strong local variations of contrast due to the presence of a high density of dislocations are observed in these samples. This is confirmed in the local **g**-map of the left inset in Fig. 6.7(a). Furthermore, in contrast with CTBs observed in the as-deposited films (Fig. 6.5), the ∑3{111} CTBs in Fig. 6.7(a) have lost their coherency after hydriding to β-phase. This loss of

coherency is due to the interaction of a high density of lattice dislocations with ∑3{111} CTBs inducing different types of structural irregularities such as residual sessile dislocations at the CTBs or lattice dislocations tangling in front of these boundaries [45,58,190].

Dislocation densities have also been quantified in HRTEM images obtained in as-deposited Pd as well as films hydrided to α- and β-phase as shown in Fig. 6.7(b). Note that the scatter of dislocation density is caused by the local nature of individual nc grains of HRTEM images, presented as individual measures (open circles). The measured average lattice dislocation density in as-sputtered Pd film equals $6.0\pm0.6\times10^{16}$ /m^2. A slight increase to $6.7\pm0.9\times10^{16}$ /m^2 has been observed in Pd film hydrided to α-phase (Fig. 6.7(b)). It has also been observed that the coherency of ∑3{111} CTBs has not much been affected during hydriding to α-phase. However, the measured lattice dislocation density in Pd film hydrided to β-phase reached $1.25\pm0.2\times10^{17}$ /m^2 which is almost 2 times higher than the initial density in as-deposited films in agreement with the clear loss of coherency of ∑3{111} CTBs shown in Fig. 6.7(a). The error bar on the individual measurements are obtained by enlarging or shrinking the selected region in the HRTEM image as long as the number of dislocations does not change, while those on the averages are standard error bars.
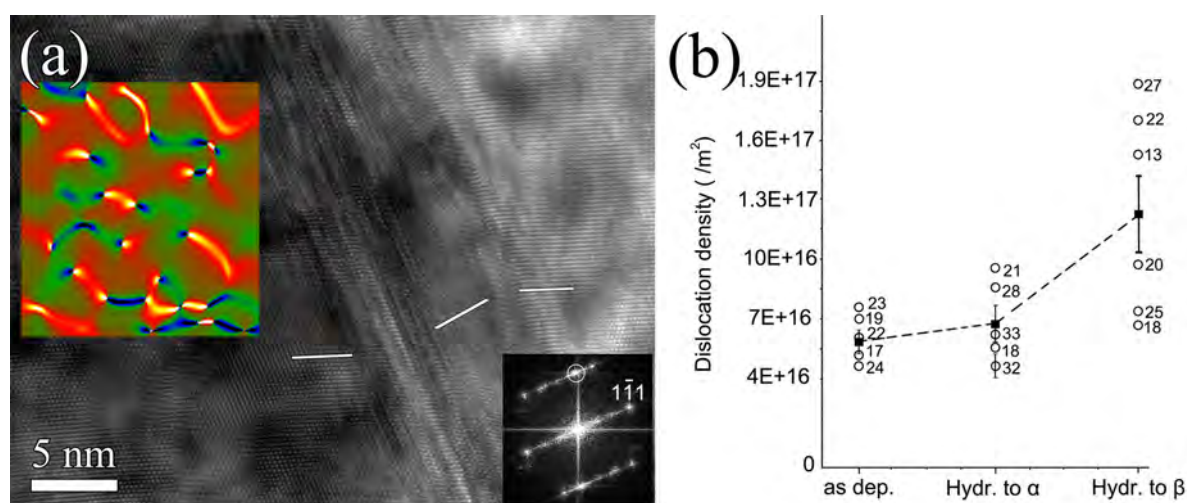
Figure 6.7 (a) HRTEM image showing the loss of coherency of ∑3{111} CTB after hydriding to β-phase. The corresponding FFT is displayed in the lower right inset showing the twin relation. The local **g**-map from the region covered under the map is shown in the upper left inset using **g** = 1$\bar{1}\bar{1}$ indicated by a white circle on the FFT. (b) Average dislocation density (filled squares) measured before and after hydriding to α- and β-phase. Numbers beside unfilled circles indicate the corresponding grain size (nm).

In order to quantify the loss of coherency of the TBs, the thickness of the TBs for as-deposited Pd and after hydriding to α and β-phase was measured by using the method explained in section 4.3.3.2. The results are shown in Fig. 6.8. It is clear that the TB thickness has not much been affected during hydriding to α-phase which is consistent with the dislocation density measurement after hydriding to α-phase (Fig. 6.7 (b)). However, the hydriding of Pd films to β-phase leads to an increase of the TB thickness by a factor of almost 3 compared with the as-deposited film, which is in agreement with the clear loss of coherency of $\sum3\{111\}$ CTBs shown in Fig. 6.7(a).
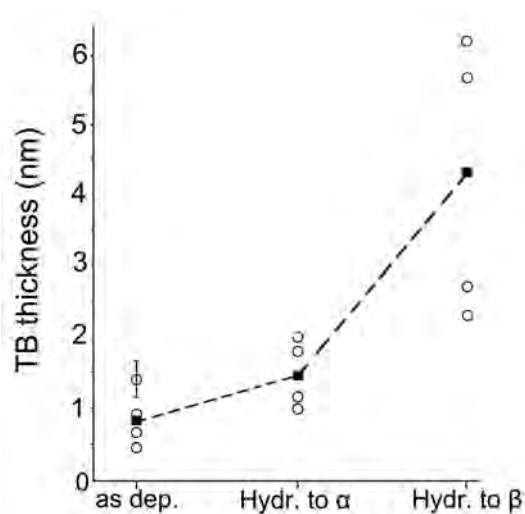
Figure 6.8 Average TB thickness (filled squares) measurement before and after hydriding to α- and β-phase. Numbers beside unfilled circles indicate the corresponding grain size (nm).

6.2.3.2.3. Effect of hydriding on the SFE of Pd

Figure 6.9 exhibits the effect of hydriding to the β-phase on the local structure of $\sum3\{112\}$ ITBs. Figure 6.9(a) shows a $\sum3\{112\}$ ITB connected to a $\sum3\{111\}$ CTB in the as-deposited Pd film. The FFT shown in the upper right inset confirms the typical twin relationship for $\sum3\{112\}$ ITBs in the fcc structure. The atomic structure of the $\sum3\{112\}$ ITB at the region indicated by dashed lines in Fig. 6.9(a) is magnified in Fig. 6.9(b). Local dissociation into a 9R phase cannot be resolved in Fig. 6.9(b) which is in agreement with the high SFE of as-deposited Pd. The compact core of the ITB of Fig. 6.9(b) is confirmed in the local **g**-map obtained in the same region and shown in the lower right inset of Fig. 6.9(b).

Figure 6.9(c) shows a <110> HRTEM image of another $\sum3\{112\}$ ITB dissociated into a 9R band embedded in the fcc Pd matrix after hydriding to β-phase. The corresponding FFT pattern characteristic of the 9R structure can be seen in the left top inset of Fig. 6.9(c). The

displacement of some of the spots from their original positions is due to small angular deviations from the ideal ∑3 60˚ twin relation. Note that the formation of the 9R phase at a ∑3{112} ITBs has not been observed after hydriding to α-phase (see Fig. 6.6(c)).

The influence of hydriding on the SFE of Pd as well as the presence of residual hydrogen atoms trapped at the defect cores can also be performed by investigating the presence of SFs and SPDs in the interior of the grains after hydriding using HRTEM. Indeed, only few perfect lattice dislocations and TDs lying at the growth TBs have been observed in the as-deposited films (Fig. 6.5(b)). However, in Fig. 6.9(c), several SFs can be observed indicated by white arrowheads. The enlarged and IFFT filtered HRTEM image shown in the bottom left inset of Fig. 6.9(c) shows the shift of the position of the {111} planes due to the presence of one SF.
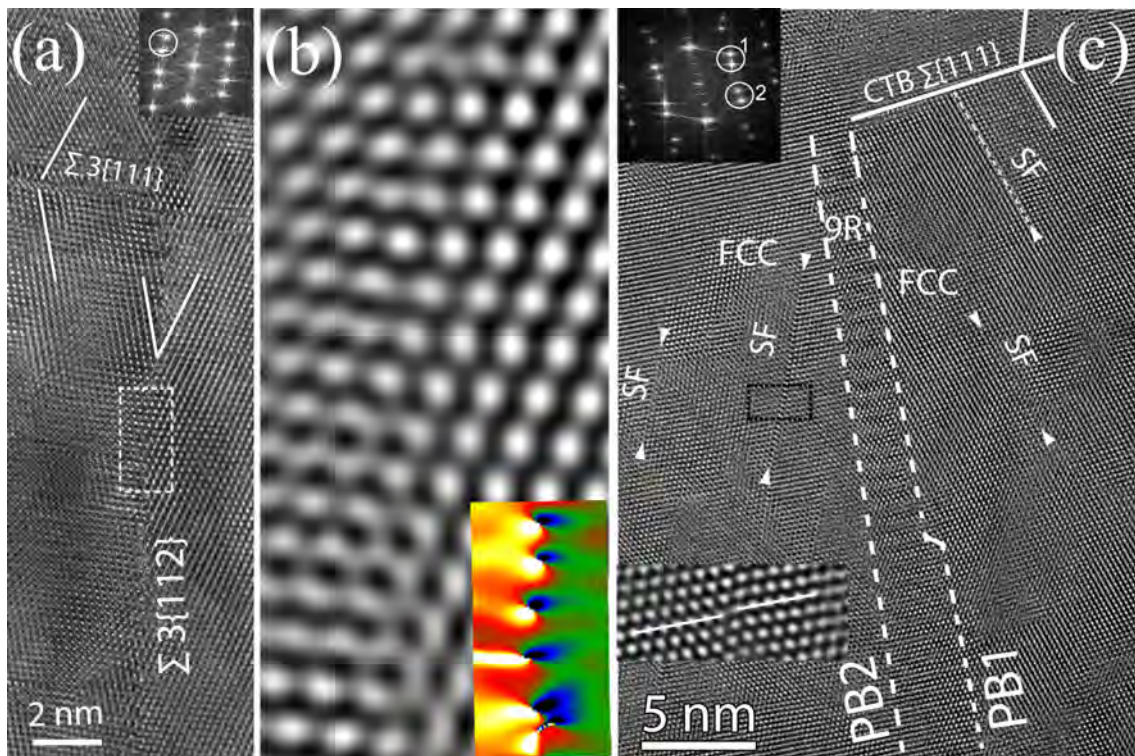
Figure 6.9 (a) HRTEM micrograph of an as-deposited cross-section FIB specimen showing a ∑3{112} ITB. (b) IFFT filtered HRTEM image obtained from the region indicated by dashed lines in (a) showing the atomic structure of the ITB. The local **g**-map of (b) obtained with the two diffracting vectors indicated by a circle in the inset of (a) (i.e., **g** = $1\bar{1}\bar{1}$ in the matrix and 002 in the twin) is shown in the lower right inset of the same figure. (c) <110> HRTEM image of a 9R band embedded in the fcc Pd matrix after hydriding to β-phase with the corresponding FFT pattern. Several SFs are indicated in the same figure by arrowheads.

Figure 6.10 shows a detailed HRTEM analysis of the nature of the SFs observed in nc Pd films after hydriding to β-phase. A HRTEM image obtained along a <110> zone axis can only accurately reveal the width of a SF when the two partial dislocation lines enclosing the SF are exactly parallel to the electron beam direction. However, in reality, these partials are often not perfectly parallel to this viewing direction and may not even be straight especially near the TEM foil surface which can yield some blurring of the lattice shifts across the apparent SF line. In the present study, only SFs with a clear lattice shift are reported.

Figure 6.10(a) shows one nanograin containing SFs located in the grain interior and connected to GBs. The enlarged IFFT of the HRTEM image of Fig. 6.10(b) shows the SF1 observed in the grain of Fig. 6.10(a). This SF was identified as a Shockley partial faulted loop formed during hydriding to β-phase. Indeed, both the IFFT of the $(\bar{1}11)$ family of planes and the local **g-**map in Fig. 6.10(b) show two partial dislocations with opposite Burgers vectors bounding the SF. In the same figure, the Burgers circuits drawn around the two partials, which are starting and ending at the SE, show that the Burgers vectors are equal to 2/3 of the distance separating two projected lattice points along the [112] direction. This confirms that the two partials are opposite 90° SPDs with $\mathbf{b} = \frac{a}{6}[112]$ and $\mathbf{b} = \frac{a}{6}[\bar{1}\bar{1}\bar{2}]$. The measured width of the Shockley partial faulted loops in different grains of Pd hydrided to β-phase varies between 2.9 nm and 5.8 nm.

Intrinsic SFs originating from the dissociation of lattice dislocations have also been observed. An example of such a feature is shown in Fig. 6.10(c) (i.e., SF2 of Fig. 6.10(a)). The Burgers circuits drawn around the partials show 30° and 90° SPDs of type $\mathbf{b} = \frac{a}{6}[112]$ and $\mathbf{b} = \frac{a}{6}[2\bar{1}1]$, respectively. The 30° partial results in a vector of [112]/12, whose magnitude is 1/3 of the distance between the projected lattice points along the [112] direction ([112]/4) in the lattice image. This hampers the observation of the extra half plane of 30° partials as can be seen in the IFFT and local **g-**map of Fig. 6.10(c). Defining the electron beam direction as the $[\bar{1}10]$ in Fig. 6.10(c), the vector "SE" closing the circuit around the stacking fault is equal to 1/4[112], which is the projection of 1/2[101] onto the $(1\bar{1}0)$ plane, therefore the extended dislocation is a 60° mixed dislocation which is dissociated into 30° and 90° SPDs following a reaction such as: $\frac{1}{2}[101] \rightarrow \frac{1}{6}[112] + \frac{1}{6}[2\bar{1}1]$.
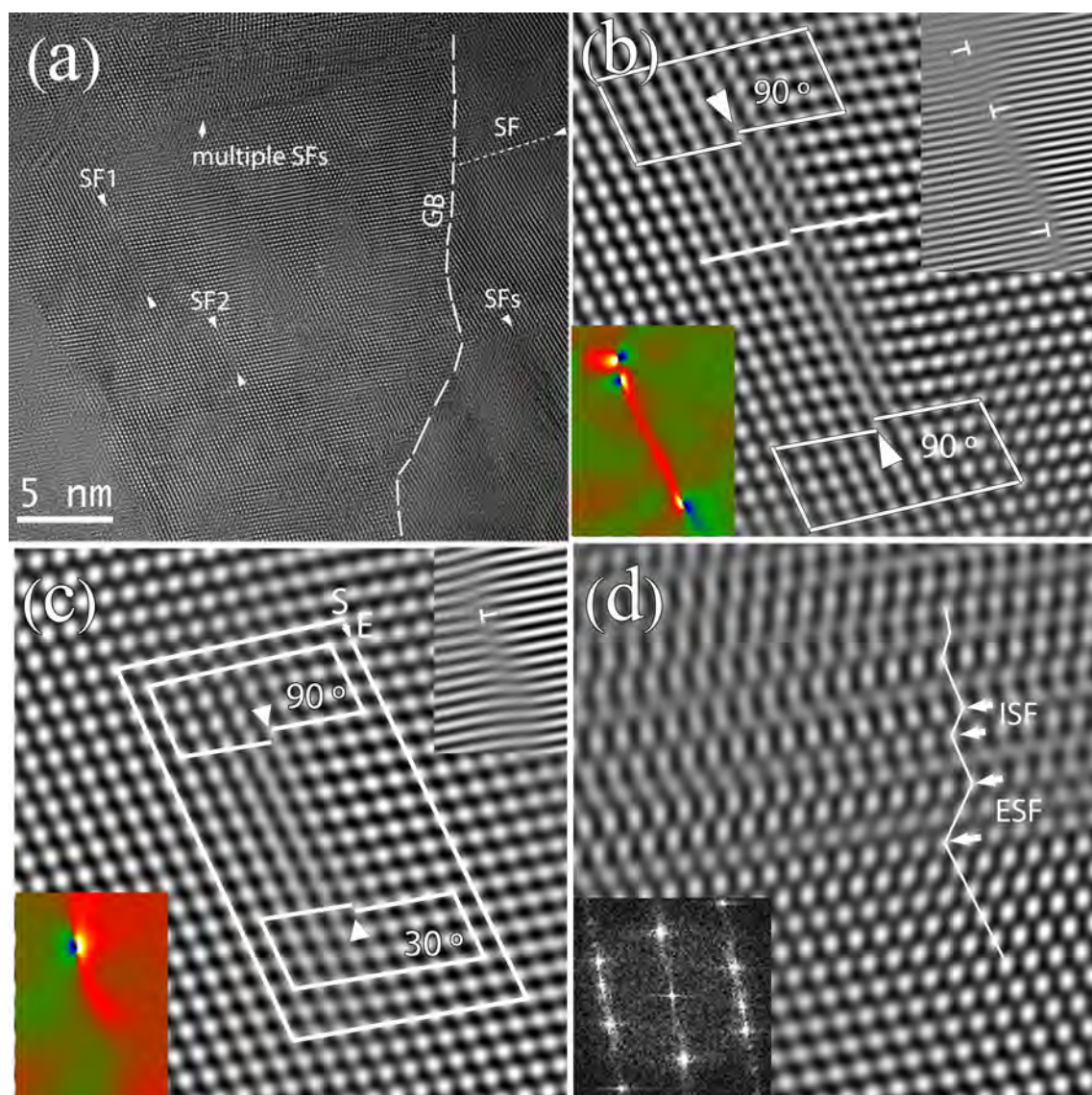
Figure 6.10 (a) SFs in Pd film after hydriding to β-phase. (b) Enlarged IFFT of SF1 in (a) showing the SF loop and its opposite 90° partial dislocations. IFFT of ($\bar{1}11$) plane and corresponding local **g**-map are shown in the upper right and lower left insets, respectively. (c) Enlarged IFFT of SF2 in (a) showing a dissociated 60° dislocation with intrinsic SF. Burgers circuits are drawn around the partials and the SFs. (d) Enlarged IFFT of multiple SFs in (a) showing intrinsic and extrinsic SFs.

A set of multiple SFs can be observed in the upper region of the grain of Fig. 6.10(a). The IFFT filtered HRTEM image obtained from the same region is shown in Fig. 6.10(d). It clearly shows changes of the stacking sequence of the fcc lattice due to the presence of a high density of parallel wide SFs. Figure 6.10(d) confirms the presence of intrinsic (i.e., one layer) and extrinsic (i.e., two layers) SFs. These SFs can transform locally into very thin twin bands leading to spot splitting in the FFT of Fig. 6.10(d). It is important to note here that a clear

distinction should be made between these very fine nanotwins accompanied by a high density of SFs and pre-existing growth twins in the as-deposited films and which generally appear as unfaulted individual variants. This can be related to the difference of the mechanisms controlling the nucleation and the evolution of these defects.

Figure 6.11 exhibits schematic illustrations of the nanoscale defect mechanisms activated in nc Pd films hydrided to β-phase and revealed using post-mortem TEM analyses in the present work. All these results confirm that local plasticity in nc Pd thin films hydrided to β-phase is mainly controlled by dislocations is spite of the small grain size. Moreover, it is worth mentioning that SFs and fcc→9R phase transformation have not been observed in as-deposited or Pd films hydrided to α-phase. The origin of this difference is discussed in the next section.
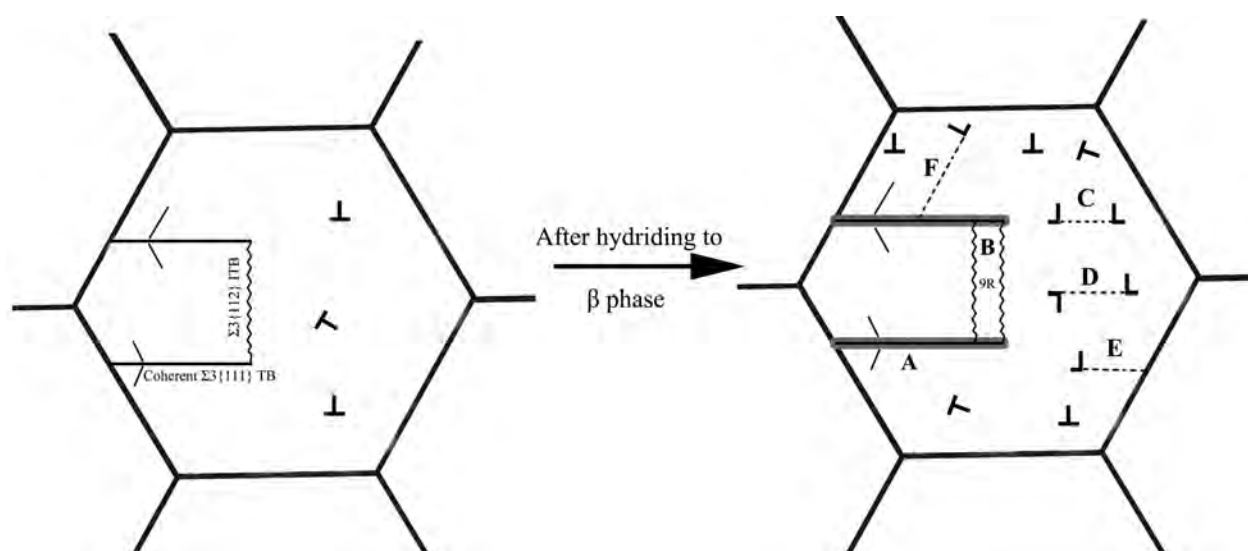
Figure 6.11 Schematic illustrations of the different nanoscale plasticity mechanisms (A to F) activated in nc Pd films hydrided to β-phase: (A) loosing the coherency of ∑3{111} TB due to interaction of dislocation with TB (B) dissociation of ∑3{112} ITB and formation of 9R phase (c) formation of SF by dissociation of a lattice dislocation (d) formation of faulted loops (e, f) formation of SF by movement of leading partial from GB and TB, respectively. "T" symbols represent the perfect lattice dislocations, "Γ" symbols shows the SPD.

6.2.4. Discussion

The present results demonstrate that hydriding cycles to β-phase induce significant increase of dislocation density in nc Pd thin films (Fig. 6.7(b)). Such a feature can be attributed to the internal stress building-up during hydriding to β-phase. Indeed, the internal stress experienced by the films during β hydriding at equilibrium (~920 MPa plateau in Fig. 6.3) is significantly higher than the macroscopic yield stress of the same films (580 ± 50 MPa) [69] allowing the generation and the glide of a vast amount of dislocations in the majority of the grains. Dislocations can nucleate from GBs as well as at the matrix/β hydride interfaces to accommodate the lattice mismatch at these interfaces. In contrast, the small variations of the internal stress during hydriding to α-phase (~120 MPa in Fig. 6.3) can explain the slight increase of dislocation density measured in these films (Fig. 6.7(b)). HRTEM investigations also show that dislocations generated in Pd films hydrided to β-phase interact and accumulate on ∑3{111} CTBs causing a clear loss of coherency of these boundaries. Interestingly, this result also demonstrates that ∑3{111} CTBs can be used as markers for qualitative evaluation of hydrogen enhanced dislocation activity in twinned nc metallic thin films or bulk systems.

Moreover, Σ3{112} ITBs have been observed to dissociate into two phase boundaries bounding a new and unstable 9R phase in Pd film hydrided to β-phase. The driving force of such a phenomenon can be attributed to the high compressive internal stress building-up during hydriding to β-phase as well as the decrease of the SFE of Pd in the presence of hydrogen which can reduce the critical resolved shear stress required for the activation of the dissociation process. However, since these two factors are operating simultaneously during hydriding, it is not possible at present to separate their effects or determine their relative importance. Nevertheless, the observations of lattice dissociated dislocations and faulted loops in Pd films hydrided to β-phase (Fig. 6.10) provide direct experimental evidence on the effect of hydrogen on the SFE of Pd.

Such behavior should be discussed based on the GPFE theory. Indeed, both simulation and experimental works in the literature have confirmed that the entire GPFE curve must be taken into consideration to describe the observed dislocation activity in nc materials [44]. Specifically, after a leading partial generates a SF, the nucleation and gliding barrier for the trailing partial is a function of the ratio of the unstable SFE (γ_{usf}) and intrinsic SFE (γ_{isf}). If this ratio is close to unity, full dislocations are favoured. Conversely, if this ratio is high, extended partial dislocations and SFs are expected within the nc grains. Furthermore, if the

ratio of the unstable twin fault energy (γ_{utf}) and unstable SFE ($\gamma_{utf}/\gamma_{usf}$) is low, then a twinning partial can form converting a pre-existing single SF to a twin nucleus. In the literature, the calculated GPFE curve in Pd shows that $\gamma_{usf}/\gamma_{isf}$ is close to 1.5 [44], meaning that only full dislocations are expected instead of SFs, in agreement with the observation of full lattice dislocations in HRTEM images obtained in both as-deposited (Fig. 6.6(b)) and deformed nc Pd thin films in the literature [58]. Also, since the unstable twin fault energy is not much higher than the unstable SFE ($\gamma_{utf}/\gamma_{usf}$ ~1.3 [44]), once a leading partial is emitted, it becomes possible to produce twins in nc Pd despite its high intrinsic SFE. For comparison, calculations of GPFE in Ni in the literature [44] have shown that $\gamma_{usf}/\gamma_{isf}$ is large (1.94) while $\gamma_{utf}/\gamma_{usf}$ is low (1.25), in agreement with the observation of SFs and twins in nc Ni using both MD simulations and experiments despite its high γ_{isf} [215,216].

In the present study, the observation of a high density of Shockley partial faulted loops (Fig. 6.10(b)) after hydriding to β-phase confirms that only the leading partial loops are nucleated. This demonstrates that γ_{usf} has increased under hydrogen loading, leading to a higher energy barrier for the formation of trailing partial loops. Such behaviour can be further enhanced by the decrease of γ_{isf} after hydriding to β-phase which is confirmed based on the observation of narrowly dissociated lattice dislocations in the interior of the grains (Fig. 6.10(c)). The decrease of γ_{isf} during hydriding to β-phase can be quantified based on the measurement of the equilibrium distance "d" separating the dissociated partials in Fig. 6.10(c) using the following equation [217]:

$$\gamma = \frac{Gb^2}{8\pi d}\frac{2-\upsilon}{1-\upsilon}\left(1 - \frac{2\upsilon}{2-\upsilon}\cos 2\beta\right) \tag{6.1}$$

where γ is the intrinsic SFE, G the shear modulus, υ the Poisson's ratio, **b** the Burgers vector of the partials, β the character the dissociated dislocation and d the splitting width of the partials. In Fig. 6.10(c), the equilibrium distance d is equal to 2.5 nm leading to γ_{isf} = 50.2 mJ/m^2 indicating that γ_{isf} has decreased during hydriding to β-phase by 60-70%. It should be noted here that the sole decrease of γ_{isf} can only provide a way to vary the dislocation splitting distance and dislocation nucleation barriers and thus cannot explain the observation of leading Shockley partial faulted loops without trailing loops. Very Recently, Tang et al.

[212] have shown using atomistic simulations in Ni that γ_{isf} decreases with increasing hydrogen concentration due to the resulting negative binding energy of hydrogen to the SF, while the unstable SFE increases with increasing hydrogen concentration in agreement with the present experimental work. On the other hand, the observation of extrinsic SFs (Fig. 6.10(d)) is in perfect agreement with the intrinsically low value of the $\gamma_{utf}/\gamma_{usf}$ ratio in Pd [44] which can be further lowered due to the increase of γ_{usf} and the decrease of γ_{utf} in the presence of hydrogen.

Figure 6.12 shows a schematic illustration of the effect of hydrogen on the GPFE curves in Pd during hydriding to β-phase, based on the elementary defect mechanisms revealed in the present study (Fig. 6.11).
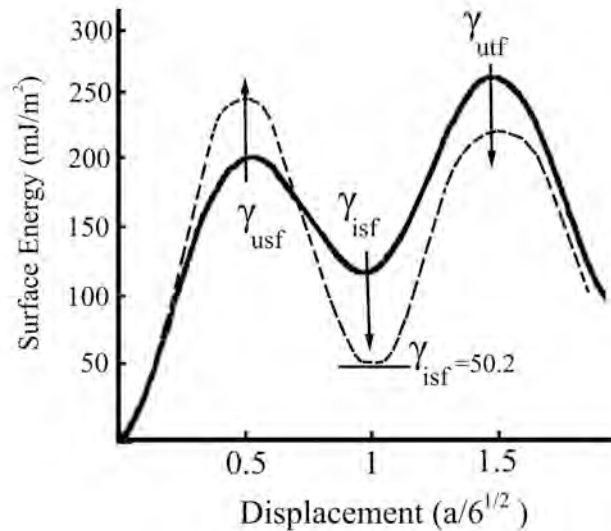
Figure 6.12 Schematic illustration of generalized SFE of Pd (solid lines) which is obtained from ref. [44] and GSFE curve for Pd after hydriding /dehydriding to β-phase (dashed lines).

It is important to note here that the changes of the GPFE curves in Pd during hydriding to β-phase should be coupled to the internal stress building up in order to explain the formation of SFs. Also, the differences of the size and the type of SFs (i.e., intrinsic or extrinsic SFs) may originate from (1) variations of the internal stress within a single grain in the presence of β hydrides or from one grain to another due to local stress concentrations originating from microstructure heterogeneities such as differences in grain size/orientation and the presence of growth twins; (2) a non-homogenous distribution of hydrogen within the matrix during hydriding.

Another factor which can influence the nucleation of SFs in nc metals is the structure of GBs. In the literature, 60° lattice dissociated dislocations in nc Ni have been observed in the vicinity of high energy non-equilibrium GBs where high stress concentrations near these boundaries help to overcome the energy barriers for the nucleation of SPDs in spite of the high SFE of Ni [66]. Such behavior can be excluded in the present study since only perfect dislocations originating from the deposition process have been observed close to GBs in as-sputtered nc Pd films while dissociated dislocations and SFs have been systematically observed in the interior of the grains or connected to GBs after hydridng to β-phase. The presence of Shockley partial faulted loops is also an intriguing point, which requires extra discussion.

Indeed, Shockley partial faulted loops have been rarely observed in nc materials because of the lack of Frank-Read sources within the small grains. In the present work, the origin of such behavior can be attributed to β nanohydrides that can act as favorite sites for the nucleation of Shockley partial faulted loops. The loops can thus play a role of debris, which can be used for statistical analysis of the distribution of β nanohydride formation in the nc grains. The stability of SFs in the FIB thin foils after releasing the hydrogen also raises questions regarding dislocation/hydrogen interactions. Indeed, when the hydrogen is released at the end of the hydriding cycle, the intrinsic SFE should evolve towards its initial value leading to the reversible contraction of the SFs, especially for the small faulted loops which are highly unstable because of the high attractive forces acting between segments with opposite Burgers vectors.

Recent atomistic simulations on the dislocation/hydrogen interaction in fcc metals have shown that, on the dislocation glide plane, only hydrogen atoms in the Shockley partial core regions can result in increasing the SF width, while those in the SF region or in the perfect fcc lattice region have no observable effects [212]. Furthermore, using multi-scale atomistic simulations, Pezold et al. have recently shown, that, depending on the hydrogen–hydrogen interaction strength, local hydrides which generally form at elevated pressures are thermodynamically stable at ambient conditions in the tensile strain field of dislocations even in the presence of extremely dilute bulk hydrogen distributions [213]. It can thus be expected that the observation of SFs in dehydraded nc Pd films used in the present study is due to the presence of thermodynamically stable nanohydrides trapped at the SPDs core. This is also in agreement with the observed stability of the SFs under the electron beam indicating high Pd-H interactions at the core of the SPDs. The presence of such a nanohydride at the partials

forming the boundaries of the 9R phase can also explain the stability of this phase after dehydriding.

It worth noting that direct observation of stable nanohydrides pinned at the lattice dislocation cores or at GBs using HRTEM was impossible because of the very low phase contrast of hydrogen atoms as well as the generic strain field associated to the defects. It was also impossible to extract a hydrogen or Pd-hydrogen signal from EELS measurements on the defects (Fig. 6.13). Therefore, in the present study, the presence of such thermodynamically stable nanohydrides at the SPDs core after dehydriding has been excluded based on spatially resolved EELS measurements. The stability of glissile intrinsic SF loops in nc Pd films after dehydriding can thus be attributed to the presence of important internal stress heterogeneities typical of nc materials.
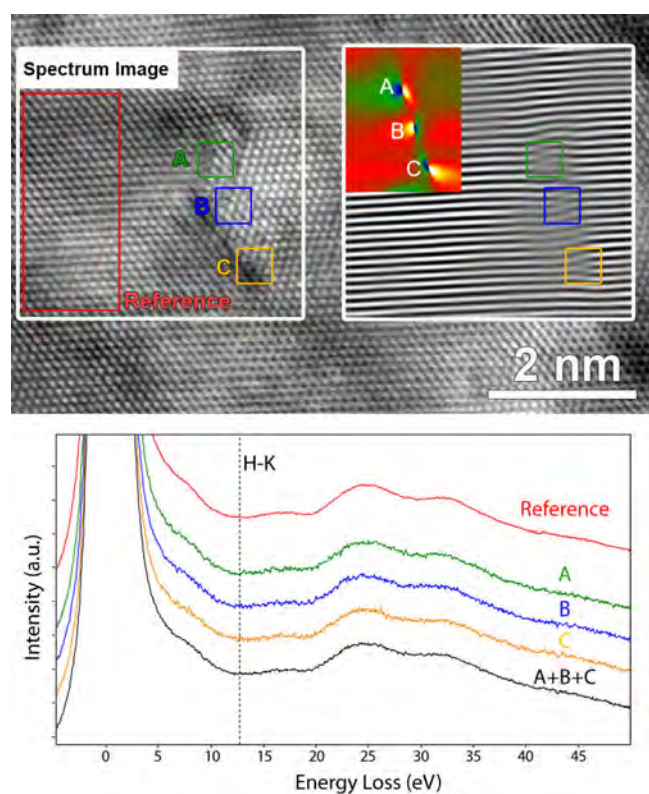
Figure 6.13 Electron energy loss spectroscopy measurement on the dislocation cores in the Pd films hydrided to β-phase.

The Pd films have been also examined using ACOM-TEM before and after hydriding to β-phase (Fig. 6.4). The results did not show significant changes of the grain size or the crystallographic texture indicating that GB mechanisms are not dominating the local plasticity during the hydriding process. Hydriding induced twinning can also be excluded since

HRTEM observations after hydriding to β-phase only revealed a high density of intrinsic and extrinsic SFs while a clear increase of twin density was not observed. The absence of intense twinning after hydriding indicates that the compressive internal stress building up during hydrogen loading was not sufficient to ensure the growth of hydrogen induced twins via TB migration. On the other hand, the loss of coherency of growth ∑3{111} CTBs due to dislocations/CTB interactions after hydriding to β-phase may result in strong interactions of hydrogen with these boundaries. Similar behavior can thus be expected for random GBs acting as strong obstacles for lattice dislocations. Furthermore, the presence of an unstable 9R phase at dissociated growth∑3{112} ITBs indicates that GBs can act as favorite sites for the emission of partial dislocations under hydriding.

Finally, all these results indicate that the mechanical properties of nc Pd thin films after hydriding may strongly differ from those of as-deposited films. On the one hand, because of the high density of SFs present within the nanograins after dehydriding, deformation twinning can be expected when the system is subjected to an external applied stress. Indeed, the presence of both intrinsic and extrinsic SFs allows overcoming the energy barriers for the nucleation of a twin. Once the twin nucleus is formed, the twin can easily grow under an external applied stress. Using atomistic simulations Stukowski et al. have recently shown that TB migration is energetically favored over the formation of SFs or full lattice dislocations in deformed nc Pd with pre-existing twins [218]. In the present study, two distinct microscopic deformation mechanisms can be envisaged in nc Pd films after hydriding. The first is strengthening controlled by the interaction of full lattice dislocations [58] with SFs induced by hydriding while the second is softening dominated by TB migration involving the nucleation and the glide of twinning dislocations at the vicinity of hydrogen induced intrinsic and extrinsic SFs.

6.2.5. Conclusions

The nanoscale plasticity mechanisms activated during hydriding in sputtered nc Pd films with growth TBs and subjected to hydriding cycles to induce both α- and β-phase transformations have been investigated ex-situ before and after hydriding using advanced TEM. The results can be summarized as follows:

- In Pd films hydrided to β-phase, local plasticity was mainly controlled by dislocation activity in spite of the small grain size. GB mediated processes were excluded as

dominant mechanisms based on the averaged ACOM-TEM data performed ex-situ. In contrast, significant microstructural changes were not observed in Pd films hydrided to α-phase.

- Intrinsic SFs as well as extrinsic SFs have been observed after hydriding to β-phase indicating that the energy barriers for the nucleation of the trailing (twinning) partials have been increased (decreased) in the presence of hydrogen. The stable SFE has also decreased by 60-70% after hydriding to β-phase.

- Growth Σ3{111} CTBs can be used as markers for qualitative evaluation of the level of plastic deformation developed in individual nanograins (i.e., loss of coherency due to the interaction with lattice dislocations) while growth Σ3{112} ITBs can be used to evaluate the effect of hydrogen on the SFE (i.e., dissociation of ITBs into 9R phase boundaries) in hydrided nc Pd films.

- Shear type faulted loops rarely reported in nc materials have probably been nucleated from β nanohydride within the Pd grains after hydriding to β-phase. These loops could possibly be used for HRTEM statistical analysis on the distribution of the nanohydrides within the nanograins.

- The observed stability of SFs and 9R phase in the FIB thin foils after dehydriding is attributed to the pinning of the partials bounding these defects by lattice dislocations or the presence of stress heterogeneities in the small grains, typical of nc materials.

These results predict an important contribution of SFs and deformation twinning on the mechanical behavior of nc Pd films hydrided to β-phase when subjected to an external applied stress. Changes of intergranular plasticity mechanisms cannot be excluded because of local changes of the structure of GBs during hydrogen loading similarly to the changes of growth TBs observed experimentally in the present study. However, different scenarios for the mechanical response can be envisaged depending on the nature, the competition or the synergy of the activated mechanisms.

7. Summary and perspectives

In the present thesis, crystal defects such as growth twins, dislocations, grain boundaries etc. in nanocrystalline Pd thin films were investigated in depth using advanced TEM techniques in order to uncover the fundamental processes governing the formation of these defects as well as their transformation and interaction with other defects under controlled mechanical and hydrogen loading modes yielding nanoplasticity mechanisms in Pd films.

First the effect of deposition rate in a wide range of 0.3 to 5 Å.s^{-1} on the microstructure changes of thin Pd films has been investigated by various TEM methods. The deposition of the films was performed by the IMAP group of the Université Catholique de Louvan-la-neuve using electron beam deposition. Results showed that all films reveal a columnar nanograin configuration containing nanoscale growth twins. Twin boundary density and volume fraction of grains containing twins increase with increasing deposition rate. A clear increase of the dislocation density was also observed for the highest deposition rate (5 Å.s^{-1}) which is related to larger internal stresses at high deposition rates (5 Å/s). It was also shown that, for the lowest deposition rates (0.3 and 1 Å/s), most of the twin boundaries are fully coherent without any residual dislocations. For the highest deposition rate (5 Å/s), the coherency of the twin boundaries decreased significantly due to dislocation/twin interactions. This result corresponds with the increase of the lattice dislocation density in the films with higher deposition rate. The fraction of high angle grain boundaries in the range of 55-65°continuously increases with increasing deposition rate, which again correlates with the increasing twin boundary density.

Next, time-resolved high resolution TEM relaxation experiments of electron beam deposited Pd films using an on-chip tensile testing method, developed at IMPA, have been performed. Based on the results obtained in the previous section, the optimized processing parameters (e.g., deposition rate 1 Å/s) were used for deposition of the nanocrystalline Pd films. Despite the small 30 nm grain size, the relaxation mechanism responsible for the unexpected large creep rates measured at room temperature is found to be mediated by the stress driven nucleation and propagation of dislocations. The dislocations interact with the growth nanotwins present in the grains, leading to a loss of coherency of the twin boundaries. The density of stored dislocations first markedly increases with applied deformation, then decreases with time to drive additional deformation while no grain boundary mechanisms are observed based on the averaged ACOM-TEM data. The impact of this fast relaxation can

constitute a key issue in the development of a variety of micro- and nanotechnologies, such as Pd membranes used in hydrogen applications.

In this respect, the effect of initial microstructure on the hydriding mechanisms of the nanocrystalline Pd films has then been investigated. Due to the effect of the internal stress on the hydriding behavior, Pd films were deposited by magnetron sputtering in order to finely control the growth internal stress. The microstructure of the sputtered Pd films was controlled by annealing for 20 min at 300°C in order to eliminate part of the defects massively generated by room temperature magnetron sputtering deposition. The hydriding results showed that the as-deposited specimen exhibits a faster hydriding kinetics than the annealed specimen. This behavior is attributed to a low defect density for twin boundaries, dislocations and grain boundaries in the annealed Pd films which can act as trapping sites and pathways of hydrogen atoms.

The effect of hydriding ($\alpha\leftrightarrow\beta$ phase transformation) on the microstructure changes of nanocrystalline Pd films was also investigated. The results show that volume changes of β-phase during hydriding induce internal stress which is higher than the yield stress of the film. This leads to an increase of dislocation density stored within the nanograins. No grain growth was observed after hydriding. It is also demonstrated that the {111} nanoscale growth twins lose their coherency. Surprisingly, the$\sum3${112} incoherent twin boundaries largely dissociate after hydriding into two-phase boundaries bounding a new and thermodynamically unstable 9R phase. The nanoscale plasticity mechanisms activated during hydriding/dehydriding cycle in sputtered nanocrystalline Pd films with growth twin boundaries have also been investigated ex-situ before and after hydriding. The results showed that in Pd films hydrided to β-phase, local plasticity was mainly controlled by dislocation activity in spite of the small grain size. Grain boundary mediated processes were not observed as dominant mechanisms. Also, significant microstructural changes were not observed in Pd films hydrided to α-phase. Intrinsic stacking faults as well as extrinsic stacking faults have been observed after hydriding to β-phase indicating that the energy barriers for the nucleation of the trailing (twinning) partials have been increased (decreased) in the presence of hydrogen. The stable stacking fault energy has also decreased by 60-70% after hydriding to β-phase. The observed stability of stacking faults and 9R phase in the focused ion beam thin foils after dehydriding is attributed to the pinning of the partials bounding these defects by lattice dislocations or the presence of stress heterogeneities in the small grains, typical of nc materials. These results predict an

important contribution of stacking faults and deformation twinning on the mechanical behavior of nc Pd films hydrided to β-phase when subjected to an external applied stress.

Based on the above results, four different interesting perspectives can be suggested:

- Understanding the mechanical properties of the nc Pd films, transitions of the mechanical response related to changes of sample dimensions or microstructures and of the elementary plasticity mechanisms (inverse Hall-Petch, interface dominated mechanics, brittle-ductile transition, rate dependent behaviour, etc.).

- The role of the irreversible microstructural changes induced under hydrogen cycling on the mechanical behaviour. For the coupling between the fundamental mechanisms operating at the nanoscale and the macroscopic (thermo-)mechanical behaviour, the ACOM-TEM technique combined with quantified in-situ TEM nano/micromechanical testing including in-situ heating.

- Thermally activated mechanisms in a large range of operating strain rates and temperatures in both as-deposited and hydrided Pd systems using quantified in-situ TEM nano/micromechanical holder.

- The study of elementary processes controlling the fracture of as-deposited and hydrided nc Pd systems such as the interactions between GBs and the atomistic cracking mechanisms.

Samenvatting en perspectieven

In dit proefschrift worden kristaldefecten zoals groeitweelingen, dislocaties, korrelgrenzen, enz. in nanokristallijne Pd dunne films grondig onderzocht met behulp van gevorderde TEM technieken. Hiermee worden de fundamentele processen van de vorming van defecten onderzocht evenals hun transformatie en interactie met andere defecten onder gecontroleerde mechanische belasting en hydratatie (toevoeging van waterstof) in het licht van nanoplasticiteitsmechanismen in Pd dunne films.

Eerst werd het effect van de depositiesnelheid op de microstructuur van de dunne Pd films onderzocht. De afzetting van de films werd uitgevoerd door de IMAP-groep van de Université Catholique de Louvain-la-Neuve m.b.v. elektronenbundel geassisteerde afzetting. De resultaten tonen aan dat alle films een kolomstructuur vertonen met groeitweelingen op de nanoschaal. De tweelinggrensdichtheid en volumefractie van korrels met een tweeling verhoogt met toenemende afzettingssnelheid. Een duidelijke toename van de dislocatiedichtheid werd ook waargenomen voor de hoogste afzettingssnelheid, wat gekoppeld kan worden aan grotere inwendige spanningen bij deze hoge afzettingssnelheden. Ook werd aangetoond dat bij de laagste depositiesnelheid de meeste van de tweelinggrenzen volledig coherent zijn zonder resterende dislocaties. Voor de hoogste depositiesnelheid blijkt de coherentie van de tweelinggrenzen aanzienlijk gedaald als gevolg van dislocatie / tweeling interacties. Dit resultaat stemt overeen met de toename van de dislocatiedichtheid in de matrix van de korrels in de films geproduceerd met een hogere depositiesnelheid. De fractie van grote-hoek korrelgrenzen in het bereik van 55-65° neemt continu toe met toenemende afzettingssnelheid, wat opnieuw in verband kan gebracht worden met de toenemende dichtheid van tweelinggrenzen.

Vervolgens werden tijdsafhankelijke opnamen met hoge resolutie TEM uitgevoerd van Pd films afkomstig van de *on-chip* treksterkte testmethode ontwikkeld in IMAP. Op basis van de resultaten uit de vorige paragraaf werden de optimale procesparameters (bv. afzettingssnelheid) van de nanokristallijne Pd films gebruikt. Ondanks de kleine korrelgrootte (~30 nm) werd een relaxatiemechanisme met onverwachte grote kruipsnelheden gemeten bij kamertemperatuur. Dit bleek te zijn geïnitieerd door de stress aangedreven nucleatie en vermeerdering van dislocaties. De interactie van de dislocaties met de groei nanotweelingen aanwezig in de korrels, leidt tot een verlies van coherentie van deze tweelinggrenzen. De dichtheid van de opgeslagen dislocaties verhoogt eerst aanzienlijk met toenemende

vervorming, daarna neemt ze af met de tijd. Op basis van gemiddelde ACOM-TEM data werden geen aanwijzigingen gevonden voor korrelgrens gekoppelde mechanismen. De impact van deze snelle ontspanning kan een belangrijk punt zijn in de ontwikkeling van een verscheidenheid aan micro- en nanotechnologieën, zoals Pd membranen gebruikt in toepassingen voor waterstoftechnologie.

Hierna werd het effect van de initiële microstructuur op de hydratatiemechanismen van de nanokristallijne Pd films onderzocht. In dit geval werden de films gedeponeerd m.b.v. magnetron sputtering om zo beter de inwendige spanningen te kunnen controleren. De microstructuur van de gesputterde Pd films werd geoptimaliseerd door uitgloeien gedurende 20 minuten bij 300 °C om een deel van de defecten, gegenereerd door de afzetting op kamertemperatuur in de magnetron sputtering, te elimineren. De resultaten na hydratatie toonden aan dat het onbehandelde specimen een snellere hydratatie kinetiek vertoont dan het gegloeide monster. Dit verschil wordt toegeschreven aan een lagere dichtheid van defecten zoals tweelinggrenzen, dislocaties en korrelgrenzen in de uitgegloeide Pd films en die kunnen fungeren als opvangplaatsen en diffusieroutes van waterstofatomen.

Het effect van hydratatie ($\alpha \leftrightarrow \beta$ faseovergang) op de veranderingen in microstructuur van nanokristallijne Pd films werd eveneens onderzocht. De resultaten tonen aan dat volumeveranderingen van β-fase tijdens hydratatie inwendige spanningen induceren die hoger zijn dan de vloeispanning van de film. Dit leidt tot een toename van de dislocatiedichtheid opgeslagen in de nanokorrels. Geen korrelgroei werd waargenomen na hydratatie. Het is ook aangetoond dat de {111} nanoschaal groeitweelingen hun coherentie verliezen. Verrassend is dat de $\Sigma 3$ {112} incoherente tweelinggrenzen grotendeels opgesplitst geraken in twee fasegrenzen die een nieuwe en thermodynamisch instabiele 9R fase begrenzen na hydratatie. De nanoschaal plasticiteitsmechanismen geactiveerd tijdens hydratatie / dehydratatie cycli in gesputterde nanokristallijne Pd films werden ook onderzocht ex situ vóór en na hydratatie. De resultaten toonden aan dat in Pd films gehydrateerd tot aan de β-fase lokale plasticiteit voornamelijk werd bepaald door dislocatieactiviteit ondanks de kleine korrelgrootte. Korrelgrens gemedieerde processen werden niet waargenomen als dominante mechanismen. Ook werden geen significante microstructurele veranderingen waargenomen in Pd films gehydrateerd tot α-fase. Intrinsieke en extrinsieke stapelfouten waargenomen na hydratatie tot β-fase geven aan dat de energiebarrières voor de kiemvorming van de achterlopende/tweeling partiële dislocaties zijn verhoogd/verlaagd in aanwezigheid van waterstof. De stabiele stapelfoutenergie is eveneens afgenomen met 60-70% na hydratatie tot de β-fase. De

waargenomen stabiliteit van stapelfouten en 9R fase in de gefocusseerde ionenbundel dunne folies na hydratatie wordt toegeschreven aan de pinning van de partiële begrenzende dislocaties door rooster dislocaties of de aanwezigheid van stress heterogeniteiten in de kleine korrels, typisch voor nc materialen. Deze resultaten voorspellen een belangrijke bijdrage van stapelfouten en vervormingstweelingen op het mechanische gedrag van nc Pd films gehydrateerd tot de β-fase bij onderwerping aan een extern aangelegde spanning.

Op basis van deze resultaten kunnen vier verschillende interessante perspectieven worden voorgesteld:

• Studie van de effecten van de dimensies van het monster of van de microstructuren op de mechanische eigenschappen van de nc Pd films, overgangen van de mechanische respons en van de elementaire plasticiteitsmechanismen (inverse Hall-Petch, de grensvlak gedomineerde mechanica, overgang breekbaar-plooibaar gedrag, snelheidsafhankelijk gedrag, enz.).

• De rol van de onomkeerbare microstructureel geïnduceerde effecten als gevolg van de waterstof cycli op het mechanisch gedrag. Het gebruik van de ACOM-TEM techniek in combinatie met gekwantificeerde in-situ TEM nano / micromechanische testen zoals in situ verwarming, met het oog op de koppeling tussen de fundamentele mechanismen die werken op nanoschaal en de macroscopische (thermo) mechanische eigenschappen,

• Thermisch geactiveerde mechanismen in een groot scala van operationele reksnelheden en temperaturen in zowel gedeponeerde als gehydrateerde Pd systemen met behulp van de kwantificeerbare in-situ TEM nano / micromechanische houder.

• De studie van de elementaire processen die het breken van gedeponeerd en gehydrateerde nc Pd systemen controleren, zoals de interacties tussen korrelgrenzen en de atomaire mechanismen.

8. References

1. R. P. Jayaraman, Thin film hydrogen sensors: a materials processing approach, Ph.D thesis, The Pennsylvania State University, 2002, USA.

2. K. L. Salcedo, C. A. Rodríguez, F. A. Perez, H. Riascos, *J. Phys*. 2011, 274, 012120.

3. Fuel Cell Standards Committee. "Basic Consideration for safety of Hydrogen Systems" Technical Report ISO TC 197 N166, International Standards Organization, 2001.

4. E. Dillon, G. Jimenez, A. Davie, J. Bulak, S. Nesbit, A. Craft, *Mater. Sci. Eng. A*, 2009, 524,89.

5. A. C. Dillon, K. M. Jones, T. A. Bekkedahl, C. H. Kiang, D. S. Bethune, M. J. Heben *Nature*, 1997, 386, 377.

6. C. Zandonella, *Nature,* 2001, 410, 734.

7. Y. Ye, C. Ahn, C. Witham, B. Fultz, J. Lui, A. G. Rinzler, D. Colbert, K. A. Smith, R. E. Smalley, *Appl. Phys. Lett.*, 1999, 74, 2307.

8. A. Chambers, C. Park, R.T.K. Baker, N.M. Rodriguez, *J. Phys. Chem. B*, 1998, 102, 4253.

9. N. Rajalakshmi, K.S. Dhathathreyan, A. Govindaraj, B.C. Satishkumar, *Electrochem. Acta*, 2000, 45, 4511.

10. R. A. Zidan, S. Takara, A. Hee, C. M. Jensen, *J. Alloys Compd.*, 1999, 285, 119.

11. B. Bogdanovic, R. A. Brand, A. Marjanovic, M. Schwickardi, J. Tolle, *J. Alloys Compd.,* 2000, 302, 36.

12. C. M. Jensen, K. J. Gross, *Appl. Phys. A*, 2001, 72, 213.

13. B. Bogdanovic, M. Schwickardi, *Appl. Phys. A*, 2001, 72, 221.

14. K. J. Gross, G. J. Thomas, C. M. Jensen, *J. Alloys Compd.*, 2002, 330–332, 683.

15. G. A. Fateev, V. L. Tarasevich, V. Stanek, P. Vychodil, *J. Eng. Phys. Thermophys.*, 1989, 57, 811.

16. F. E. Lynch, *J. Less Common Metals*, 1991, 172–174, 943–958.

17. A.Y. Esayed, *Energy Sources*, 2001, 23, 257.

18. S. A. Gadre, *Ind. Eng. Chem. Res.*, 2003, 2, 1713.

19. J. M. Wheeler, T. W. Clyne, *Int. J. Hydrogen Energy,* 2012*, 37, 14315.*

20. G. Jimenez, E. Dillon, R. Miller, F. Massicotte, S. Nesbitd, A. Craft, *Scr. Mater.* 2008, 59, 870.

21. A. Othonos, K. Kalli, D. P. Tsai, *Appl. Surf. Sci.*, 2000, 161, 54.

22. B. D. Adams, A. Chen, *Mater. Today*, 2011, 14, 282.

23. R. Delmelle, G. Bamba, J. Proost, *Int. J. Hydrogen energy*, 2010, 35, 9888.

24. A. Maeland, T. B. Flanagan, *Platinum Met. Rev.*, 10, 1966, 20.

25. M. V. Goltsova, G. I. Zhirov, *Met. Sci. Heat Treat.*, 2007, 49, 141.

26. T. Yokosawa, T. Alan, G. Pandraud, B. Dam, H. Zandbergen, *Ultramicroscopy* 2012, 112, 47.

27. M. S. Colla, Plasticity and creep in thin free-standing nanocrystalline Pd films, Louvain-la-Neuve, Ph.D thesis, 2013, Belgium.

28. Y. Li, Y. T. Cheng. *Int. J. Hydrogen Energy*, 1996, 21, 281.

29. A. Pundt, R. Kirchheim, *Ann. Rev. Mater. Res.,* 2006, 36, 555.

30. R. Delmelle, Effect of internal stress and microstructure on the hydriding of Pd thin films, Louvain-la-Neuve, PhD thesis, 2012, Belgium.

31. H. Ren, X. Yang, Y. Gao, T. Y. Zhang. *Acta Mater.*, 2013, 61, 5487.

32. F. Favier, E. C. Walter, M. P. Zach, T. Benter, R. M. Penner, *Science,* 2001, 293, 2227.

33. J. Carpena-Nunez, D. Yang, J. W. Kim, C. Park, L. F. Fonsec, *Nanotech.* 2013, 24, 035701.

34. L. L. Jewell, B. H. Davis. *Appl. Catal. A: General*, 2006, 310,1.

35. G. Alefeld, J. Volkl. *Springer Verlag*, 1978, 978, 231.

36. D. Stolten, Hydrogen and Fuel Cells: Fundamentals, Technologies and Applications, John Wiley & Sons, 2010.

37. E. Wicke, H. Brodowsky, *Hydrogen in Metals*, 1978, 2, 73.

38. T. Mutschele, R. Kirchheim, *Scr. Metal.*, 1987, 21, 135.

39. D. Hull, D. J. Bacon, Introduction to dislocations, Fifth edition, Elsevier Ltd..

40. R. Kirchheim, *Acta Metall.* 1981, 29, 835.

41. N. Mommer, M. Hirscher, F. Cuevas, H. Kronm-uller, J. alloys Compd. 1998, 266, 255.

42. M. Koyama, E. Akiyama, T. Sawaguchi, D. Raabe, K. Tsuzaki, *Scr. Mater.,* 2012, 66, 459.

43. M. Danaie, S. Tao, P. Kalisvaart, D. Mitlin, *Acta Mater.* 2010, 58, 3162.

44. Z. H. Jin, S.T. Dunham, H. Gleiter, H. Hahnb, P. Gumbsch, *Scr. Mater.* 2011, 64, 605.

45. Y. T. Zhu, X. Z. Liao, X. L. Wu, Progress Mater. Sci., 2012, 57, 1.

46. H. Van Swygenhoven, P. M. Derlet, A. G. Froseth, *Nature Mater.* 2004, 3, 399.

47. R. J. Asaro, S. Suresh, *Acta Mater.* 2005, 53, 3369.

48. Y. T. Zhu, X. Z. Liao, X. L. Wu. *JOM,* 2008, 60, 60.

49. D. Farkas, E. Bringa, A. Caro, *Phys. Rev. B.,* 2007, 75, 184111.

50. L. Lu, Y. Shen, X. Chen, L. Qian, K. Lu, *Science*, 2004, 304, 422.

51. K. Lu, L. Lu, S. Suresh, *Science*, 2009, 324, 349.

52. L. Lu, X. Chen, X. Huang, K. Lu, *Science*, 2009, 323, 607.

53. X. Zhang, H. Wang, X. H. Chen, L. Lu, K. Lu, R. G. Hoagland, A. Misra, *Appl. Phys. Lett.* 2006, 88, 173116.

54. X. Zhang, A. Misra, H. Wang, M. Nastasi, J. D. Embury, T. E. Mitchell, R. G. Hoagland, *Appl. Phys. Lett.* 2004, 84, 1096.

55. X. Zhang, A. Misra, H. Wang, T. D. Shen, M. Nastasi, T. E. Mitchell, J. P. Hirth, R. G. Hoagland, J. D. Embury, *Acta Mater.,* 2004, 52, 995.

56. X. Zhang, A. Misra, H. Wang, A. L. Lima, M. F. Hundley, R. G. Hoagland, *J. Appl. Phys.*, 2005, 97, 094302.

57. X. Zhang, O. Anderoglu, A. Misra, H. Wang, *Appl. Phys. Lett.*, 2007, 90, 153101.

58. H. Idrissi, B. Wang, M. S. Colla, J. P. Raskin, D. Schryvers, T. Pardoen, *Adv. Mater.*, 2011, 23, 2119.

59. B. Wang, H. Idrissi, H. Shi, M. S. Colla, S. Michotte, J. P. Raskin, T. Pardoen, D. Schryvers, *Scr. Mater.* 2012, 66, 866.

60. M. F. Ashby, E. Harper, Harvard Rept. Sept. Cambridge, MA: Harvard Univ, 1967.

61. H. Gleiter, in: J.W. Christian, P. Haasen, T.B. Massalski (Eds.), Progress in Materials Science, Chalmers Anniversary Volume, Pergamon Press, Oxford, 1981.

62. R. L. Fullman, J. C. Fisher. *J. Appl. Phys.* 1951, 22, 1350.

63. Y. B. Wang, M. L. Sui, E. Ma, *Philos. Mag. Lett.* 2007, 87, 935.

64. X. L. Wu, X. Z. Liao, S. G. Srinivasan, F. Zhou, E. J. Lavernia, R. Z. Valiev ,Y. T. Zhu, *Phys. Rev. Lett.*, 2008, 100, 095701.

65. X. Z. Liao, F. Zhou, E. J. Lavernia, S. G. Srinivasan, M. I. Baskes, D. W. He, Y. T. Zhu, *Appl. Phys. Lett.,* 2003, 83, 632.

66. X. Wu, Y. T. Zhu, *Appl. Phys. Lett.* 2006, 89, 031922.

67. X. L. Wu, J. Narayan, Y. T. Zhu. *Appl. Phys. Lett.* 2008, **93**, 031910.

68. Y. T. Zhu, X. Z. Liao, R. Z. Valiev, *Appl. Phys. Lett.,* 2005, 86, 103112.

69. M. S. Colla, B. Wang, H. Idrissi, D. Schryvers, J. P. Raskin, T. Pardoen, *Acta Mater.,* 2012, 60, 1795.

70. D. Fabregue, N. Andre, M. Coulombier, J. P. Raskin, *Micro. Nanolett.,* 2007, 2 , 13.

71. N. Andre´, M. Coulombier, V. De Longueville, D. Fabregue, T. Gets, S. Gravier, T. Pardoen, J. P. Raskin, *Microelectron. Eng.,* 2007, 84, 2714.

72. U. K. Bhaskar, V. Passi, S. Houri, E. Escobedo-Cousin, S. H. Olsen, T. Pardoen, J. P. Raskin, *Rev. Sci. Inst.,* 2012, 27, 571.

73. G. A. Malygin, *Phys. Solid State*, 2007, 49, 1013.

74. A. V. Sergeeva, V. V. Stolyarov, R. Z. Valiev, A. K. Mukhergee, *Scr. Mater.,* 2000, 43, 819.

75. M. A. Meyers, A. Mishra, D. J. Benson. *Progress in Materials Science,* 2006, 51, 427.

76. X. L. Wu, E. Ma. *Appl. Phys. Lett.*, 2006, 88, 231911.

77. J. Lohmiller, M. Grewer, C. Braun, A. Kobler, C. Kubel, K. Schuler, V. Honkimaki, H. Hahn, O. Kraft, R. Birringer, P. A. Gruber. *Acta Mater.*, 2014, 65, 295.

78. X. Z. Liao, S. G. Srinivasan, Y. H. Zhao, M. I. Baskes, Y. T. Zhu, F. Zhou, E. J. Lavernia, H. F. Xu. *Appl. Phys. Lett.* 2004, 84, 3564.

79. V. Yamakov, D. Wolf, M. Salazar, S.R. Phillpot, H. Gleiter.. *Acta Mater.*, 2001, 49, 2713.

80. N. I. Noskova, E. G. Volkova, *Phys. Met. Metalloved.*, 2001, 91, 629.

81. F. D. Schiotz, T. Vergge, F. D. Di Tolla, K. W. Jacobsen, *Phys. Rev. B: Condens. Matter*, 1999, 60, 11971.

82. H. van Swygenhoven, M. Spaczer, A. Caro, D. Farkas, *Phys. Rev. B: Condens. Matter*, 1999, 60, 22.

83. H. van Swygenhoven, D. Farkas, A. Caro, *Phys. Rev. B: Condens. Matter*, 2000, 62, 831.

84. V. Yamakov, D. Wolf, S. R. Phillpot, A. K. Mukherjee, H. Gleiter, *Nature Mater.*, 2004, 3, 43.

85. J. Schiotz, K. W. Jacobsen, *Science,* 2003, 301, 1357.

86. H. V. Swygenhoven, P. M. Derlet, A. G. Froseth, *Nature Mater.,* 2004, 3, 399.

87. Y. T. Zhu, X. Z. Liao, X. L. Wu. *Progress in Materials Science*, 2012, 57, 1.

88. J. W. Christian, S. Mahajan. *Progress in Materials Science*, 195, 39:1.

89. Z.-H. Jin, P. Gumbsch, E. Ma, K. Albe, K. Lu, H. Hahn, H. Gleiter. *Scripta Mater.* 2006, 54, 1163.

90. Z.-H. Jin, P. Gumbsch, K. Albe, E. Ma, K. Lu, H. Gleiter, H. Hahn. *Acta Mater.*2008, 56, 1126.

91. Y. M. Wang, F. Sansoz, T. LaGrange, R. T. Ott, J. Marian, T. W. Barbee, A. V. Hamza. *Nat Mater*, 2013, 12, 697.

92. T. Zhu, J. Li, A. Samanta, H. G. Kim, S. Suresh. *Proc. Natl. Acad. Sci.* 2007, 104, 3031.

93. A. Kobler, J. Lohmiller, J. Schäfer, M. Kerber, A. Castrup, A. Kashiwar, P. A. Gruber, K. Albe, H. Hahn, C. Kübel, *Beilstein J. Nanotechnol.* 2013, 4, 554.

94. R. C. Hugo, H. Kung, J. R. Weertman, R. Mitra, J. A. Knapp, D. Follstaedt, *Acta Mater.*, 2003, 51, 1937.

95. K. S. Kumar, S. Suresh, M. F. Chisholm, J. A. Horton, P. Wang, *Acta Mater.*, 2003, 51, 387.

96. I. M. Robertson, P. Ferreira, G. Dehm, R. Hull, *MRS Bull.*, 2008, 33, 122.

97. K. Hattar, J. H. Han, D. M. Follstaedt, S. J. Hearne, T. A. Saif, I. M. Robertson, *Mater. Res. Soc. Symp. Proc.*, 2006, 907.

98. K. Hattar, J. Han, M. T.A. Saif, I. M. Robertson, *J. Mater. Res.*, 2005, 20, 1869.

99. Y. B. Wang, B. Q. Li, M. L. Sui, *Appl. Phys. Lett.*, 2008, 92, 011903.

100. D. S. Gianola, S. Van Petegem, M. Legros, S. Brandstetter, H. Van Swygenhoven, K. J. Hemker, *Acta Mater.*, 2006, 54, 2253.

101. M. Legros, D. S. Gianola, K. J. Hemker, *Acta Mater.*, 2008, 56, 3380.

102. T. Gorkaya, D. A. Molodov, G. Gottstein, *Acta Mater.*, 2009, 57, 5396.

103. F. Mompiou, D. Caillard, M. Legros, *Acta Mater.*, 2009, 57, 2198.

104. H.C. Jamieson, G.C. Weatherly, F.D. Manchester, J. Less-Common Met, 1976, 50, 85.

105. M.V. Goltsova , Yu.A. Artemenko, V.I. Zaitsev, J. Alloys Compd, 1999, 293, 379.

106. J.M. Wheeler, T.W. Clyne, Int. J. Hydrogen Energy, 2012, 37, 14315.

107. E. Dillon, G. Jimeneza, A. Daviea, J. Bulaka, S. Nesbitb, A. Craft, Mater. Sci. Eng. A, 2009, 524, 89.

108. T. Rupert, D. Gianola, Y. Gan, K. Hemker, *Science*, 2009, 326, 1686.

109. F. Mompiou, M. Legros, A. Boe, M. Coulombier, J.-P. Raskin, T. Pardoen, *Acta Mater.*, 2013, 61, 205.

110. J. Schiotz, K. W. Jacobsen. *Science*, 2003, 301, 1357.

111. H. Conrad, J. Narayan, *Acta Mater.*, 2002, 50, 5067.

112. M. Ames, J. Markmann, R. Karos, A. Michels, A. Tschope, R. Birringer. *Acta Mater.*, 2008, 56, 4255.

113.   K. Zhang, J. R. Weertman, J. A. Eastman. *Appl. Phys. Lett.*, 2004, 85, 5197.

114.   D. S. Gianola, S. Van Petegem, M. Legros, S. Brandstetter, H. Van Swygenhoven, K. J. Hemker. *Acta Mater.*, 2006, 54, 2253.

115.   B. Zhu, R. J. Asaro, P. Krysl, K. Zhang, J.R. Weertman.. *Acta Mater.*, 2006, 54, 3307.

116.   A. J. Haslam, D. Moldovan, V. Yamakov, D. Wolf, S.R. Phillpot, H. Gleiter.. *Acta Mater.*, 2003, 51 2097.

117.   K. S. Kumar, H. Van Swygenhoven, S. Suresh, *Acta Mater.* 2003, 51, 5743.

118.   X. Zhang, H. Wang, R. O. Scattergood, J. Narayan, C. C. Koch, *Mater. Sci. Eng. A* 2003, 344,175.

119.   V. L. Tellkamp, A. Melmed, E. J. Lavernia, *Metall. Mater. Trans. A*, 2001, 32, 2335.

120.   F. Zhou, X. Z. Liao, Y. T. Zhu, S. Dallek, E. J. Lavernia, *Acta Mater.* 2003, 51, 2777.

121.   R. Z. Valiev, R. K. Islamgaliev, I. V. Alexandrov, *Prog. Mater. Sci.* 2000, 45, 103.

122.   H. Gleiter, *Prog. Mater. Sci.* 1989, 33, 223.

123.   P. G. Sanders, G. E. Fougere, L. J. Thompson, J. A. Eastman, J. R. Weertman, *Nanost. Mater.* 1997, 8, 243.

124.   P. G. Sanders, J. A. Eastman, J. R. Weertman, *Acta Mater.* 1997, 45, 4019.

125.   U. Erb, *Nanost. Mater.* 1995, 6, 533.

126.   A. M. El-Sharik, U. Erb, G. Palumbo, K. T. Aust. *Scr. Metall. Mater.* 1992, 27, 1185.

127.   F. Ebrahimi, Q. Zhai, D. Kong, *Scr. Mater.* 1998, 39, 315.

128.   M. Ohring, The materials science of thin films, Academic Press, 2002.

129.   D. B. Williams, C. B. Carter, Transmission Electron Microscopy A Textbook for Materials Science, Springer, third edition, 2009.

130.   E. Abbe, *J. R. Microsc. Soc.,* 1881, 1, 388.

131.   F. J. Humphreys, *Scr. Mater.* 2004, 51, 771.

132.   S. Zaefferer, *Ultramicroscopy* 2007, 107, 254.

133.   E. F. Rauch, M. Veron, *J. Mater. Sci. Eng. Tech.* 2005, 36, 552.

134.   C. A. Volkert, A. M. Minor, *MRS Bulletin* 2007, 32, 389.

135.   S. Yun, S.T. Oyama, *J. membrane Sci.* 2011, 385, 28.

136.   J. A. Eastman, L.J. Thompson, B.J. Kestel, *Phys. Rev. B* 1993, 48, 84.

137.   Y. M. Wang, M. Chen, F. Zhou, E. Ma, *Nature* 2002, 419, 912.

138.   M. A. Haque, M. T. A. Saif, *Proc. Natl. Acad. Sci. USA* 2004, 101, 6335.

139.   T. Pardoen, M. Coulombier, A. Boe, A. Safi, C. Brugger, S. Ryelandts, P. Carbonnelle, S. Gravier, J. P. Raskin, *Mater. Sci. Forum*, 2010, 633, 615.

140.   O. Anderoglu, A. Misra, H. Wang, X. Zhang, *J. Appl. Phys.* 2008, 103, 094322.

141.   B. Wang, H. Idrissi, M. Galceran, M. S. Colla, S. Turner, S. Hui, J. P. Raskin, T. Pardoen, S. Godet, D. Schryvers, *Int. J. Plast.*, 2012, 37, 140.

142.   A. Kobler, J. Lohmiller, J. Schäfer, M. Kerber, A. Castrup, A. Kashiwar, P. A. Gruber, K. Albe, H. Hahn, C. Kübel, *Beilstein J. Nanotechnol.* 2013, 4, 554.

143.   J. Cai, F. Wang, C. Lu and Y. Y. Wang, *Phys. Rev. B* 2004, 69, 224104.

144.   Y. T. Zhu, X. L. Wu, X. Z. Liao, *Appl. Phys. Lett.* 2009, 95, 031909.

145.   H. Van Swygenhoven, P.M. Derlet, A. Hasnaoui, *Phys. Rev. B* 2002, 66, 024101.

146.   M. Y. Gutkin, I. A. Ovidko, *Mech. Sol.* 2007, 42, 271.

147.   A. Castrup, C. Kubel, T. Scherer, H. Haln, *J. Vac. Sci. Technol.* 2011, 29, 021013.

148.   M. Sennour, S. Lartigue-Korinek, Y. Champion, M. J. Hytch, *Phil. Mag.* 2007, 87, 1465.

149.   G. G. Stoney, *P. Roy. Soc.* 1909, 82, 172.

150.   N. Li, J. Wang, X. Zhang, A. Misra, *JOM-J. Min. Met. Mat.* S. 2011, 63, 62.

151.   M. Meyers, A. Mishra, D. Benson, *Prog. Mater. Sci.* 2006, 51, 427.

152.   K. Jonnalagadda, N. Karanjgaokar, I. Chasiotis, J. Chee, D. Peroulis, *Acta Mater.* 2010, 58, 4674.

153.   G. Guisbiers, M. S. Colla, M. Coulombier, J. P. Raskin, T. Pardoen, *J. Appl. Phys.* 2013, 113, 024513.

154.   W. Nix, *Metall. Trans. A* 1989, 20, 2217

155.   J. Rajagopalan, C. Rentenberger, H. P. Karnthaler, G. Dehm, M. T. Saif, *Acta Mater.* 2010, 58, 4772.

156.   L. Lu, R. Schwaiger, Z. W. Shan, M. Dao, K. Lu, S. Suresh, *Acta Mater.* 2005, 53, 2169.

157.   Y. Wang, A. Hamza, E. Ma, *Acta Mater.* 2006, 54, 2715.

158.   M. Maier, D. Durst, M. Mueller, B. Backes, H. W. Höppel, M. Göken, *J. Mater. Res.* 2011, 26, 1421.

159.   M. Dao, L. Lu, Y. Shen, S. Suresh, *Acta Mater.* 2006, 54, 5421.

160.   M. J. Kobrinsky, C. V. Thompson, *Acta Mater.* 2000, 48, 625.

161.   S. Gravier, M. Coulombier, A. Safi, N. André, A. Boé, J. P. Raskin, T. Pardoen, *J. MicroElectroMech. Syst.* 2009,18, 555.

162.   M. Coulombier, G. Guisbiers, M. S. Colla, R. Vayrette, J. P. Raskin, T. Pardoen, *Rev. Sci. Instrum.* 2013, 84, 036102.

163.   M. S. Colla, B. Amin-Ahmadi, H. Idrissi, L. Malet, S. Godet, J. P. Raskin, D. Schryvers, T. Pardoen, *Nature Comm.* 2015, 6.

164.   X. Wu, Y. T. Zhu, Y. G. Wei, Q. Wei, *Phys. Rev. Lett.* 2009, 103, 205504.

165.   L. Wang, X. Han, P. Liu, Y. Yue, Z. Zhang, E. Ma, *Phys. Rev. Lett.* 2010, 105, 135501.

166.   J. H. Lee, T. B. Holland, A. K. Mukherjee, X. Zhang, H. Wang, *Sci. Rep.* 2013, 3, 1061.

167.   I. L. Dillamoreand, S. M. Smallman, *Philos. Mag.* 1965, 12, 191.

168.   J. Lian, B. Baudelet, A. Nazarov, *Mater. Sci. Eng. A* 1993, 172, 23.

169.   Q. Xu, D. Van Dyck, H. W. Zandbergen, *Ultramicroscopy* 2010, 110, 535.

170.   H. Tanimoto, S. Sakai, H. Mizubayashi, *NanoStruct. Mater.* 1999, 12, 751.

171.   E. Ma, *Science* 2004, 305, 623.

172.   Z. Shan, E. A. Stach, J. M. K. Wiezorek, J. A. Knapp, D. M. Follstaedt, S. X. Mao, *Science* 2004, 305, 654.

173.   E. Ma, Y. M. Wang, Q. H. Lu, M. L. Sui, L. Lu, K. Lu, *Appl. Phys. Lett.* 2004, 85, 4932.

174.   J. Wang, H. Huang, *Appl. Phys. Lett.* 2006, 88, 203112.

175.   T. Zhu, J. Li, A. Samanta, H. G. Kim, S. Suresh, *Proc. Natl. Acad. Sci. U.S.A.* 2007, 104, 3031.

176.   K. A. Afanasyev, F. Sansoz, *Nano Lett.* 2007, **7**, 2056.

177.   J. Wang, N. Li, O. Anderoglu, X. Zhang, A. Misra, J.Y. Huang, J.P. Hirth, *Acta Mater.* 2010, 58, 2262.

178.   U. wolf, F. Ernst, T. Muschik, W. Finnis, H. F. Fischmeister, *Phil. Mag. A* 1992, 66, 991.

179.   T. Muschik, W. Laub, U. Wolf, M. W. Finnin, W. Gust, *Acta metal. mater.* 1993, 41, 2163.

180.   D. Hofmann, F. Ernst, *Ultamicroscopy* 1994, 53, 205.

181.   J. D. Rittner, D. N. Seidman, K. L. Merkle, *Phys. Rev. B* 1996, 53, 4241.

182.   J. Wang, A. Misra, J. P. Hirth, *Phys. Rev. B* 2011, 83, 64106.

183.   J. Wang, O. Anderoglu, J. P. Hirth, A. Misra, X. Zhang, *Appl. Phys. Lett.* 2009, 95, 021908.

184.   U. wolf, P. Gumbsch, H. Ichinose, H. F. Fischmeister, *J. Phys., Paris* 1990, 51.

185.   G. Lucadamo, D. L. Medlin, *Science* 2003, 300, 1272.

186.   L. Liu, J. Wang, S. K. Gong, S. X. Mao, *Phys. Rev. Lett.* 2011, 106, 175504.

187.   F. Ernst, M. W. Finnis, D. Hofmann, T. Muschik, U. Schonberger, U. Wolf, M. Methfessel, *Phys. Rev. Lett.* 1992, 69, 620.

188.   D. Hofmann, M.W. Finnis, *Acta metall. mater.* 1994, 42, 3444.

189.   J. Proost, F. Spaepen, *J. Appl. Phys.* 2002, 91, 204.

190.   S. Ni, Y. B. Wang, X. Z. Liao, R. B. Figueiredo, H. Q. Li, S. P. Ringer, T. G. Langdon, Y. T. Zhu, *Acta Mater.* 2012, 60, 3181.

191.   E. Abe, S. Kajwara, T. Kumagai, M. Nakamu, *Phil. Mag. A* 1997, 75, 975.

192.   C. L. Chen, W. Lu, Y. Y. Cui, L. L. He, H. Q. Ye, *J. Alloys Compd.* 2009, 468, 179.

193.   D. L. Meldin, S. M. Foiles, G. H. Campbell, C. B. Carter, *Mater. Sci. Forum* 1999, 294, 35.

194.   D. L. Medlin, G. H. Campbell, C. B. Carter, *Acta mater.* 1998, 46, 5135.

195.   F. Apostol, Y. Mishin, *Phys. Rev. B* 2011, 84, 104103.

196.   J. Weissmüller, C. Lemier *Phys. Rev. Lett.* 1999, 82, 213.

197.   S. M. Myers, M. I. Baskes, H. K. Birnbaum, J. W. Corbett, G. G. DeLeo, S. K. Estreicher, E. E. Haller, P. Jena, N. M. Johnson, R. Kirchheim, S. J. Pearton, M. J. Stavola *Rev. Mod. Phys.* 1992, 64, 559.

198.   K. H. So, J. S. Kim, Y. S. Chun, K. T. Park, Y. K. Lee, C. S. Lee *ISIJ Int.* 2009, 49, 1952.

199.   R. Daniel, D. Holec, M. Bartosik, J. Keckes, C. Mitterer *Acta Mater.* 2011, 59, 6631.

200.   D. Kumar, A. J. Gupta *Magn. Magn. Mater.* 2007, 308, 318.

201.   H. Köstenbauer, G. A. Fontalvo, M. Kapp, J. Keckes, C. Mitterer *Surf. Coat. Technol.* 2007, 201, 4777.

202.   L. Karlsson, A. Hörling, M. Johansson, L. Hultman, G. Ramanath *Acta Mater.* 2002, 50, 5103.

203.   R. Daniel, K. Martinschitz, J. Keckes, C. Mitterer *Acta Mater.* 2010, 58, 2621.

204.   H. Xu, H. Heinrich, J. M. Wiezorek, *Intermetallics* 2003, 11, 963.

205.   D. C. Miller, C. F. Herrmann, H. J. Maier, S. M. George, C. R. Stoldt, K. Gall, *Scr. Mater.* 2005, 52, 873.

206.   J. Tien, A. Thompson, I. Bernstein, R. Richards *Metall. Mater. Trans. A* 1976, 7, 821.

207.   H. C. Jamieson, G. C. Weatherly, F. D. Manchester, *J. Less-Common Met.*1976, 50,85.

208.   M. V. Goltsova , Yu. A. Artemenko, V. I. Zaitsev, *J. Alloys Compd.* 1999, 293, 379.

209.   H. Hahn, P. Mondal, K. A. Padmanabhan, *Nanostruct. Mater.* 1997, 9,603.

210.   H. Van Swygenhoven, P. Derlet, *Phys. Rev. B* 2001, 64, 224105.

211.   A. J. Haslam, D. Moldovan, V. Yamakov, D. Wolf, S. R. Phillpot, H. Gleiter, *Acta Mater.* 2003, 51, 2097.

212.   Y. Tang, J. A. El-Awady, *Phys. Rev. B* 2012, 86, 174102.

213.   J. von Pezold, L. Lymperakis, J. Neugebeauer, *Acta Mater.* 2011, 59, 2969.

214.   H. Van Swygenhoven, P.M. Derlet, A.G. Froseth, *Acta Mater.* 2006, 54, 1975.

215.   X. L. Wu, Y. Qi, Y. T. Zhu, *Appl. Phys. Lett.* 2007, 90, 221911.

216.   X. Y. Zhang, X. L. Wu, A. W. Zhu, *Appl. Phys. Lett.* 2009, 94, 121907.

217.   Z. Pei, L. F. Zhu, M. Friak, S. Sandlobes, J. von Pezold, H. W. Sheng, C. P. Race, S. Zaefferer, B. Svendsen, D. Raabe, J. Neugebauer, *New J. Phys.* 2013, 15, 043020.

218.   A. Stukowski, *Ph.D. Thesis*, Darmstadt University of Technology, July 2010.

List of abbreviations

Ag	Silver
Al	**Al**uminum
ACOM-TEM	**A**utomated **C**rystal **O**rientation **M**apping in **TEM**
BF	**B**right **F**ield
CCD	**C**oupled **C**harge **D**evice
CTB	**C**oherent **T**win **B**oundary
CSL	**C**oincidence **S**ite **L**attice
Cu	**C**opper
DC	**D**irect **C**urrent
DF	**D**ark **F**ield
DP	**D**iffraction **P**attern
DRIE	**D**eep **R**eactive **I**on **E**tching
e-beam	electron-**beam**
EBSD	**E**lectron **B**ackscattered **D**iffraction
ED	**E**lectron **D**iffraction
EDS	**E**nergy **D**ispersive **X**-Ray **S**pectroscopy
EELS	**E**lectron **E**nergy **L**oss **S**pectroscopy
ESF	**E**xtrinsic **S**tacking **F**ault
fcc	**f**ace **c**entered **c**ubic
FFT	**F**ast **F**ourier **T**ransform
FIB	**F**ocused **I**on **B**eam
GB	**G**rain **B**oundary
GPA	**G**eometric **P**hase **A**nalysis
GIS	**G**as-**I**njection **S**ystems
GPFE	**G**eneralized **P**lanar **F**ault **E**nergies
HAGB	**H**igh **A**ngle **G**rain Boundary
H-P	**H**all-**P**etch
HRTEM	**H**igh **R**esolution **T**ransmission **E**lectron **M**icroscopy
IFFT	**I**nverse **F**ast **F**ourier **T**ransform
ISF	**I**ntrinsic **S**tacking **F**ault

ITB		**I**ncoherent **T**win **B**oundary
LAGB		**L**ow **A**ngle **G**rain **B**oundary
L-C		**L**omer-**C**ottrell
mc		**m**icro**c**rystalline
MD		**M**olecular **D**ynamics
MEMS		**M**icro**E**lectro**M**echanical **S**ystems
Mg		**M**agnesium
nc		**n**ano**c**rystalline
Ni		**N**ickel
OIM		**O**rientation **I**maging **M**icroscopy
Pd		**P**alladium
PVD		**P**hysical **V**apour **D**eposition
RF		**R**adio **F**requency
ROI		**R**egion **O**f **I**nterest
SAD		**S**elected-**A**rea **D**iffraction
SAED		**S**elected-**A**rea **E**lectron **D**iffraction
SEM		**S**canning **E**lectron **M**icroscopy
SF		**S**tacking **F**ault
SFE		**S**tacking **F**ault **E**nergy
SPD		**S**hockley **P**artial **D**islocation
SPD		**S**evere **P**lastic **D**eformation
TB		**T**win **B**oundary
TD		**T**winning **D**islocation
TEM		**T**ransmission **E**lectron **M**icroscopy
UCL		Université Catholique de Louvain
ufg		**u**ltra**f**ine **g**rain
ULB		**F**ree University of **B**russels
XRD		**X**-**R**ay **D**iffraction

List of scientific contributions

Journal articles related to the PhD work

- M.S. Colla, **B. Amin-Ahmadi**, H. Idrissi, L. Malet, S. Godet, J.P. Raskin, D. Schryvers, T. Pardoen, *"Dislocation mediated relaxation in nanograined columnar Palladium films revealed by on-chip time-resolved HRTEM testing"*, **Nature Communications** 6, 1-8, 2015.

- H. Idrissi, **B. Amin-Ahmadi**, B. Wang, D. Schryvers, *"Review on TEM analysis of growth twins in nanocrystalline palladium thin films: Toward better understanding of twin-related mechanisms in high stacking fault energy metals"*, **Phys. Status Solidi B**, 251, 1111, 2014.

- **B. Amin-Ahmadi**, H. Idrissi, R. Delmelle, T. Pardoen, J. Proost, D. Schryvers, *"High resolution transmission electron microscopy characterization of fcc - 9R transformation in nanocrystalline palladium films due to hydriding"* **Applied Physics Letters,** 102:071911, 2013.

- **B. Amin-Ahmadi**, H. Idrissi, M. Galceran, M.S. Colla, J.P. Raskin, T. Pardoen, S. Godet, D. Schryvers, *"Effect of deposition rate on the microstructure of electron beam evaporated nanocrystalline palladium thin films"*, **Thin Solid Films**, 539, 145, 2013.

- R. Delmelle, **B. Amin-Ahmadi**, H. Idrissi, D. Schryvers, J. Proost, *"Effect of microstructure on the hydriding kinetics of nanocrystalline Pd thin films"*, accepted for publication in **International Journal of Hydrogen Energy**.

- **B. Amin-Ahmadi**, D. Connétable, M. Fivel, D. Tanguy, R. Delmelle, S. Turner, T. Pardoen, J. Proost, D. Schryvers, H. Idrissi, *"Dislocation/hydrogen interaction mechanisms in hydrided nanocrystalline palladium films"*, to be submitted to **Acta Materialia**.

Journal articles NOT related to the PhD work

- M. Kabiri Samani, X. Z. Ding, N. Khosravian, **B. Amin-Ahmadi**, Y. Yi, G. Chen, E. Neyts, A. Bogaerts, B. K. Tay, *"Thermal conductivity of titanium nitride/titanium aluminum nitride multilayer coatings deposited by lateral rotating cathode arc"*, **Thin Solid Films** 578, 133, 2015.

- H. Idrissi, A. Kobler, **B. Amin-Ahmadi**, M. Coulombier, M. Galceran, J-P Raskin, S. Godet, C. Kübel, T.Pardoen, D. Schryvers, *"Plasticity mechanisms in ultrafine grained freestanding aluminum thin films revealed by in-situ transmission electron microscopy nanomechanical testing"*, **Applied Physics Letters,** 104, 101903, 2014.

- J. Peirs, W. Tirry, **B. Amin-Ahmadi**, F. Coghe, P. Verleysen, L. Rabet, D. Schryvers, J. Degrieck, *"Microstructure of adiabatic shear bands in Ti6Al4V"*, **Materials Characterization,** 75,79, 2013.

- X. Wang, **B. Amin-Ahmadi**, D. Schryvers, B. Verlinden, J. Van Humbeeck, *"Effect of Annealing on the Transformation Behavior and Mechanical Properties of Two Nanostructured Ti-50.8at.%Ni Thin Wires Produced by Different Methods"*, **Materials Science Forum** 738, 306, 2013.

Conference contributions

- Oral presentation titled "*First experimental study of nanoscale plasticity mechanisms in nanocrystalline Pd thin films under hydrogen cycling"*, 18th International Microscopy Congress (IMC), Czech republic, Prague 2014.

- Oral presentation titled " *Dislocation mediated hardening and relaxation in nanocrystalline palladium films revealed by on-chip HRTEM in-situ nano mechanical testing*", 16th international conference on experimental mechanics (ICEM16), 2014, UK.

- Poster presentation titled "*Study of Pd thin films deformed by on chip nanomechanical tensile testing using ACOM-TEM*", International workshop on Precession Electron Diffraction, Diffraction Tomography and Orientation Imaging, Germany 2012.

- Poster presentation titled "*Active plasticity mechanisms during hydriding of nanocrystalline Pd thin films*", Small scale plasticity workshop, Corsica, France 2013.

- Poster presentation titled *"Effect of deposition rate on the formation of growth twins in Pd thin films"* 15th European Microscopy Congress (emc 2012), Manchester, UK, 2012.

- Poster presentation titled "*First high resolution transmission electron microscopy characterization of fcc→9R transformation in nanocrystalline palladium films due to hydriding* " Microscopy Congress, Regensburg, Germany, 2013.

- Poster presentation titled *"Dislocation mediated creep/relaxation in nanocrystalline palladium thin films revealed by on-chip high resolution TEM time-resolved testing*", 18th International Microscopy Congress (IMC), Czech republic, Prague 2014.

Acknowledgment

Bringing a Ph. D. thesis up to its end is obviously an important personal challenge. But it cannot be properly carried out without the scientific, technical and human contribution of numerous people, who I wish to warmly acknowledge here.

Foremost, I would like to express my sincere gratitude to my advisor Prof. Dominique Schryvers for giving me the opportunity to start my PhD studies at world-class EMAT research group. I also thank him for the continuous support of my PhD study and research, for his patience, motivation, enthusiasm, and immense knowledge. His guidance helped me in all the time of research and writing of this thesis. I could not have imagined having a better advisor for my PhD study.

At the same time, I can never thank enough to my co-promoter, Dr. Hosni Idrissi for his altruistic enthusiasm and sensible advice. Without his passionate participation and scientific discussion, the validation survey could not have been successfully conducted.

Besides my advisors, I would like to thank the rest of my jury members: Prof. E. Goovaerts, Prof. C. Kübel, Prof. T. Pardoen, Prof. B. Partoens, for their encouragement, insightful comments, and useful questions.

I would also like to cordially thank Prof. Thomas Pardoen and Dr. Marie-Stephane Colla from UCL for providing the e-beam deposited and free standing Pd films, Prof. Joris Proost and Dr. Renaud Delmelle from UCL for deposition and hydriding the sputtered Pd films and finally Prof. Stephane Godet, Dr. Montserrat Galceran and Loic Malet from ULB for performing ACOM-TEM experiments on nc Pd films.

I want to express my great gratitude to my colleagues in EMAT and friends for their help and support during the process of researching and writing this thesis.

Finally, and most importantly, I must express my very profound gratitude to my parents and to my wife, Sanaz for providing me with unfailing support and continuous encouragement throughout my years of study and through the process of researching and writing this thesis. This accomplishment would not have been possible without them. Thank you.